Isolated Direct Double Photon Production in $\overline{p}p$ collisions at $\sqrt{s}$ = 1.8 TeV with the DØ Detector

A Dissertation Presented

by

Wei Chen

to

The Graduate School

in Partial Fulfillment of the Requirements

for the Degree of

Doctor of Philosophy

in

Physics

State University of New York
at
Stony Brook

December 1997

State University of New York at Stony Brook

The Graduate School

Wei Chen

We, the dissertation committee for the above candidate for the Doctor of Philosophy degree, hereby recommend acceptance of the dissertation.

---

dissertation director
Professor Roderich J. Engelmann
Department of Physics

---

chairman of defense
Professor Paul Grannis
Department of Physics

---

committee member
Professor George Sterman
Department of Physics

---

outside HEP group
Professor Daev Fossan
Department of Physics

---

outside member
Doctor John Womersley
Fermi National Accelerator Laboratory

This dissertation is accepted by the Graduate School.

Graduate
School

Abstract of the Dissertation

Isolated Direct Double Photon Production in $\overline{p}p$ collisions at $\sqrt{s}$ = 1.8 TeV with the DØ Detector

by

Wei Chen

1997

This thesis reports a measurement of direct double-photon production, $p\overline{p} \rightarrow \gamma\gamma + X$, in $p\overline{p}$ collisions at $\sqrt{s}$ =1.8 TeV with the DØ detector. The data sample corresponds to an integrated luminosity $\int \mathcal{L}dt = 82.36 \pm 4.40 pb^{-1}$. We observe 333 double-photon candidate events in the region $|\eta^1| < 1.0, |\eta^2| < 1.0, E_T^1 > 14.0GeV, E_T^2 > 13.0GeV$. This implies a production cross section $\sigma = 8.7 \pm 1.5(stat)^{+2.9}_{-3.4}(syst)pb$, The four differential cross sections, $d\sigma/dE_T^\gamma$, $d\sigma/dM^{\gamma\gamma}$, $d\sigma/dP_T^{\gamma\gamma}$ and $d\sigma/d\Delta\phi^{\gamma\gamma}$, are compared to the NLO QCD, the Resummed QCD(RESBOS) and the PYTHIA calculations. At the high Q^2 region (corresponding to large $P_T^{\gamma\gamma}$), data agree well with the NLO calculation. At the low Q^2 region (corresponding to small $P_T^{\gamma\gamma}$), the data show reasonable agreement with the Resummed QCD calculation.

To Justin, Nathan and My Mother

Contents

List of Figures

List of Tables

Acknowledgements

First I'd like to thank my thesis advisor, Rod Engelmann, for all the help and tolerance he has provided. Appreciations go to the rest of Stony Brook group, Paul Grannis, Bob McCarthy and Michael Rijssenbeek, and the old student crowd, Jim Cochran, Joey Thompson, Marc Paterno, Scott Snyder, Dhiman Chakraborty and Paul Rubinov. I'd like to thank two Stony Brook postdocs, Dan Claes and Rich Astur. Dan Claes patiently explained to me the level-2 trigger and error analysis, and Rich Astur taught me how to program.

I would like to thank Hailin Li and Ting Hu for helpful discussion, and the three newest Stony Brook members: Slava Kulik, Bogdan Kulik and Dennis Shpakov. Special thanks go to Slava for reading and correcting my writing.

Specially I'd like to thank Dr.Yuri Fisyak. He taught me statistics. His knowledge and deep understanding opened up a new world to me.

I would like to thank the two QCD convenors, Prof.Heidi Schellman and Dr.Nikos Varelas. Heidi's scientific honesty and judgement helped tremendously in shaping up this analysis. A lot of thanks to Heidi.

I would also like to thank the direct photon group, John Womersley, Steve Linn, Steve Jerger, Pierrick Hanlet, and the old members: Sal Fahey,

Bob Madden and Paul Rubinov. Thanks John Womersley for carefully reading my writing and pointing out a lot of mistakes.

As a d0fs shifter, I worked closely with Lee Lueking and Dorota Genser. A lot of Thanks go to Dorota. I learned a lot by hacking her codes and asking her questions.

Last, not the least, I'd like to thank my husband, Justin. Without him, I would not be who I am now. For numerous occasions, he assumed the babysitting job and let me go in during evenings and weekends. His love and support kept me through these years. Our sweet boy, Nathan, is my constant joy and hope. His innocence and sense of justice remind me what the true world is and keep me sane when working in a big collaboration. I am also grateful to my Mom. She brought me up single-handed and supported me even during some very difficult times.

Chapter 1

QCD and Direct Photon Physics

1.1 The Standard Model

The *standard model* of elementary particles and their fundamental interactions (see Table 1.1) has been repeatedly demonstrated to be a good description of nature at the subnuclear energy scale. The fundamental constituents are six quarks and six leptons. They are all fermions, and can be grouped into three generations. It remains a great puzzle why nature chooses to repeat itself in three generations or more. Recently the precise measurement of the width of the Z boson at LEP[1] and SLD[2] shows that there are only three species of neutrinos with masses $< m_Z/2$ [1, pp.286]).

These constituents interact through four fundamental forces: strong, unified electroweak and gravitational. The first three interactions are transmitted by exchange of gauge bosons, which are described by Yang-Mills gauge field

[1] LEP for Large Electron Positron Collider

[2] SLD for Stanford Linear Collider

FERMIONS (matter constituents)						
	Leptons (spin=1/2)			**Quarks** (spin=1/2)		
	Flavor	Mass (GeV/c^2)	Electric Charge	Flavor	Appr.Mass (Gev/c^2)	Electric Charge
1st gener.	ν_e	$<7\times10^{-9}$	0	u	0.005	2/3
	e	0.000511	-1	d	0.01	$-1/3$
2nd gener.	ν_μ	< 0.0003	0	c	1.5	2/3
	μ	0.106	-1	s	0.2	$-1/3$
3rd gener.	ν_τ [a]	< 0.03	0	t	175	2/3
	τ	1.7771	-1	b	4.7	$-1/3$
FOUR INTERACTIONS Gauge Bosons as Force Carriers						
Interaction	Gauge Bosons	Mass (GeV/c^2)	Electric Charge	Spin-parity	Coupling Constant	
Strong	g(gluon)	0	0	1^-	$\alpha_s \sim 1$	
Unified Electroweak	γ(photon)	0	0	1^-	α_{EM}=1/137	
	W^+	80.33	+1	1^-	1.02×10^{-5}	
	W^-	80.33	-1	1^-	1.02×10^{-5}	
	Z^0	91.187	0	1^+	1.02×10^{-5}	
Gravity	graviton [b]	0	0	2^+	0.53×10^{-38}	
HIGGS BOSON breaking EW symmetry						
	H [b](higgs)	>67	0	0	?	

Table 1.1: The Fundamental Particles and Interactions in the Standard Model [1, pp.19-23]

[a] not directly observed

[b] not observed

theories. The unified electroweak interaction is, described by a spontaneously-symmetry-broken SU(2)×U(1) gauge theory [2], and the strong interaction by an unbroken SU(3) color gauge theory, known as quantum chromodynamics (QCD). [2, 3]

The *standard model* has been extremely successful. The electroweak interaction has a weak coupling (less than 1), and can be calculated by making a perturbative expansion in the order of the coupling. Nearly all the electroweak theory predictions have been beautifully confirmed by experiments. Unlike the electroweak interaction, the strong interaction has a strong coupling, $\alpha_s \approx 1$, and therefore can a priori not be calculated by perturbative expansion. In this context, Regge theory and S matrix approach and various other non-perturbative developments flourished. Only in the early seventies, many developments in gauge field theory and the renormalization group led to the concept of "running" effective coupling and asymptotic freedom [4, 5]. Asymptotic freedom is a perturbative concept and makes it feasible to calculate a substantial number of large momentum Q^2 transfer (e.g. short distance) processes by perturbative QCD (pQCD in brief) (for a detailed review about pQCD, see [3]). Even with little knowledge about the contributions from higher orders, the perturbative QCD calculations have agreed reasonably well with experimental tests of the strong interaction, though a lot of work, both theoretical and experimental, remains to be done.

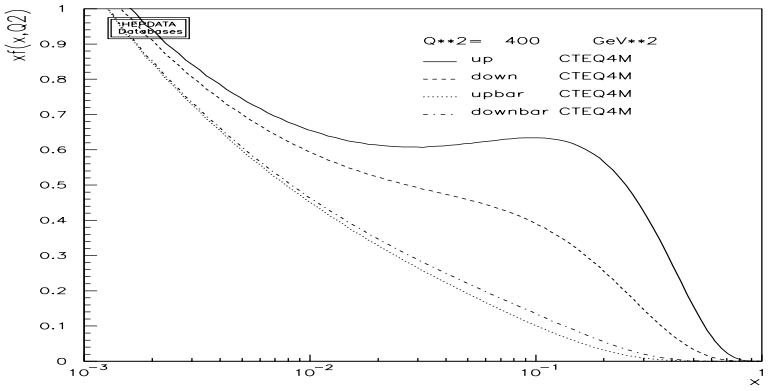

Figure 1.1: The quark momentum probability density functions (PDF)

1.2 The Parton Model and Quantum Chromodynamics

1.2.1 Hadron Colliders

Experimentally, there are two ways to produce high energy processes. We can accelerate one beam to high energy and then let it hit a stationary target, or accelerate two beams to high energy and let them collide with each other

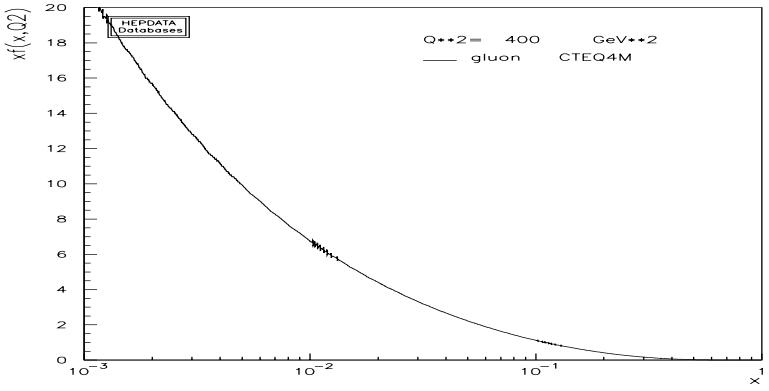

Figure 1.2: The gluon momentum probability density function (PDF)

head-on. The available center-of-mass energy is $\sqrt{s} = \sqrt{4E_A E_B}$ for colliding beam experiments and $\sqrt{s} = \sqrt{2E_A m_B}$ for fixed target experiments, where E_A, E_B are the beam energy and m_B the mass of the target. $\sqrt{s}$ grows linearly with the beam energy in collider experiments, and increases only as the square root of the beam energy in fixed target experiments.

Colliders are therefore more efficient to reach the higher energy frontier, and provide possibilities of finding new phenomena and particles. The $p\overline{p}$ collider at *CERN* reached the highest center-of-mass energy $\sqrt{s} = 630$ GeV at the time when the W and Z bosons were discovered [6]. During 1992 to 1995, the $p\overline{p}$ collider at Fermilab had a successful run at the highest energy $\sqrt{s} = 1800$ GeV and discovered the Top quark [7, 8]. In addition, the Fermilab collider has produced hundreds of thousands of high Q^2 events(here $Q^2 = -t^2$), which can help us to understand perturbative QCD.

1.2.2 The Parton Model

Around 1968, deep-inelastic electron-nucleon scattering experiments at SLAC [9, 10] showed that the structure functions of the nucleon exhibited approximate "scaling". The scaling phenomenon can be interpreted if the scattering nucleon contains pointlike particles [11, 12]. This assumption is known as the *Bjorken scaling hypothesis.* In physical terms, Feynman proposed the parton model [14] which viewed the nucleons as consisting of structureless constituents that are nearly free from each other and each carries a fraction of nucleon energy as xP^μ. Later, the pointlike constituents were identified as

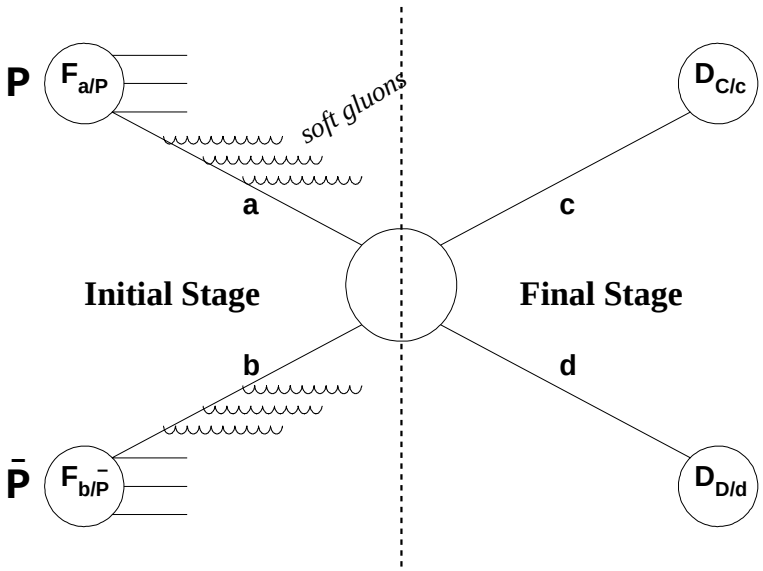

Figure 1.3: A schematic picture of $p\overline{p}$ collision. The initial partons a and b are carrying longitudinal momentum $P_z = xP$ according to parton density functions $F_{a/P}(x_a, Q_a^2)$ and $F_{b/\overline{P}}(x_b, Q_b^2)$. They radiate soft gluons before the collision. The hard scattering between the incoming partons a and b takes a shorter time than the final stage of fragmentation. The hard collision therefore can be treated separately from the final stage processes and be described by a simple $2 \rightarrow 2$ cross section $d\sigma(ab \rightarrow cd)$. The partons c and d, emerging after collision, recombine with the rest of partons and fragment into hadrons according to fragmentation functions $D_{C/c}(z_c)$ and $D_{D/d}(z_d)$, where z is the fraction of hadron momentum. The observed cross section is the parton cross section convoluted with the initial state PDF's and the final state fragmentation function.

quarks and gluons, which cannot exist in isolation. They can only appear in a colorless bound state, known as the "confinement" hypothesis.

Using this parton model, let us imagine what happens when a proton collides with an antiproton. Both proton and antiproton are made of partons (see fig. 1.3). The basic assumption is that the collision occurs in two independent stages. First two partons, one from each hadron, are scattered, the hard collision time being $t_1 \approx \hbar/\mu$, where μ is the energy transfer during the

scattering. Over a much longer time, the partons, having emerged from hard scattering, recombine to form the final hadronic states, through very complicated processes of fragmentation and hadronization. The recombination takes place over a long time scale and can be treated separately from the initial collision. The cross section therefore depends first and foremost on the dynamics of the initial stage, and only weakly on the complexity of the final state. This turns out to be a good assumption.

The probability that a parton carries a fraction x of its parent hadron's momentum is given by the probability density function $F(x, Q^2)$, called a *PDF*. The *PDF* function is parametrized and fitted to a large set of experimental data. Take the proton as an example. Its partons are identified as three valence quarks, uud, and a sea of virtual quark-antiquark pairs and gluons. Figures 1.1 and 1.2 show one set of *PDF*s, *CTEQ4M* [13]. For final state hadrons, the fragmentation function $D_{C/c}(z_c)$ is defined as the probability for parton c to produce a hadron C carrying a fraction z_c of parton c momentum. The overall cross section, for the process shown in fig. 1.3, is the hard-scattering matrix element convoluted with the PDF's and the fragmentation functions:

$$E_C \frac{d\sigma}{d^3 p_C}(p\overline{p} \to C + X) = \sum_{abcd} \int dx_a dx_b dz_c F_{a/P}(x_a, Q^2) F_{b/\overline{P}}(x_b, Q^2) \times \frac{\hat{s}}{z_c^2 \pi} \frac{d\sigma}{d\hat{t}}(ab \to cd) \times D_{C/c}(z_c) \delta(\hat{s} + \hat{t} + \hat{u}). \quad (1.1)$$

where E_C and p_C are the energy and momentum of the final state hadron C. $\hat{s}$, $\hat{t}$ and $\hat{u}$ are the partonic s, t and u, defined as:

$$\hat{s} = (x_a p_p + x_b p_{\overline{p}})^2, \qquad \hat{t} = (x_a p_p - \tfrac{1}{z_c} p_C)^2, \qquad \hat{u} = (x_a p_p - p_d)^2$$

Here Q^2 is the momentum transfer involved in the hard scattering.

1.2.3 Perturbative QCD and Sudakov Resummation

Historically, QCD emerged in the 1960s when the quark model was proposed by Gell-Mann [15] and Zweig [16]. Out of the quark model grew the idea of color as a new quantum number. Three different kinds of colors were needed to explain hadron spectroscopy. The color idea was then extended to a SU(3) quantum gauge field theory, quantum chromodynamics, where the color quantum number was treated analogous to isospin [17, 18]. In QCD, the color charge, like the electric charge, interacts with other color carriers by exchange of gauge bosons: gluons. There are eight types of gluons in total.

Experimentally electron-positron annihilation at high energy, say above 10 GeV CMS energy, provides the most convincing evidence for the quark-parton model and the three-color hypothesis (for a good review, see [19]). Let us measure the processes $e^+e^- \rightarrow \ hadrons$ and $e^+e^- \rightarrow \ \mu^+\mu^-$. When we take the ratio of two cross sections, defined as

$$Ratio = \frac{\sigma(e^+e^- \rightarrow \ hadrons)}{\sigma(e^+e^- \rightarrow \ \mu^+\mu^-)} \tag{1.2}$$

the ratio behaves roughly as a step function in the center-of-mass energy. Theoretically the leading order contribution is from the electromagnetic interaction, and the ratio can be simply expressed as

$$Ratio = \frac{\sum_{quark\ i}\ e_i^2}{1} \tag{1.3}$$

where e_i is the electric charge of quark i.

The Ratio grows with the center-of-mass energy, depending upon the number of quark-antiquark pairs which the center-of-mass energy is able to excite. For $\sqrt{s} > 10$ GeV,

$$Ratio(\sqrt{s} > 10GeV) = (\frac{2}{3})^2 + (\frac{1}{3})^2 + (\frac{2}{3})^2 + (\frac{1}{3})^2 + (\frac{1}{3})^2 = \frac{11}{9} \qquad (1.4)$$

where the experimental data at $\sqrt{s} > 10$ GeV are consistent with a constant, having a value equal to $\frac{11}{3}$. The introduction of three colors for each quark, as an additional quantum number, increases the theoretical ratio by a factor of 3 and brings the quark-parton model prediction into line with experiment.

The success of QCD can be summarized by two terms: asymptotic freedom [4, 5] and confinement. Asymptotic freedom refers to the weakness of the short-distance interaction, while the confinement follows the force's ever-increasing strength at long distance. QCD can accomodate these unusual features. The effective strong coupling α_s "runs" as the momentum transfer Q^2 grows.

Because the coupling constant α_s is weak at short distance, any physical quantity can be expanded in orders of α_s with a certain degree of caution. Perturbative QCD calculation can only be applied to a class of experimental quantities to which asymptotic freedom may be applied consistently. Those quantities are *infrared safe* [20], which means they do not depend upon the long-distance behavior of QCD.

Since the discovery of asymptotic freedom, a lot of work has been carried out to calculate various cross sections at fixed order of α_s, like leading order (LO) and next-to-leading order (NLO) calculations. In the process,

it was realized that some calculations can be better done if we can reorganize the perturbative series to identify and calculate infrared safe quantities. One approach to reorganize the series is to use various resummation techniques [21, 22, 23, 24]. It is because of two basic ideas, factorization and evolution of QCD, that perturbative QCD can be used to make predictions. Factorization enables us to factor long-distance from short-distance dependence, and keep the physical quantities infrared safe. Evolution allows the parton distribution functions $F_2(x, Q^2)$ to be moved to the high Q^2 scale (where pQCD can be applied) from the low Q^2 region, and therefore perturbative calculation is feasible. The evolution is described by the Altarelli-Parisi evolution equations [25].

Sudakov Resummation

Here I will briefly describe one resummation scheme, Sudakov resummation [22]. For direct double-photon production, we define q_T as $q_T = |\vec{E_T^{\gamma 1}} + \vec{E_T^{\gamma 2}}|$. The basic idea is that the perturbative expansion becomes infrared divergent at low q_T. As $q_T \to 0$, the dominant contributions to the cross section can be written in the form:

$$\frac{d\sigma}{dq_T^2} \approx \frac{\alpha_s}{q_T^2} \ln(\frac{Q^2}{q_T^2})[v_1 + v_2 \alpha_s \ln^2(\frac{Q^2}{q_T^2}) + v_3 \alpha_s^2 \ln^4(\frac{Q^2}{q_T^2}) + ...] \qquad (1.5)$$

These correspond to the processes in which multiple soft gluons contribute to the cross section. The resummation of all the large logarithms gives a Sudakov form factor and keeps the cross section infrared safe at $q_T \to 0$. The formalism was developed by Collins, Soper and Sterman [22]. By using their prescription,

the cross section can be written as two parts, the resummation part Y_r and the finite one Y_f. The resummed part Y_r is given as:

$$\begin{aligned} & Y_r(q_T^2, Q^2, y, \theta) \\ & \quad = \Theta(Q^2 - q_T^2) \times \tfrac{1}{2\pi} \int b db J_0(q_T b) \textstyle\sum_{c,d} [F^{NP}(Q, b, x_c, x_d) \\ & \qquad \times W_{cd}(Q, b_*, \theta) f'_{c/A}(x_c, \mu(b_*)) f'_{d/B}(x_d, \mu(b_*))] \end{aligned} \tag{1.6}$$

where c and d are the parton labels, and A and B are the initial state particle labels. $W_{cd}(Q, b_*, \theta) = \exp[S(b, Q)] H_{cd}^{(0)}(\theta)$. The finite part Y_f is small. The Sudakov form factor S(b,Q) is expressed as

$$S(b, Q) = \int_{b_0^2/b^2} Q^2 \frac{d\overline{\mu}^2}{\overline{\mu}^2} \left[\ln \left(\frac{Q^2}{\mu^2} \right) A(\alpha_s(\overline{\mu})) + B(\alpha_s(\overline{\mu})) \right] \tag{1.7}$$

where A and B are known coefficients [27]. A detailed description of the above equations can be found in [29].

All coefficients are known except the non-perturbative function $F_{ab}^{NP}(Q, b, x_A, x_B)$. Ladinsky and Yuan proposed one parametrization for the function [26]

$$F^{NP}(Q, b, x_A, x_B) = \exp(-[g_2 b^2 \ln(\frac{Q}{2Q_0}) + g_1 b^2 + g_1 g_3 b \ln(\frac{\tau}{\tau_0})]) \tag{1.8}$$

where the parameters were determined by fitting to two Drell-Yan experiments E288 and R209. Their values in the above paper [26] are as

$$\tau_0 = 0.01, \quad Q_0 = 1.6 GeV, \quad b_{lim} = 0.5 GeV^{-1}$$

$$g_1 = 0.11^{+0.04}_{-0.03} GeV^2, \quad g_2 = 0.58^{+0.1}_{-0.2} GeV^2, \quad g_3 = -1.5^{+0.1}_{-0.1} GeV^{-1}$$

Using the above formalism, a Monte Carlo program, RESBOS [28, 29], has been developed so that experimentalists can apply cuts and compare the resummed calculation to data.

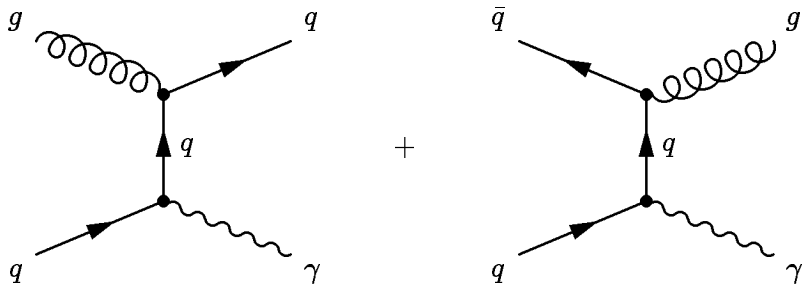

Figure 1.4: Direct Photon Production at $p\overline{p}$ ($p\overline{p} \rightarrow \gamma$X) , to the left the compton and to the right the annihilation subprocess.

1.3 Direct Photon Physics

1.3.1 Theory

Direct photon production refers to the processes where the final state photons are produced directly from hard scattering of incoming partons, not from secondary decays(for review, see [30, 31]). Direct single photon production has two subprocesses, $gq \rightarrow \gamma q$ (compton) and $q\overline{q} \rightarrow \gamma g$ (annihilation), at the lowest order $O(\alpha\alpha_s)$ [see Fig. 1.4]. At $\sqrt{s} = 1800$ GeV, the parton x_T (defined as $x_T = 2p_T/\sqrt{s}$, where p_T is the transverse momentum of the parton) is in the range of $0.01 \sim 0.1$. When the direct photon is constrained to the central region (requiring $|\eta|$ less than 1.1), the corresponding parton x falls between 0.01 and 0.17. Fig. 1.1 and Fig. 1.2 show the gluon content is larger than the quark content of the proton in this region. In Fig. 1.4, the gluon distribution enters at the lowest order, while, in deeply inelastic scattering (DIS) and Drell-Yan production, the gluon distribution contributes to the structure functions only in the next-to-leading order. Direct single photon data is therefore very sensitive to gluons, and can be used to constrain the gluon distribution PDF's

(see [3], pp.222).

Double-Photon Production

In addition to direct single photon production, there is the direct double-photon production. At a $p\overline{p}$ collider, the double-photon final state is clean and well defined regarding the photon's energy and angle, unlike the jet final state which is messy due to fragmentaion and can only be defined given a certain jet reconstruction algorithm. It has long been recognized as an important process for testing the parton model, the short distance dynamics of quarks and gluons, and QCD [32, 33]. In Figure 1.5, the Born process is just a QED(Quantum Electrodynamics) interaction and its cross section is proportional to the fourth power of the charge of the hard-colliding quark. If there was a way to isolate this subprocess, it would be possible to measure the fourth power of the quark charges by comparing the rate with that for single photon produced by the subprocess $q\overline{q} \rightarrow g\gamma$. However, the other subprocess, illustrated as the box diagram in Figure 1.5, is comparable to it or even larger at low x_{T} values. In the $p\overline{p}$ collider at $\sqrt{s}$ = 1800 GeV at Tevatron, the direct double-photon events have one photon p_T ranging from 10 to 50 GeV/c, equivalent to an x_{T} range from 0.011 to 0.055. In figure 1.1 (quark PDF) and figure 1.2 (gluon PDF), the gluon content is nearly ten times the quark content at $x = 0.02$. If this subprocess can be isolated, it can provide a useful constraint on the gluon PDF. Two complete NLO QCD calculations of double-photon production have been presented by Aurenche *et al.* [34] and Bailey *et al.* [35].

Besides the usual variables one photon E_T and double-photon mass, it

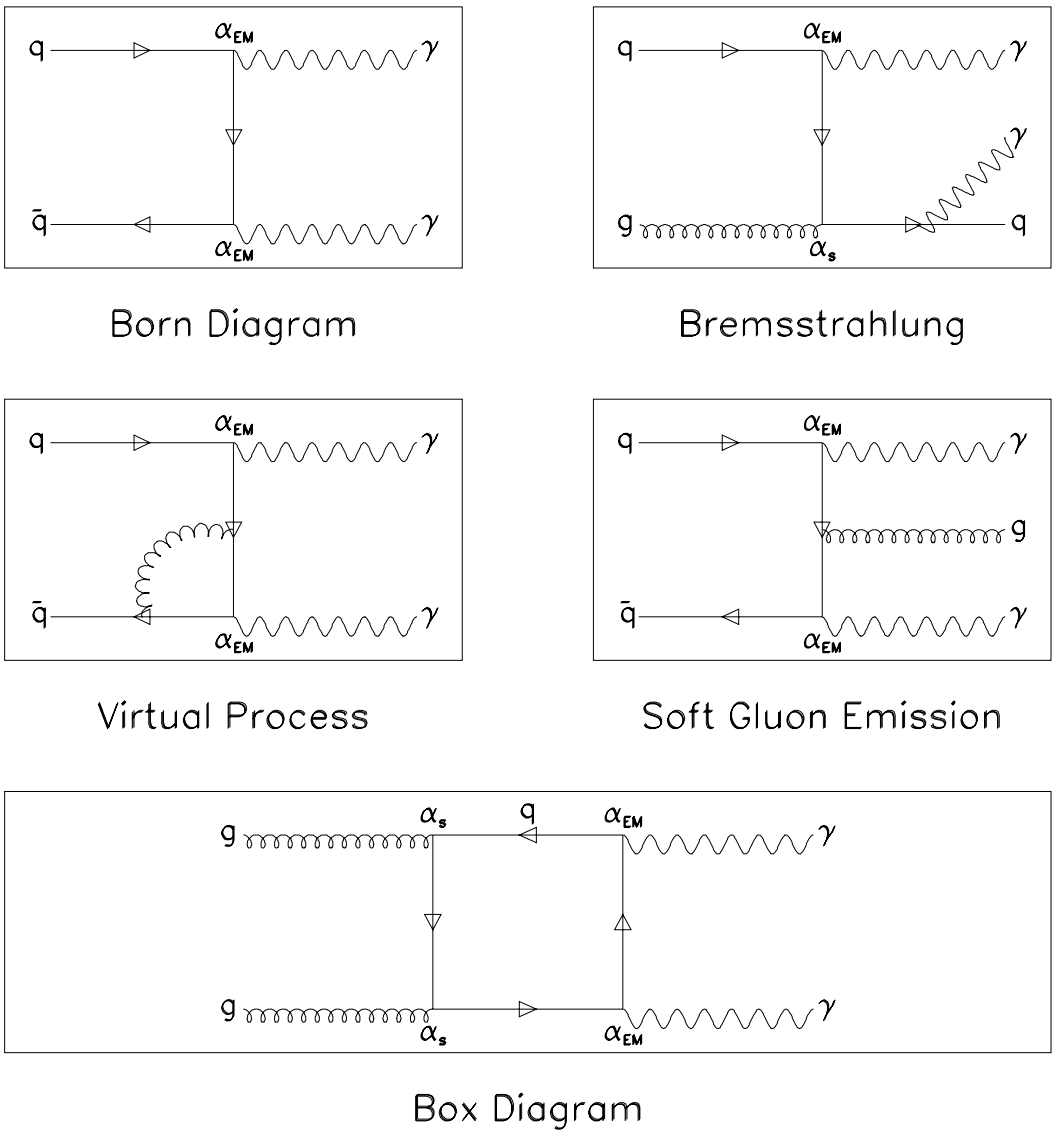

Figure 1.5: The NLO QCD contributions to direct double-photon production at the $p\overline{p}$ collider.

is specially interesting to study the transverse momentum imbalance of the double-photon system, defined as $p_{\rm T} = |\vec{p_{\rm T}^1} + \vec{p_{\rm T}^2}|$. Around $p_{\rm T} = 0$, the cross section is ill-defined in both LO and NLO calculations. Higher order contributions become important. The cross section near $p_{\rm T} = 0$ is sensitive to multiple soft gluon radiation, and is the region in which the soft gluon resummation [36, 28] can be tested and its parameters get constrained. It is also interesting to study $\Delta\phi$, defined as $\Delta\phi = |\phi_1 - \phi_2|$, of the double-photon system, where ϕ is the angle of each photon. When $\Delta\phi$ is far from π (back-to-back), the cross section only arises from the extra jet produced in the NLO calculation and is very sensitive in testing the NLO QCD prediction.

Another extremely important motivation for understanding QCD direct double-photon production has to do with the Standard Model(SM) Higgs boson search at LHC (Large Hadron Collider). In the intermediate mass range $80 \leq M_{\rm H} \leq 150$ GeV, the decay mode $H \rightarrow \gamma\gamma$ will be the most promising channel to discover the SM Higgs boson. For this purpose, an accurate prediction of the QCD direct double-photon background is mandatory. The $p\overline{p}$ collider at the Tevatron is the ideal place to measure this QCD process, and helps to improve the QCD prediction at the LHC.

1.3.2 Experimental Tests of Direct Double-Photon Production

Ever since 1982, several experimental collaborations have observed and published direct double-photon production results in hadron-hadron collisions,

Experi -ment	Beams	$\sqrt{s}$ GeV	integ.L pb^{-1}	p_{T}^{min} GeV/c	x_{T}^{min}	Num $\gamma\gamma$ Events (Stat.Signifi.)
R806	pp collision	63	80	2.0	0.0635	31 ± 16 (1.9 σ)
AFS	pp collision	63	15	1.1	0.0349	23 ± 11 (2.1 σ)
NA3	p, π^+, π^- beams on a carbon target	19.4	?	1.8	0.185	1.48 ± 0.38 (3.9 σ)
WA70	π^- beam on a hydrogen target	22.9	7.7	$p_T^1 > 3.0$, $p_T^2 > 2.75$	0.240	138 ± 23 (6.0 σ)
UA1	$p\overline{p}$ collision	630	0.567	12	0.0381	6 ± 2.7 (2.2 σ)
UA2	$p\overline{p}$ collision	630	13.2	$p_T^1 > 10$ $p_T^2 > 9$	0.0286	58.2 ± 13.4 (4.3 σ)
CDF	$p\overline{p}$ collision	1800	4.3	10	0.0111	$86 \pm 27\ ^{+32}_{-27}$ (2.2 σ)
This(DØ)	$p\overline{p}$ collision	1800	82.36	$p_T^1 > 14.$, $p_T^2 > 13.$	0.0144	$180 \pm 31\ ^{+60}_{-70}$ (2.5 σ)

Table 1.2: Various experiments have measured double direct photon production in hadron-hadron collisions

by using different beams and targets [31, 30]. Table 1.2 lists the relevant parameters for those experiments.

The R806 collaboration, in 1982, reported the first evidence of direct double-photon production at the CERN Intersecting Storage Rings (ISR) [37]. They presented a cross section of $d^2\sigma/dmdy|_{y=0} = 8 \pm 4$ pb/GeV/c^2 for $8 \leq m_{\gamma\gamma} \leq 11$ GeV/c^2(where m is the mass of the photon pair and y is

the rapidity of the pair system), and a ratio $\gamma\gamma/e^+e^- = 1.7 \pm 1$. A little later in 1986 at the CERN ISR, the AFS collaboration measured the same process [38]. They reported a positive $\gamma\gamma$ signal with a cross section of $d^2\sigma/dmdy|_{y=0} = 5.5 \pm 2.7 pb/GeV/c^2$ for $4 \leq m_{\gamma\gamma} \leq 6$ GeV/c^2 and a ratio of $\gamma\gamma/e^+e^- = 4.0 \pm 3.0$. At the CERN Super Proton Synchrotron (SPS) in 1985, the NA3 collaboration measured double-photon production using various beams incident on a fixed target. They reported a cross section 1.48 ± 0.38 pb for $p_T > 1.8$ GeV/c [39]. The signal is more than three standard deviations from zero. Later in 1989 at the CERN SPS, the WA70 collaboration used a π^- beam bombarding a hydrogen target and observed a signal of six standard deviations, with a cross section 54 ± 9 pb for $p_T > 3.0$ GeV/c [40].

After the $p\overline{p}$ collider was turned on at the CERN SPS, the UA1 collaboration collected a small data sample in 1988, corresponding to an integrated luminosity of 567 nb^{-1}. They reported six $\gamma\gamma$ candidates with one background. Their cross section is $38 \pm 19 \pm 10$ pb for $E_T > 12$ GeV [41]. Much later in 1992 at the same collider, the UA2 collaboration presented a double-photon measurement with their upgraded detector and a large data sample with 13.2 pb^{-1} [42]. They observed a $\gamma\gamma$ signal with a significance of 4.3 standard deviations. The $d\sigma/dp_T$, measured by UA2, shows good agreement with NLO QCD prediction. At the Fermilab Tevatron collider in 1993, the CDF collaboration presented the double-photon cross section to be $86 \pm 27(\text{stat}) \, ^{+32}_{-23}(\text{syst})$ pb [43]. With its high $\sqrt{s}$ (1800 GeV), the Tevatron collider can probe the region of low x_T, ranging from 0.01 to 0.04, and high Q^2, where perturbative QCD is found to work well.

Experiment	Analysis Method
R806	EGS Monte Carlo simulating γ π^0, R_s/R_π [a] > 1
AFS	Highly segmented NaI crystal walls, able to resolve $\pi^0 \rightarrow \gamma\gamma$
NA3	A MWPC[b] inside the calorimeter, using conversion probability matrix
WA70	A finely-grained calorimeter, both γ and π^0 modeled by a detailed Monte Carlo
UA1	Applying isolation cuts : E_T between R=0.7 and R=0.4 < 2 or 10%[c], and longitudinal shower profile fitting
UA2	A preshower detector, by using conversion probability, extracting the photon fraction f_γ statistically
CDF	A strip MWPC embedded in the calorimeter, transverse shower profile χ^2 used
This(DØ)	A fine-segmented calorimeter, fitting longitudinal shower profile

Table 1.3: Various analysis techniques used to extract photon signal from the overwhelming background

[a] R_s and R_π are characteristic quantities for signal and background showers respectively, see [37] for definition

[b] MWPC for multi-wire proportional chamber

[c] R is an isolation cone, see Fig.3.2 for its definition

In hadron-hadron collisions, the direct photon signal is contaminated by jet background, in which jets fragment into single energetic π^0 or η and some soft particles. Table 1.3 lists the various methods which are used by the different experiments(Table 1.2) to separate signals from background and extract the signal fraction.

In this thesis, a high statistics data set, the integrated luminosity $L = 82.36$ pb^{-1}, accumulated during Fermilab Tevatron collider 1994-1995 run, is used to study double-photon production with the DØ detector. The plan for this thesis is as follows. Chapter 1 describes the physics motivation. Chapter 2 describes in detail the DØ detector and each subdetector. Chapter 3 presents the algorithms and methods with which the particles and jets are reconstructed. Chapter 4 describes the core of the analysis, the data selection, the efficiency determination and the background subtraction. Chapter 5 presents the final differential cross section results, $d\sigma/dE_T^{\gamma}$, $d\sigma/dM^{\gamma\gamma}$, $d\sigma/dp_T^{\gamma\gamma}$ and $d\sigma/d\Delta\phi^{\gamma\gamma}$. The last chapter, Chapter 6, gives conclusion and summary.

Chapter 2

Experimental Apparatus

This chapter presents a description of the Fermilab Tevatron $p\overline{p}$ collider complex and the DØ detector. A complete and 'official' reference of the DØ detector can be found elsewhere [44]

2.1 The Fermilab $p\overline{p}$ Collider Complex

2.1.1 Accelerator Concepts

All accelerators employ electric fields to accelerate charged particles to high energy [45]. The energy gained by a charged particle is $\Delta E = Q \times V$, where V is the voltage gap of each accelerating electric field. The simplest accelerator is a d.c. high-voltage source, which can only achieve beam energy up to near 20 MeV. For higher energy, a high frequency a.c. voltage is implemented. In practice nowadays, microwave frequencies are employed to accelerate electrons and protons above MeV energies. It is accomplished either in a *linear* accelerator(*linac*), with a succession of accelerating elements in line,

or in the *cyclic* accelerator (*synchrotron*), by arranging particles to traverse a RF voltage repeatedly in a ring.

A *linac* [46, 47] consists of an evacuated pipe containing a series of drift tubes. Alternate tubes attach to either side of a radiofrequency (RF) voltage. The charged particles will get continous acceleration if the length of a drift tube is so chosen that the particles traverse the gap when the field force in the gap is along the direction of the particles. Such proton *linacs* are used as injectors for the later stages of cyclic accelerators. The final beam energy depends upon the voltage per cavity and the total linac length.

Most modern accelerators are circular. Charged particles are constrained in a vacuum pipe in the ring which is surrounded by magnets. The particles are accelerated by RF cavities once or a number of times per revolution. For a proton of momentum p, the magnetic field has to have a value of B (in Tesla) to keep the proton on a circular path of radius R (in meter):

$$p = 0.3 \times B \times R \tag{2.1}$$

Both the field B and the RF frequency must increase and be synchronized with the particle momentum as it increases, from which comes the term *synchrotron* [46, 47]. The maximum energy a particle can reach at a *synchrotron* is determined by the ring radius R and the maximum field B.

2.1.2 The Tevatron $p\overline{p}$ collider

The Tevatron, located near Chicago, is the world's first superconducting proton synchrotron [49, 50, 48]. The superconducting Tevatron magnets can

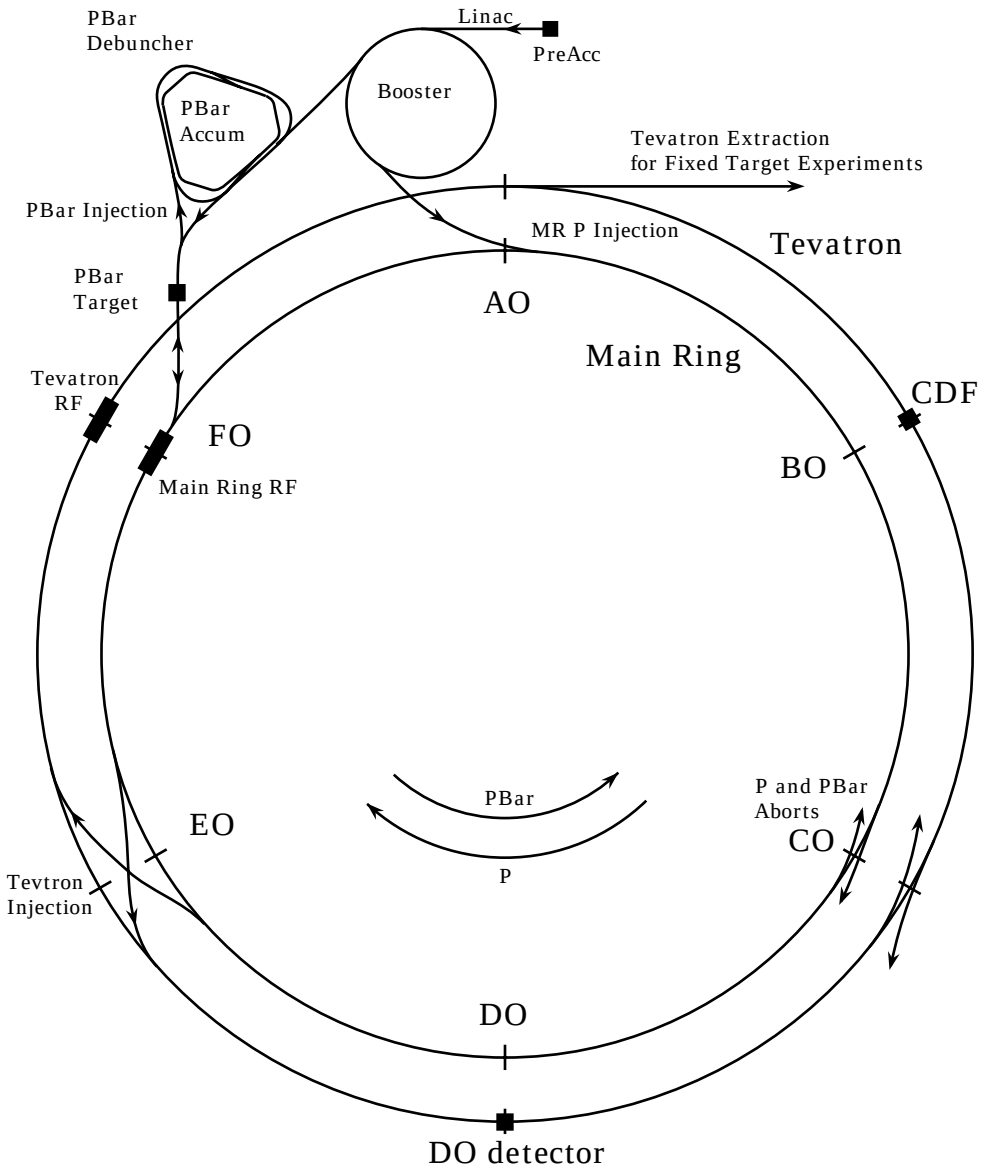

Figure 2.1: Schematic layout of the tevatron complex at Fermilab [48]

deliver a magnetic field (up to 5 T) more than three times as strong as its conventional counterpart, as the *main ring*, in the same tunnel of a radius $R = 1$ km (see fig. 2.1). According to equation 2.1, protons can be accelerated to 3 times or more higher energy at the Tevatron.

The proton beam originates from H^- ions which are released and accelerated to 750 KeV by an electrostatic Cockroft-Walton accelerator, part of the PreAccelerator (see fig. 2.1). The H^- ions are bunched and transported to a 150 m long linac, which boosts the energy of the ions to 400 MeV. The ions then pass through a carbon foil, which strips off the electrons and extracts the bare protons from the ions. The remaining protons are guided into the booster, a synchrotron of 159 m diameter, where the proton is propelled to 8 GeV. The protons are then injected into the main ring, which is a large synchrotron of radius 1 km, composed of conventional copper-coil magnets. Here the protons are boosted to an energy of 150 GeV.

Unlike the positron e^+, an intense beam of antiprotons $\overline{p}$ is much more difficult to generate. Fermilab creates antiprotons by extracting the protons from the main ring and smashing them onto a copper target. The antiprotons produced are guided into the first antiproton storage ring, known as the Debuncher, where they are cooled by debunching and stochastic cooling [51, 52]. Then they are sent to another storage ring, the Accumulator, to be cooled further for several hours until the antiproton number per bunch reaches the order of 50 - 150 $\times$ 10^{10}. A portion of the stored antiprotons is transferred to the main ring to be accelerated to 150 GeV.

Just below the main ring, in the same accelerator tunnel, lies a superconducting proton synchrotron, the Tevatron [50]. The Tevatron can boost protons or antiprotons to a maximum energy of 900 GeV (upgrades to the cryogenic system are expected to increase the maximum magnetic field B and to raise the maximum energy to 1000 GeV). The protons and antiprotons are injected out of the main ring into the Tevatron and squeezed into bunches. Before a "shot", the Tevatron ring is filled with six bunches of protons and six bunches of antiprotons, traveling in opposite directions at nearly the speed of light. The bunches of protons and antiprotons are accelerated to the maximum energy of 900 GeV and allowed to collide at the two collision points BØ and DØ every 3.5 μs. Each store lasts for about 20 hours.

2.1.3 Collider Luminosity

Though collider machines are more efficient at reaching high CMS energy (see Section 1.2.1), they possess some disadvantages. The beams must be stable, and the luminosity is much lower than at the fixed-target machines. For two oppositely moving beams, the interaction rate is given by:

$$R = \sigma \mathcal{L} \tag{2.2}$$

where σ is the cross-section and L, as the luminosity, is given by:

$$\mathcal{L} = fn\frac{N_1 N_2}{A} \tag{2.3}$$

where N_1 and N_2 are the numbers of particles in each bunch, n is the number of bunches in either beam around the ring, f the revolution frequency, and

A the cross-sectional area of the beams. L typically has a value near 10^{30} $cm^{-2}s^{-1}$.

At DØ, the instantaneous luminosity is measured by the Level-Ø counters [53]. When the Level-Ø counters register a firing rate $R_{L\emptyset}$, the luminosity is simply given as:

$$\mathcal{L} = \frac{R_{L\emptyset}}{\sigma_{L\emptyset}} \tag{2.4}$$

where $\sigma_{L\emptyset}$, known as *luminosity monitor constant*, is the $p\overline{p}$ cross section visible to the Level-Ø system.

The total $p\overline{p}$ cross section is composed of two major contributions, elastic and inelastic:

$$\sigma_{p\overline{p}} = \sigma_{el} + \sigma_{inel} \tag{2.5}$$

where the inelastic processes include single diffractive (SD), hard core (HC), and double diffractive (DD),

$$\sigma_{inel} = \sigma_{SD} + \sigma_{HC} + \sigma_{DD} \tag{2.6}$$

The DØ Level-Ø system has a different geometric acceptance for each of the processes. The counters are also not 100% efficient when they are hit. Taking into account all the effects, the visible total cross section to the DØ Level-Ø system, i.e. the *luminosity monitor constant*, can be measured as:

$$\sigma_{L\emptyset} = \epsilon_{L\emptyset}(\epsilon_{SD}\sigma_{SD} + \epsilon_{DD}\sigma_{DD} + \epsilon_{HC}\sigma_{HC}) \tag{2.7}$$

where $\epsilon_{L\emptyset}$ is the efficiency of the level-Øcounters. The cross sections σ_{SD}, σ_{DD} and σ_{HC} are the measurements of the experiments E710 and CDF (for original references for the two measurements, please see [53]). DØ use the

world-average values of the two available sets of the cross sections. For acceptance studies, two Monte Carlo samples with different physics processes were generated and put through the DØ detector simulation. Real DØ zero-bias data are then used to determine the overall Level-Ø firing efficiency, where zero-bias data are collected when no beam is present. A detailed list of all values and errors is given in [54, 55]. The resulting DØ *luminosity monitor constant* is given as:

$$\sigma_{L_\emptyset} = 46.7 \pm 2.5mb \tag{2.8}$$

In order to determine the cross section for a physics process, we usually run an experiment over a period of time and count the total number of events. It is given by:

$$N = \int \sigma \mathcal{L} dt = \sigma(\int \mathcal{L} dt) \tag{2.9}$$

The quantity $\int \mathcal{L} dt$ is the *integrated luminosity.* The integrated luminosity for this analysis is 82.36 ± 4.40 pb^{-1}.

2.2 The DØ Detector

The DØ detector is one of two detectors designed to study high energy $p\overline{p}$ collisions at the Tevatron (see fig. 2.1). The DØ detector is located at the collision point DØ in the Tevatron (fig. 2.1), and the other detector, CDF, is at BØ.

Because of the high energy processes at a $p\overline{p}$ collider, the DØ detector has to have sufficient depth to fully contain the high P_T particles which interact

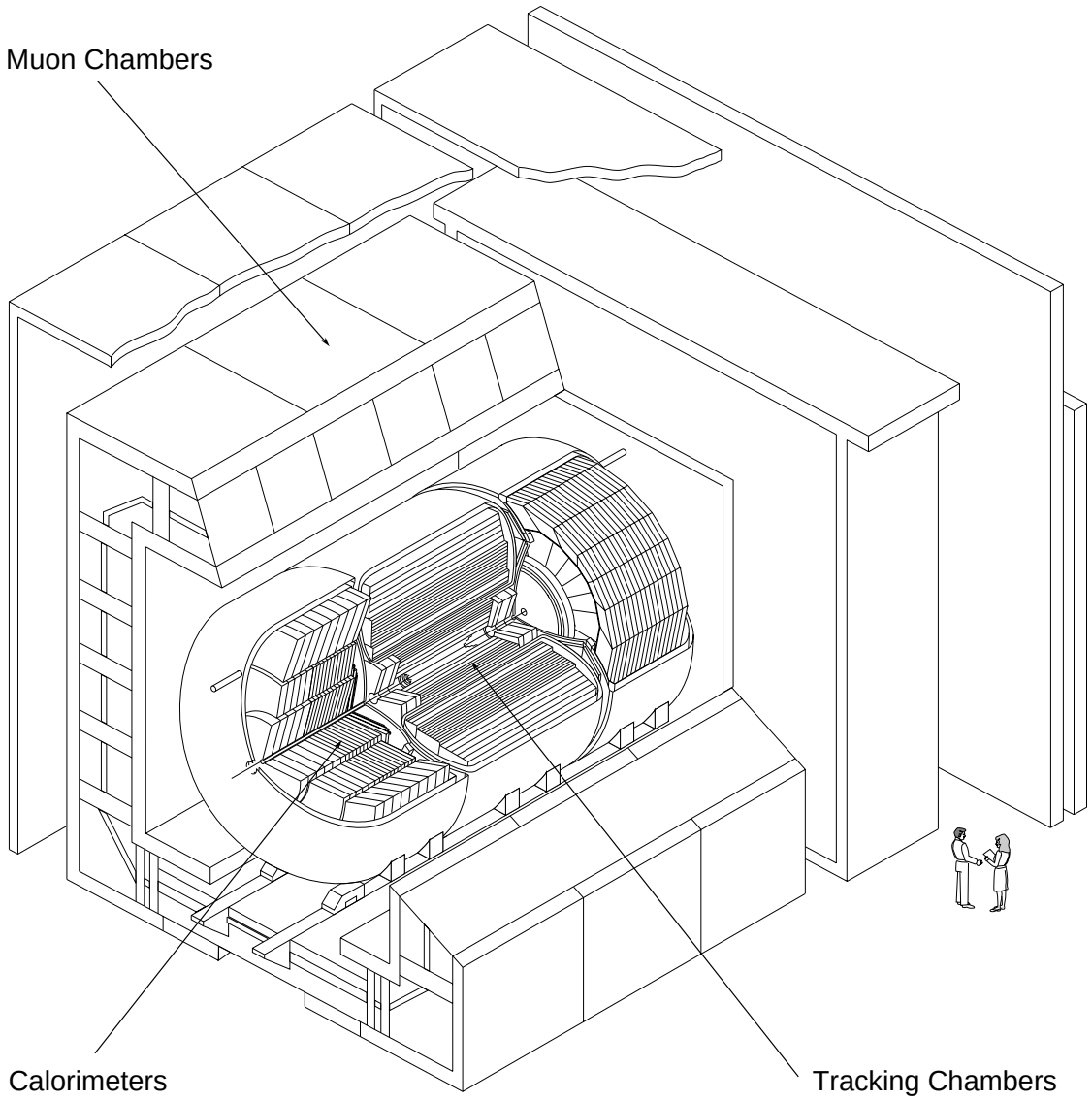

Figure 2.2: An isometric view of the DØ detector

with materials, like electrons, photons and jets, in each event. It also must employ a variety of detector techniques to measure and characterize these particles. The resulting detector is very complex, large and expensive, and takes hundreds of people and years of work to build. It is designed to be a general purpose detector, covering a wide range of physics topics, rather than being optimized for a single physics purpose. Driven by the type of physics to be studied, the DØ detector was optimized for high p_T phenomena and high mass states, focussing upon the detection of electrons, muons, jets and missing transverse energy. It consists of three major parts, the central tracking systems immediately surrounding the collision point, the calorimeters in the middle, and the muon systems outside the calorimeters (see Fig. 2.2).

2.2.1 Coordinate Systems at DØ

The DØ coordinate system is right-handed, where the positive z direction is aligned along the proton beam direction, and the positive x lies in the plane of the Tevatron ring and points outward from the center of the ring. Typical definitions for spherical coordinates (r,ϕ,θ) or cylindrical (r,ϕ,z) are used. For example, $\phi = 0$ points along the positive x and $\theta = 0$ along the positive z.

For highly relativistic processes, a quantity η, known as the *pseudorapidity*, is used in general, rather than the angle θ. It is defined as (for detail, see the kinematics chapter of [1]):

$$\eta = -\ln(\tan\frac{\theta}{2}) \tag{2.10}$$

In a $p\overline{p}$ collider experiment, the longitudinal momenta of the colliding

partons along the beam pipe are unknown. However, the transverse momenta can be well measured, and the vector sum of them must be conserved to be close to zero. It is therefore convenient to define the transverse momentum P_T as:

$$P_T = P \times \sin(\theta) \tag{2.11}$$

2.3 Central Detectors

The central detectors are comprised of the central tracking systems and the transition radiation detector (TRD). The layout of these detectors are shown in Fig. 2.3. The vertex drift chamber (VTX) immediately surrounds the beryllium beam pipe, and the transition radiation detector (TRD) is located outside the VTX to provide electron identification. Outside the TRD, there are the central drift chamber (CDC) and two forward drift chambers (FDC) to provide high tracking efficiency. Further details can be found in [56].

Since DØ is a non-magnetic detector, the tracking chambers don't need to measure the momenta of charged particles. All tracks are straight, regardless of whether the track is associated with a high momentum or a low momentum particle. The design goal is therefore to emphasize primarily on high tracking reconstruction efficiency, good spatial resolution and two-track resolving power, and good ionization energy (dE/dx) measurement which can be used to distinguish a single electron from a converted e^+e^- pair (mainly from γ or π^0 or η decay).

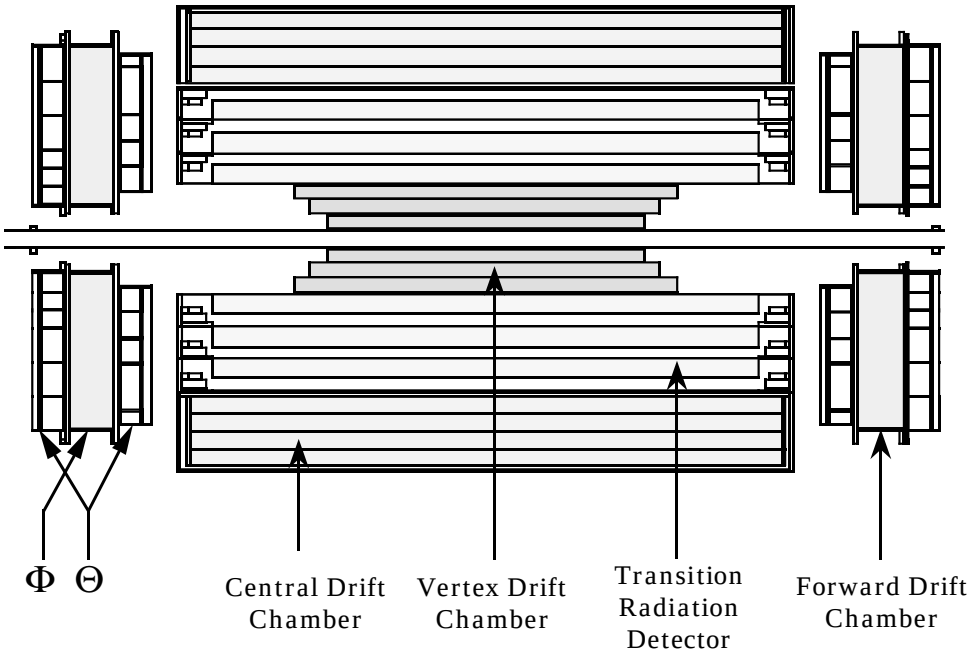

Figure 2.3: Side view of the central tracking systems and the transition radiation detectors

The central detectors are also used for a precise determination of the location of the $p\overline{p}$ interaction vertex for every event, and providing information about whether an event has a single $p\overline{p}$ interaction or multiple interactions. In order to fulfill these goals, the chambers need to have good spatial resolutions, both in ϕ and z. The following chapters will present more information about each detector.

2.3.1 Drift Chamber Principles

A good reference for drift chamber operation can be found in a review article by Sauli [57]. Here the basic ideas are presented.

A drift chamber is filled with gas as its active volume. When a charged

particle passes through the gas, it interacts with the electrons on the outer layer of the atoms and results in creating electron-ion pairs along the path of the particle. The number of the primary pairs created depends upon the energy and the charge of the particle, and the type of gas used in the chamber. For typical gases, nearly 100 electron-ion pairs are produced for every centimeter of a particle track. The amount of ionization pairs depends quadratically on the charge of the traversing particle, and only logarithmically on the energy. Two collinear particles, for example a converted e^+e^- pair from a photon, create twice the ionization. This can be used to indicate possible conversion of $\gamma \rightarrow\ e^+e^-$.

If an electric field is turned on, the electrons will start to drift to a set of positive anodes or sense wires. The sense wires have very small diameter. The electric field surrounding the wires is very strong and causes an avalanche of ionization pairs before the drifted electrons reach the anodes. This avalanche generates a measurable current at the positive anode, the size of which is proportional to the number of primary electron-ion pairs. The *gas gain* is defined as the ratio of the number of electrons collected at the anode to the charge of the particle which initiates this avalanche. It is very high, at the order of 10^4 - 10^6 for some practical chambers.

The position of the charged track is determined by measuring the drift time of the ionization electrons to the sense wire. The drift time is measured as the difference between the time when the particle traverses the chamber and the time when the electron reaches the sense wire. The drift time is then converted to a drift distance by using a detailed time-to-distance relation

map. The time-to-distance relation depends upon the type of gas used in the chamber, and the electric field strength map at all positions in the chamber. At DØ, the gas choice, the chamber geometry and the electric field (usually called HV) are all constrained by the 3.5 μsec bunch crossing time. To avoid pile-up, all ionized electrons must have reached the sense wire before the next beam crossing, i.e. the drift time must be less than 3.5 μsec.

In order to keep the time-to-distance relation simple, it is practical to create a drift electric field which is as constant as possible over a large volume, so that the drift electron velocity is nearly constant. Additional field-shaping electrode wires are applied to fulfill this goal. These wires are much thicker than sense wires, so that the surrounding field is not high enough to cause amplification. They are also applied near the sense wires to focus the field lines onto the sense wires and minimize cross-talk between adjacent anodes. In addition to the field, the choice of gas has a large effect on the performance of a drift chamber. The gas must not contain any highly electromagnetic components. Most drift chamber gases operate in *saturated* mode, in which the electron drift velocity is nearly independent of electric field strength. In the following, we will describe each chamber's special concerns and some chamber parameters relevant to the physics analysis.

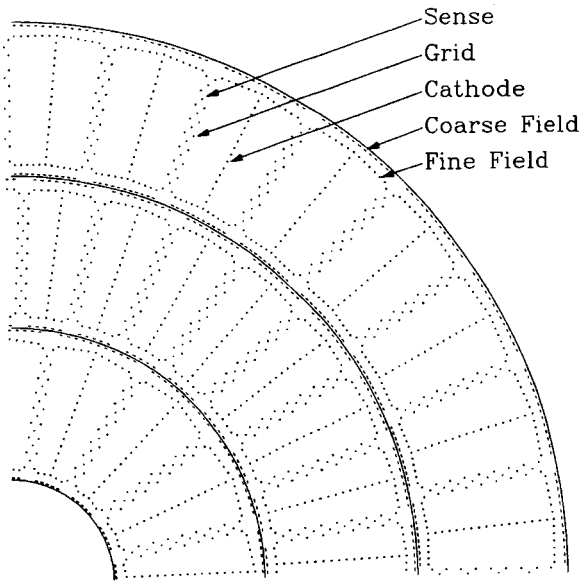

Figure 2.4: r - ϕ view of one quadrant of the VTX chamber, showing the layout of the sense wires and field-shaping electrodes.

2.3.2 Vertex Chamber

The Vertex chamber (VTX) [58] is the innermost tracking detector (see Fig. 2.4). It is just outside the beryllium beam pipe, and has three mechanically independent concentric layers of cells. Each layer is mounted on thin carbon fiber support tubes. Table 2.1 summarizes the geometry setup, the gas and the drift field used in the VTX chamber, and the chamber hit resolutions and efficiencies.

The vertex chamber uses a jet cell geometry for the drift cells, in which the sense wires are arranged in planes parallel to the paths of particles scattered from the interaction vertex, and the drift direction is azimuthal so that the measured drift distance provides the ϕ position of a hit of a charged track. Because the vertex chamber gas is run in unsaturated mode, the drift velocity

GEOMETRY	
Number of layers	3
Active radius	3.7 cm - 16.2 cm
Active z lengths of 1 - 3 layer	96.6 cm, 106.6 cm, 116.8 cm
Number of cells per layer	16, 32, 32
Number of sense wires	8 per cell, 640 in total
Sense wire separation	4.57 mm radially, 100 μm stagger within one cell
Sense wire specifications	25 μm NiCoTin, 80 g tension
Sense wire voltage	2.5 kV
Field wire specifications	152 μm gold-plated Al, 360 g tension
GAS and DRIFT FIELD	
Gas composition	CO_2 95%, ethane 5%, H_2O 0.5%
Gas pressure	1 atm
Gas operation	unsaturated mode
Average drift field	1 kV/cm
Drift velocity	low, $\approx 7.3\,\mu$m/ns
Maximum drift distance	1.6 cm
Gas gain	4×10^4
RESOLUTIONS and EFFICIENCIES	
Hit resolution along $r\phi$	≈ 60 μm
Isolated hit z resolution	≈ 1.5 cm
Two-hit resolving power	≈ 630 μm in $r\phi$ at 90% efficiency
Hit-finding efficiency	98%
Hit z-position finding efficiency	very low

Table 2.1: Vertex Chamber Parameters

is low in the VTX, which allows excellent spatial resolution and two-pulse separation along the drift direction $r\phi$ (see Table 2.1). Running in this mode, the drift velocity varies with drift field strength, and therefore care has been taken to determine the correct time-to-distance relation. The z position of each hit is measured using a charge division technique, the resolution of which is about 1.5 cm based upon test beam data. The basic idea of the charge division technique is that the resistive sense wire is read out at both ends and used as a voltage divider. Unfortunately, the method works well only when the sense wire pulses are well separated in space and the cell occupancy is very low. In the $p\overline{p}$ collider, the vertex chamber is next to the beam pipe, nearly all charged particles will travel through the chamber from the collision vertex. The high occupancy in the chamber causes a lot of overlapping hits, such that most of VTX hits have no z information at all. The three dimensional track-finding efficiency is very low.

2.3.3 Central Drift Chamber

The central drift chamber (CDC) [59, 60] is the outermost tracking detector in the central region, and covers a pseudorapidity range of $-1.2 < |\eta| < 1.2$ (Fig. 2.5). The chamber consists of four concentric layers and 32 azimuthal cells per layer. The chamber construction is modular, and the separate modules are positioned within a single support cylinder. The inner surface of the cylinder is a composite carbon fiber/Rohacell tube to minimize conversions, and the outer surface is 0.95 cm thick aluminum. A detailed list of the chamber

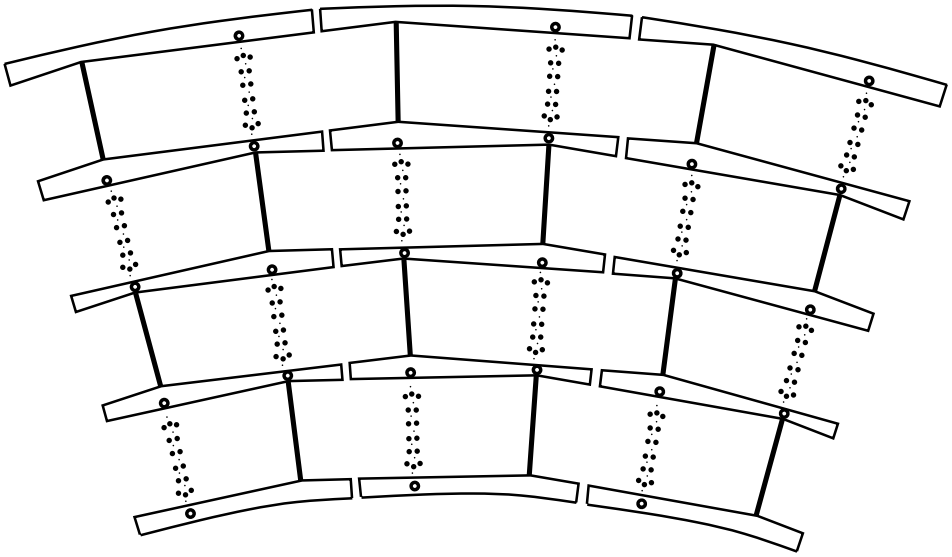

Figure 2.5: End view of three modules of the central drift chamber (CDC), showing the sense wires, the field-shaping wires and the delay lines

parameters can be found in Table 2.2.

Like the vertex chamber, the CDC has a jet cell geometry. The spatial resolution along the drift direction is around 200 μm, and two-pulse separation power is roughly 2 mm at 90% efficiency (see Table 2.2). The inductive delay lines are used to measure the z position of a hit. The delay lines are embedded in the inner and outer shelves of each cell, and propagate signals induced from the nearest neighboring sense wires. The z position of an avalanche can be determined by measuring the difference of arrival times at the two ends of a delay line. The spatial resolution along the delay line direction is around 2.5 mm. Since the CDC is far away from the beam pipe, the occupancy rate is reasonable, not like the situation with the VTX. The three dimensional track-finding efficiency is around 86%. The ionization energy dE/dx can be used to

GEOMETRY	
Number of layers	4
Active radius	49.5 cm - 74.5 cm
Active z lengths of 1 - 4 layer	184 cm, the same for all
Number of cells per layer	32, the same for all
Number of sense wires	7 per cell, 896 in total
Sense wire separation	6.0 mm radially, 200 μm stagger
Sense wire specifications	30 μm gold-plated W, 110 g tension
Sense wire voltage	1.45 kV (inner SW), 1.58 kV (outer SW)
Field wire specifications	125 μm gold-plated CuBe, 670 g tension
Number of delay lines	2 per cell, 256 in total
Delay line specifications	coil on carbon-fiber epoxy core
GAS and DRIFT FIELD	
Gas composition	Ar 92.5%, CH_4 4% CO_2 3%, H_2O 0.5%
Gas pressure	1 atm
Gas operation	saturated mode
Average drift field	620 V/cm
Drift velocity	$\approx 34\,\mu$m/ns
Delay line velocity	≈ 2.35 mm/ns
Maximum drift distance	7 cm
Gas gain	2×10^4 (inner SW), 6×10^4 (outer SW)
RESOLUTIONS and EFFICIENCIES	
Hit resolution along $r\phi$	200 μm
Isolated hit z resolution	2.5 mm
Two-hit resolving power	2 mm at 90% efficiency
Hit-finding efficiency	94 ± 2 %
3D track-finding efficiency	≈ 86%

Table 2.2: Central Drift Chamber Parameters

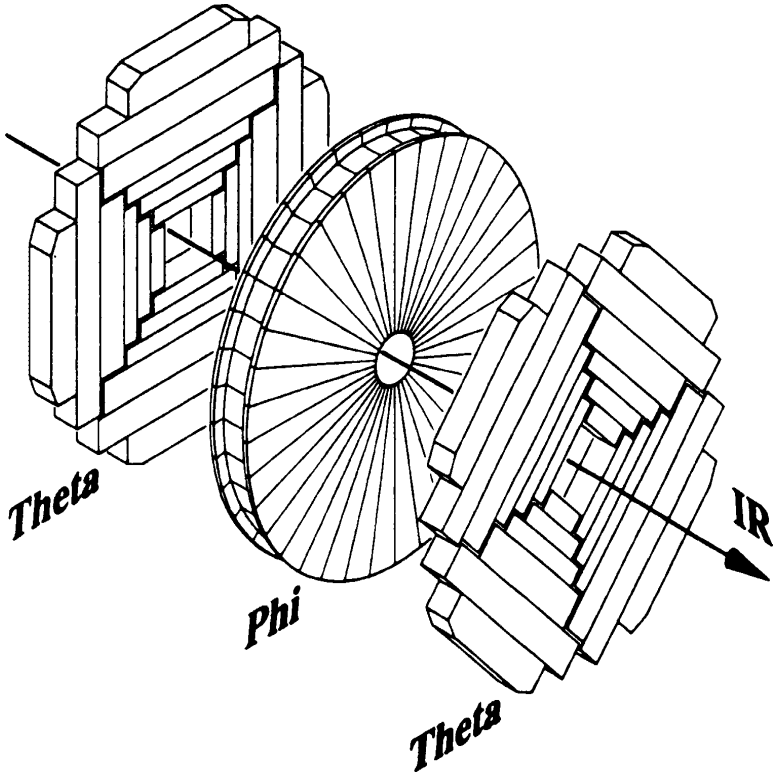

Figure 2.6: View of one Forward Drift Chamber, Its Θ and Φ Modules

indicate photon conversion, and so help to distinguish a single electron from a converted e^+e^- pair.

2.3.4 Forward Drift Chamber

The forward drift chambers (FDCs) [61, 62] extend the coverage for charged particle tracking down to $\theta \approx 5°$. There are two FDC chambers, located at either end of the concentric barrels of the central detectors and before the cryostat wall of the end calorimeters. Figure 2.6 shows a 3D picture of one of the FDC chambers. Each FDC consists of three separate chambers, a pair of Θ chambers and one Φ chamber sandwiched in the middle. The Φ

chamber is divided into 36 sectors azimuthally, each having 16 anode wires along the z-direction. Each Θ chamber consists of four mechanically independent quadrants, each of which has six rectangular cells. Each cell contains eight anode wires along z, and is equipped with one delay line identical to the CDC delay line. The FDC chambers operate with the same gas as the CDC, and the same drift field and gas gain. The drift distance resolution is roughly 200 μm in the Φ chamber, and 300 μm in the Θ chambers. A detailed list of parameters is given in the Table 2.3.

2.3.5 Transition Radiation Detector

The transition radiation detector (TRD) occupies the space between the VTX and the CDC, and provides independent electron identification in addition to that provided by the calorimeters. Transition radiation X-rays are produced when highly-relativistic particles ($\gamma > 10^3$) traverse boundaries between media with different dielectric constants. The DØ TRD is made of three mechanically separate units, each of which contains a radiator and an X-ray detection chamber. The energy spectrum of the X-rays is determined by the thickness of the radiator foils and the gaps between the foils. Each radiator section consists of 393 foils of 18 μm thick polypropylene in a volume filled with nitrogen gas. The mean gap between foils is 150 μm.

The detection of X-rays is accomplished in a two-stage time-expansion radial-drift PWC. The X-rays convert mainly in the first stage of the chamber, and the resulting charge drifts radially outward to the sense cells. In

	Θ Modules	Φ Modules
GEOMETRY		
Number of cells	4 quadrants per module 6 cells per quadrant	32 in total
Active radius	11 cm - 62 cm	11 cm - 61.3 cm
Active z lengths	104.8 cm - 111.2 cm 128.8 cm - 135.2 cm	113.0 cm - 127.0 cm
Number of sense wires	8 per cell, 384 in total	16 per cell, 512 in total
Sense wire separation	8.0 mm radially, 200 μm stagger	
Sense wire specifications	30 μm gold-plated W, 50 - 100 g tension	
Sense wire voltage	1.55 kV	1.66 kV
Field wire specifications	163 μm gold-plated AL, 100 - 150 g tension	
Number of delay lines	1 per cell, 48 in total	none
Delay line specifications	coil on carbon-fiber epoxy core	none
GAS and DRIFT FIELD		
Gas composition	Ar 92.5%, CH_4 4% CO_2 3%, H_2O 0.5%	
Gas pressure	1 atm	
Gas operation	saturated mode	
Average drift field	1.0 kV/cm	
Drift velocity	$\approx 40\,\mu$m/ns	$\approx 37\,\mu$m/ns
Delay line velocity	≈ 2.35 mm/ns	
Maximum drift distance	5.3 cm	
Gas gain	2.3×10^4 (inner SW) 5.3×10^4 (outer SW)	3.6×10^4
RESOLUTIONS and EFFICIENCIES		
Hit resolution along drift	$\approx 300\,\mu$m	$\approx 200\,\mu$m
track-finding efficiency	$\approx 92\%$	

Table 2.3: Forward Drift Chamber Parameters

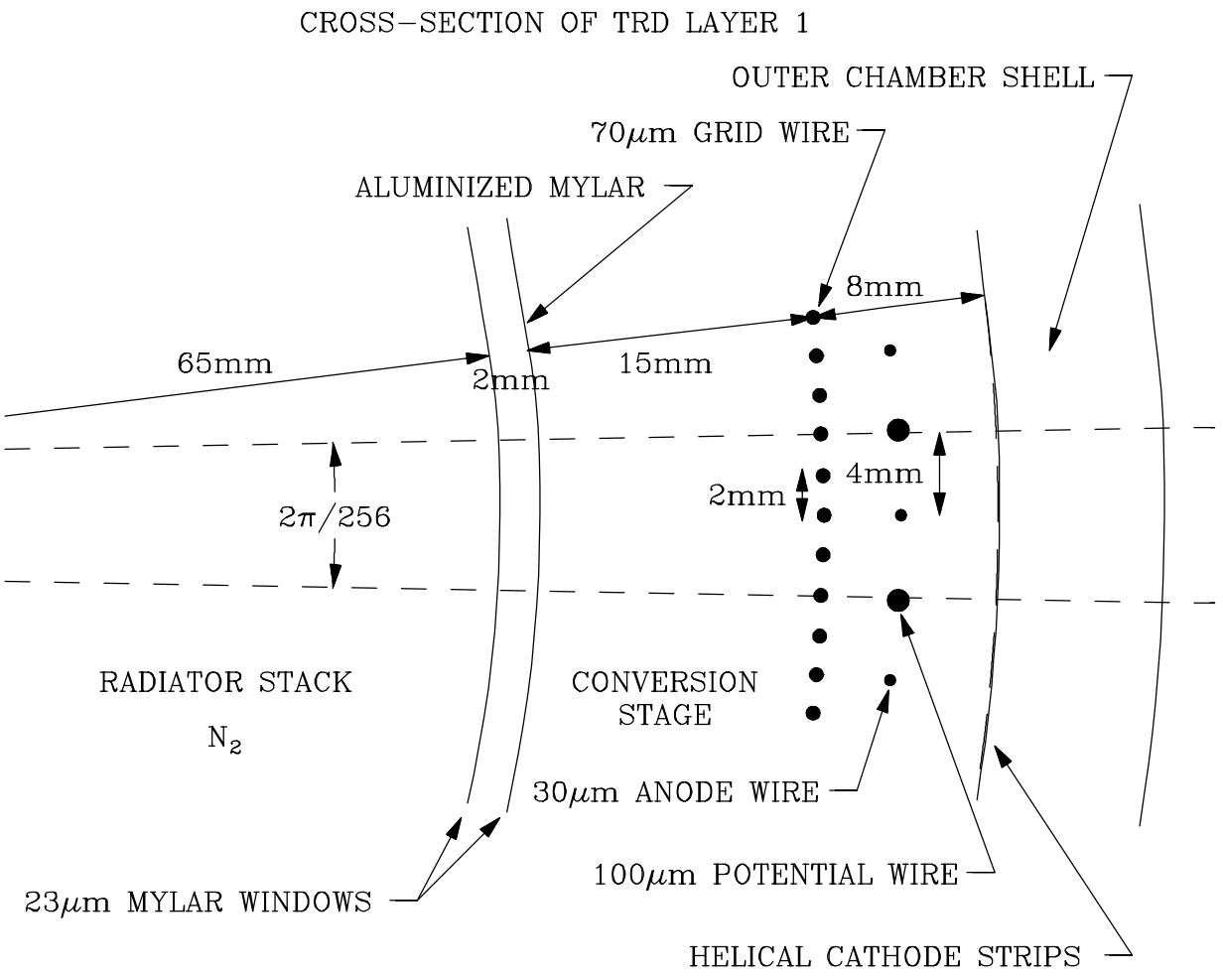

Figure 2.7: The TRD detector, showing the end of the polypropylene foil radiator sections.

addition to the charge deposited by the transition radiation X-rays, ionization is generated by all charged particles traversing the conversion and amplification gaps. The total energy deposited by electrons exceeds that deposited by pions of the same energy. A cut on the energy deposited can be used to gain an additional rejection factor over pions. See the references [63, 64] for detailed description and performance of the TRD.

2.3.6 Central Detector Readout Electronics

The readout electronics are almost the same for all CD detectors. There are three stages of signal processing. First the avalanche pulses from the sense wires, the delay lines and the TRD cathode strips are fed into preamplifiers mounted directly on the chambers themselves. Then the preamp output signals are carried via long cables of about 15 m length into pulse shaping cards, located on the platform underneath the detectors. Finally the shaper output signals are transported over 45 m cables to the moving counting house (MCH), where the analog pulses are sampled and converted into flash ADC counts (FADC). The digitized data are stored in a circuit, pending a decision from the trigger system. If an event satisfies the trigger requirements, the event data are then fed into a custom-made circuit to be zero suppressed. The zero-suppressed FADC are stored in memory, and are then transferred to the trigger computers for software processing. Further information can be found in [56].

2.4 Calorimeters

Since DØ has no central magnetic field, the calorimeters must provide the energy measurement for electrons, photons, jets and missing E_T, and play important roles in the identification of electrons, photons and muons and in the definition of jets. The calorimeters are crucial to the overall performance of the DØ detector and to its ability to get physics results out.

2.4.1 Calorimetry Principles

A calorimeter is a block of matter which is thick enough to intercept a particle traversing through it and make it deposit all its energy inside the detector volume in the subsequent cascade of low-energy particles [65]. Most of the incident energy turns into the form of heat. Some (usually small) fraction of the deposited energy is detectable in the form of scintillation light, or cherenkov light, or ionization charge, which is proportional to the energy of the incident particle. By finding the conversion constant using a single-particle test beam, the calorimeter can be used to measure the energy, and the resolution usually gets better as the energy becomes higher. According to the physics processes and the energy loss mechanisms, calorimeters can be classified into two types: electromagnetic and hadronic.

Electromagnetic Calorimeters

When high-energy electrons and photons (above 1 GeV) traverse a material, they lose energy primarily through bremsstrahlung for electrons and

e^+e^- pair production for photons. The emitted electrons, positrons and photons then undergo bremsstrahlung or e^+e^- pair production, and so on until the energy of all emitted particles has been degraded to the regime dominated by ionization loss. It is through a succession of these energy losses that the electromagnetic cascade or electromagnetic shower is formed.

The electromagnetic shower is well understood and fully described by quantum electrodynamics (QED). It depends essentially on the density of electrons in the absorber medium, and is nearly independent of the material. The energy loss ΔE in the length Δx can be expressed in terms of the *radiation length* X_0:

$$\frac{\Delta E}{E} = -\frac{\Delta x}{X_0} \tag{2.12}$$

The typical value of the *radiation length* is of the order of mm, and is about 3.2 mm for uranium for example.

Hadronic Calorimeters

In principle, the energy of hadronic showers can be measured in a way similiar to electromagnetic showers; but hadronic interactions have much greater variety and complexity in generating hadronic showers. There exists no simple analytical description of hadronic showers. The resulting detectable energy may depend upon the incident energy in a nonlinear manner. It is non-trivial to calibrate a hadronic calorimeter.

When hadronic particles pass through a medium, they lose energy mainly through inelastic collisions with atomic nuclei in the absorber. The collisions

generate secondary hadrons through nucleon excitation and break-up, which in turn undergo further nuclear inelastic collisions until all particles are stopped by ionization losses or absorbed by nuclear processes. In addition to nuclear interactions, a considerable amount of the secondaries are π^0, which will propagate through electromagnetically after decay. The scale of the energy loss can be described in terms of the *nuclear interaction length* λ. The equation analogous to that for the electromagnetic shower in (2.12) is:

$$\frac{\Delta E}{E} = -\frac{\Delta x}{\lambda} \tag{2.13}$$

The *nuclear interaction length* $\lambda = 10.5$ cm for uranium.

Signal Collection and Readout

After particles lose all their energy in the absorbers medium, some of the deposited energy turns into detectable signals, like the ionization charge in the DØ liquid argon calorimeter. These signals are collected at another medium, like the readout pad in the DØ calorimeter (see Fig. 2.8). The ratio of the collected energy over the incident energy is called the *sampling fraction.* One approach is to interleave layers of dense absorber with layers of signal-collection pads. This kind of '*sampling*' calorimeter allows considerably greater freedom in the optimization of detectors for specific applications, such as electron(photon)/pion discrimination, position determination, and good energy resolutions for electrons(photons) and jets.

The showering process converts a single high-energy particle into many low-energy particles. The total track length **T** for full absorption of the energy

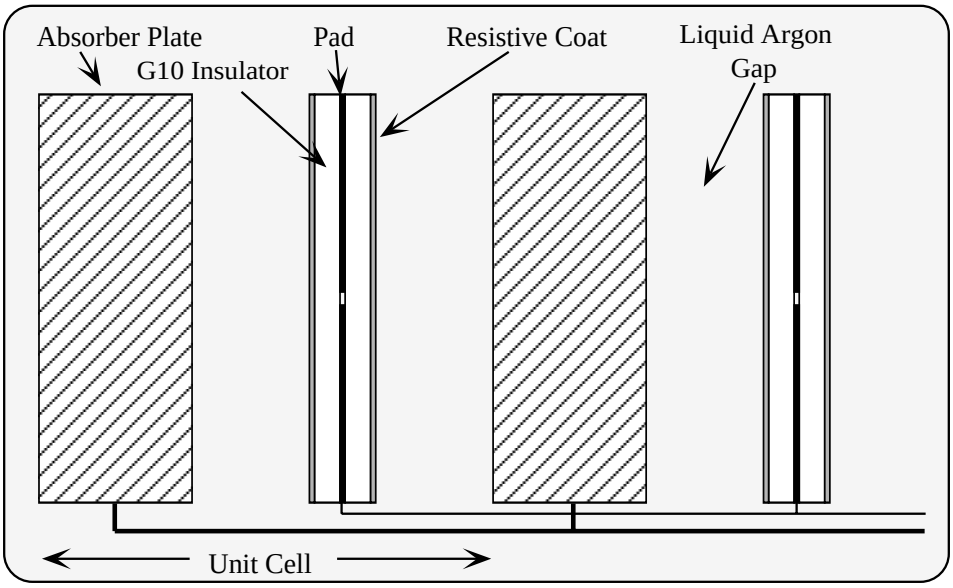

Figure 2.8: View of a unit cell in DØ liquid argon calorimeter, showing the absorber and readout plates.

is broken up into a 'tree' of many individual segments. The statistical fluctuation of the number of segments, N_s, contributes to the energy resolution.

$$\delta(E)/E \approx \delta(N_s)/N_s = 1/\sqrt{N_s} \tag{2.14}$$

where $N_s = E/\epsilon d$, ϵ being the critical energy and d the distance between active plates. The energy resolution $\delta(E)/E$ is therefore nearly proportional to $1/\sqrt{E}$, the higher the energy the better a calorimeter can measure it. The energy resolution for a single particle, like an electron or pion, can be well parametrized as

$$(\frac{\delta_E}{E})^2 = C^2 + \frac{S^2}{E} + \frac{N^2}{E^2} \tag{2.15}$$

The constants C, S and N describe the calibration uncertainties, sampling fluctuations and noise contributions.

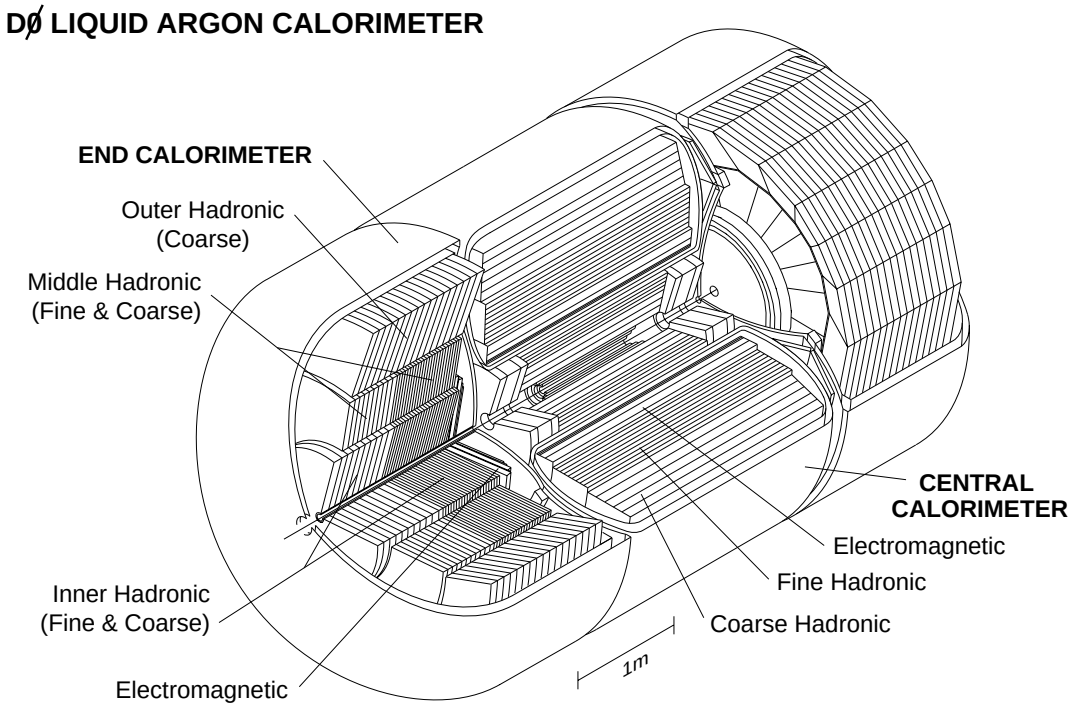

Figure 2.9: Isometric view of the central and two end calorimeters.

2.4.2 Geometry of DØ Calorimeters

The DØ calorimeters are *sampling* calorimeters, using liquid argon (LAr) as the active medium to sample the ionization produced in showers. Three distinct types of modules are used to optimize the responses for electrons , photons and jets, namely electromagnetic (EM) modules with relatively thin depleted uranium absorber plates, fine-hadronic (FH) modules with thick uranium plates and coarse-hadronic (CH) plates with thick copper or stainless steel plates. Fig. 2.9 shows the central and two end calorimeters, with three types of modules arranged in a ring. A typical unit cell is shown in Fig. 2.8.

Since uranium has a very high Z value, it takes less thickness to have sufficient amount of *radiation length* and *nuclear interaction length* to contain the showers. Therefore, the calorimeters are compact, and so is the whole detector. The calorimeters are designed to be as hermetic as possible, covering up to $\eta \approx 4.4$, and cracks and dead regions are minimized.

The electric field is generated by grounding the absorber plates and connecting the signal boards to a positive high voltage, which was 2.0 - 2.5 kV during the collider run. The ionized electrons will drift in the liquid argon gap between absorber plates and signal boards. The gap thickness was chosen to be large enough to observe a minimum ionizing particle and to avoid fabrication difficulties. The electron drift time across the gap is $\approx 450ns$. Limited by the accelerator bunch crossing time 3.5 μs, the sampling time of the pulse signals has to be less than 3.05 μs. This implies that each readout cell should have a capacitance less than 5 nF. The DØ calorimeters use a 'pseudo-projective' set of towers for readout. Fig. 2.10 shows the calorimeter segmentation pattern and the layout of readout towers. The size of one readout tower is $\Delta\eta = 0.1$ by $\Delta\phi = 0.1$. The readout cells in the third electromagnetic layer are twice as fine, spanning $\Delta\eta = 0.05$ by $\Delta\phi = 0.05$, because the electromagnetic shower development reaches the maximum there and so the fine segmentation can be useful to separate two EM showers close-by (for example, the two γ's from π^0 decay) and to determine the shower position precisely.

The DØ liquid Argon calorimeters are contained in cryostats. In order to have some access to the CD, the calorimeters are designed to be contained in three separate vessels, a central calorimeter (CC) and a pair of end calorimeters

Central Calorimeter Setup			
Module Type	CCEM	CCFH	CCCH
Num of modules	32	16	16
Active radius	84 - 105 cm	105 - 170 cm	170 - 224 cm
Active z length	265 cm	266 cm	230 - 268 cm
Active η	$\approx$ -1.1 - 1.1	$\approx$ -0.9 - 0.9	$\approx$ -0.6 - 0.6
Num of readout towers	24×2 per module, 1536 in total		
Num of readout layers	4 per tower	3 per tower	1 per tower
Cells per layer	1,1,4,1 per tower	1,1,1 per tower	1 per tower
Total readout cells	10368	3000	1224
Absorber plates [a]	D.U.	D.U.- Nb	copper
Signal boards	G-10 coated with carbon-loaded epoxy		
Absorber thickness	$\approx$ 3 mm	$\approx$ 6 mm	$\approx$ 46.5 mm
Signal thickness	2×0.5 mm		
Argon gap	2.3 mm		
Voltage across the gap	2.0 - 2.5 kV		
Electron drift time	$\approx$ 450 ns		
Radiation lengths X_0	2.0, 2.0, 6.8, 9.8	-	-
Nuclear interaction lengths	0.76 in total	1.3, 1.0, 0.9	3.2
RESOLUTIONS			
Energy resolution	$C^2 + \frac{S^2}{E_T} + \frac{N^2}{E^2}$		
Single electron[b]	$C = 0.015, S = 0.13\ (GeV)^{\frac{1}{2}}, N \approx 0.4\ GeV$		
Single pion[c]	$C = 0.041, S = 0.511\ (GeV)^{\frac{1}{2}}, N \approx 1.17\ GeV$		
Position resolutions (elec)[d]	$\delta(r\phi) = 0.26$ cm, $\delta(z) = 0.21$ cm		

Table 2.4: Central Calorimeter Parameters. [68]

[a] D.U. for depleted uranium, D.U.-Nb for uranium-niobium (1.7%) alloy

[b] Studies by W mass group [66]

[c] Results from Test Beam Studies [67]

[d] Studies using Plate level MC electrons

End Calorimeter Setup			
Module Type	ECEM	ECIFH (ECMFH)	ECICH (ECMCH,ECOH)
Num of modules	1	1(16)	1(16, 16)
Active radius (cm)	5.7 - 84 through 104	3.92(86.7) - 86.4(156)	3.92(86.7,158.7) - 86.4(156,221.7)
Active z (cm)	168 - 195	195(195) - 296(269)	296(269,159 to 195) - 372(349,317 to 353)
Active η	$\approx$ 1.5 - 3.8	$\approx$ 1.8(1.2) - 4.4(1.8)	$\approx$ 2.1(1.4,0.8) - 4.4(2.0,1.4)
Num readout towers	38 per $\Delta\phi = 0.1$		
Num readout layers	4/tower	4(4)/tower	3(3,3)/tower
Cells /layer/tower	1,1,4,1	1,1,1,1	1,1,1
Total readout cells	7488	5216(IH), 1856(MH), 960(OH)	
Absorber plates [a]	D.U.	D.U.-Nb	SS
Signal boards	G-10 coated with carbon-loaded epoxy		
Absorber thickness	$\approx$ 4 mm	$\approx$ 6(6) mm	$\approx$ 6(46.5,46.5) mm
Signal thickness	2$\times$0.5 mm		
Argon gap	2.3	2.1(2.2)	2.1(2.2,2.2)
Voltage across the gap	2.0 - 2.5 kV		
Electron drift time	$\approx$ 450 ns		
Radiation lengths X_0	0.3,2.6,7.9,9.3	-	-
Nuclear interaction lengths λ	0.95 in total	4.9(4.0)	3.6(4.1, 7.0)
Energy resolution	$C^2 + \frac{S^2}{E} + \frac{N^2}{E^2}$		
Single electron [b]	$C = 0.003 \pm 0.002$, $S = 0.157 \pm 0.005$ $(GeV)^{\frac{1}{2}}$, N $\approx$ 0.14 GeV		
Single pion [b]	$C = 0.032 \pm 0.004$, $S = 0.41 \pm 0.04$ $(GeV)^{\frac{1}{2}}$, N $\approx$ 1.28 GeV		
Position resolutions(e) [b]	vary as $\sqrt{E}$, ranging 0.8 to 1.2 mm		

Table 2.5: End Calorimeter Parameters. [70]

[a] D.U. for depleted uranium, D.U.-Nb for uranium-niobium (1.7%) alloy, SS for stainless steel.

[b] These are results from Test Beam Studies. [69]

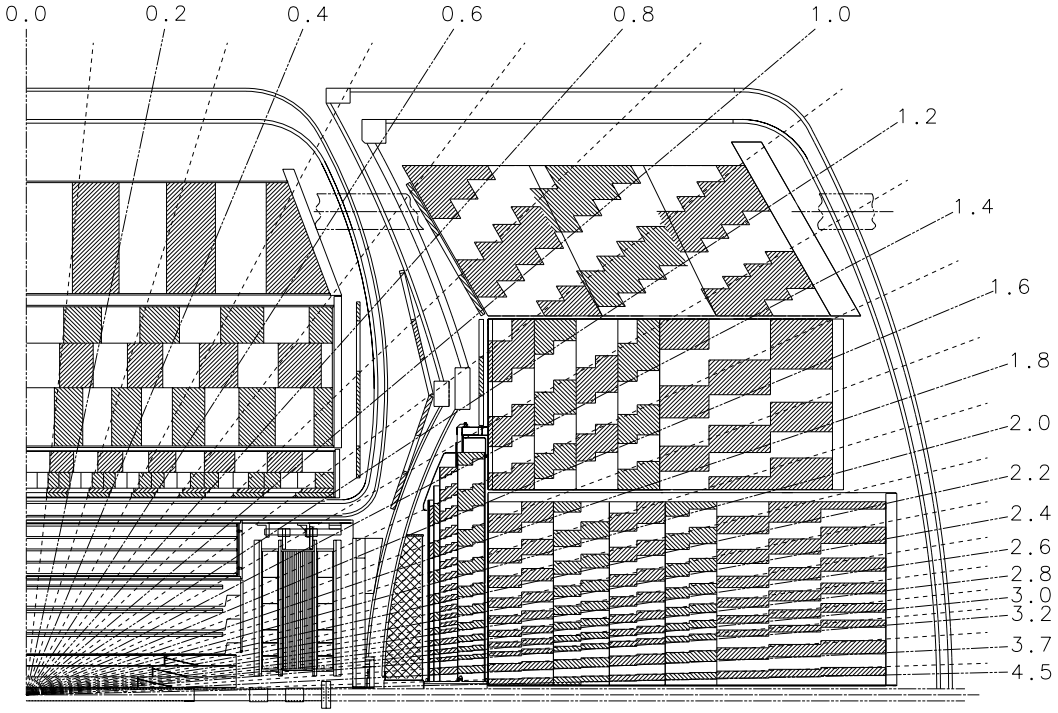

Figure 2.10: Schematic view of the calorimeters, showing the transverse and longitudinal segmentation pattern. The shading pattern indicates the 'pseudo-projective' set of cells ganged together to form readout towers.

(EC). The CC consists of three concentric layers of modules, the electromagnetic (EM), the fine hadronic (FH) and the coarse hadronic (CH). The parameters of the central calorimeter are compiled in Table 2.4. Like the CC, the EC is composed of four types of modules, the electromagnetic (EM) [71], the fine hadronic (IFH,MFH), the coarse hadronic (ICH,MCH) and the outer hadronic (OH). Table 2.5 gives the parameters for the EC. Fig. 2.11 shows the readout cell segmentation, transversely and longitudinally.

In figure 2.10, it can be seen that there is a large amount of uninstrumented material in the form of cryostat walls, stiffening rings, and module endplates between the CC and the EC, in the region $0.8 \leq |\eta| \leq 1.4$. Two

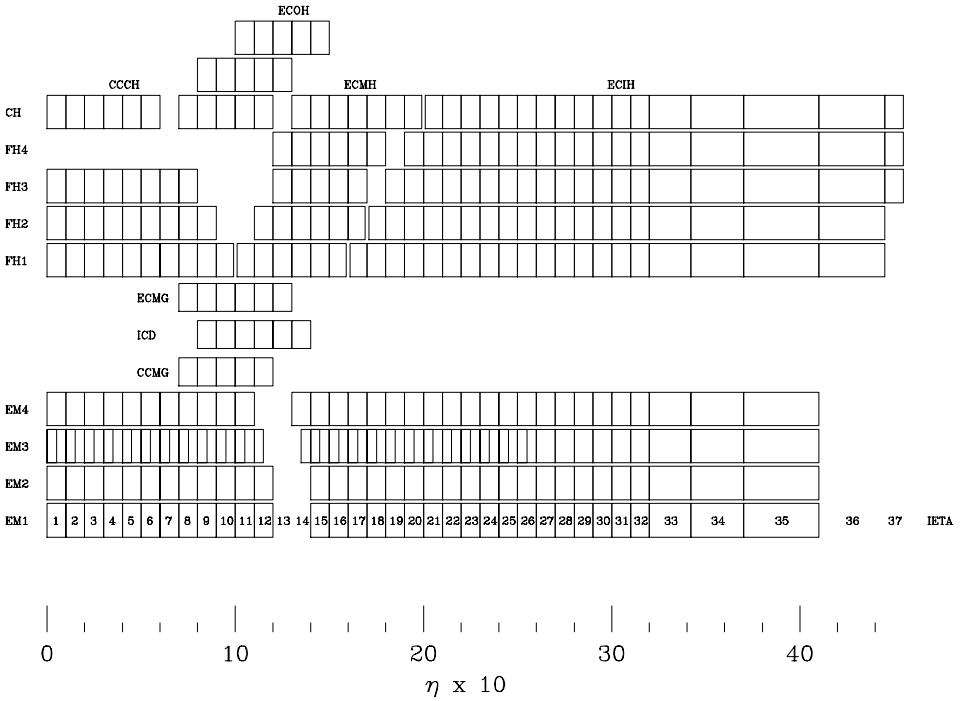

Figure 2.11: Diagram of calorimeters readout channels in depth and η

additional devices are implemented in the transition region to recover some of the energy deposited there. One is the massless gaps (MG), which are simply rings of signal boards mounted on the end plates of the CCFH, ECMH and ECOH modules. The other is the intercryostat detectors (ICD). The ICD consists of 384 scintillator tiles of size $\Delta\eta = \Delta\phi = 0.1$, being mounted on the front surface of the ECs.

2.4.3 Calorimeter Readout Electronics

Signals from the calorimeter modules are brought to the four feedthrough ports by specially fabricated cables [72]. The outputs from the feed-through boards are fed into hybrid preamplifiers mounted on the surface of each cryostat. The signals are then transported through 30 m long cables to the baseline subtractors (BLSs); the inputs are integrated (430 ns) and differentiated (33 μms). At the input to the BLS, a portion of the signals is extracted to feed into trigger towers with a size of $\Delta\eta \times \Delta\phi = 0.2 \times 0.2$. The rise time of this signal is $\approx$ 100 ns. The whole signal is sampled before a beam-crossing and 2.2 μs after, the difference of which is proportional to the charge collected on the readout boards. The BLS outputs are sent over 50 m long cables to the Moving Counting House (MCH), and are digitized in about 10 μs in 24-channel 12-bit ADC circuits. Roughly 4 MeV of deposited energy corresponds to one ADC count. The ADCs can also perform pedestal subtraction and zero-suppression for each channel. The ADCs are read into VME buffers which drive the data cables to carry data to the computers.

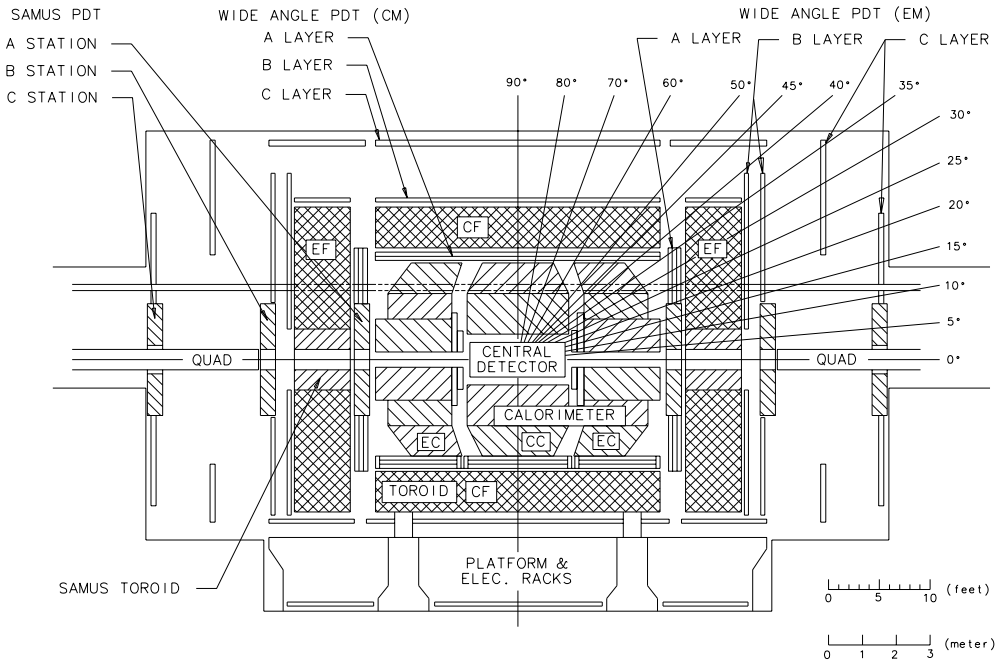

Figure 2.12: Side elevation of the muon system.

2.5 Muon System

The DØ muon system [73] consists of five separate iron toroidal magnets and sets of proportional drift chamber tubes(PDT) to measure tracks down to a polar angle of approximately 3° from the beam pipe(see Fig. 2.12). The system is responsible for the identification of muons from collisions (not cosmic muons) and determination of their trajectories and momenta. A closely spaced set of measurements of the muon track prior to the toroid provides the entry point; two sets of measurements separated by 1 to 3 meters after the toroid yield the exit direction. Since the relevant muons come from $p\overline{p}$ collisions, their incident trajectory is required to be a straight line, determined from a combination of the primary interaction vertex, the track seen in the central

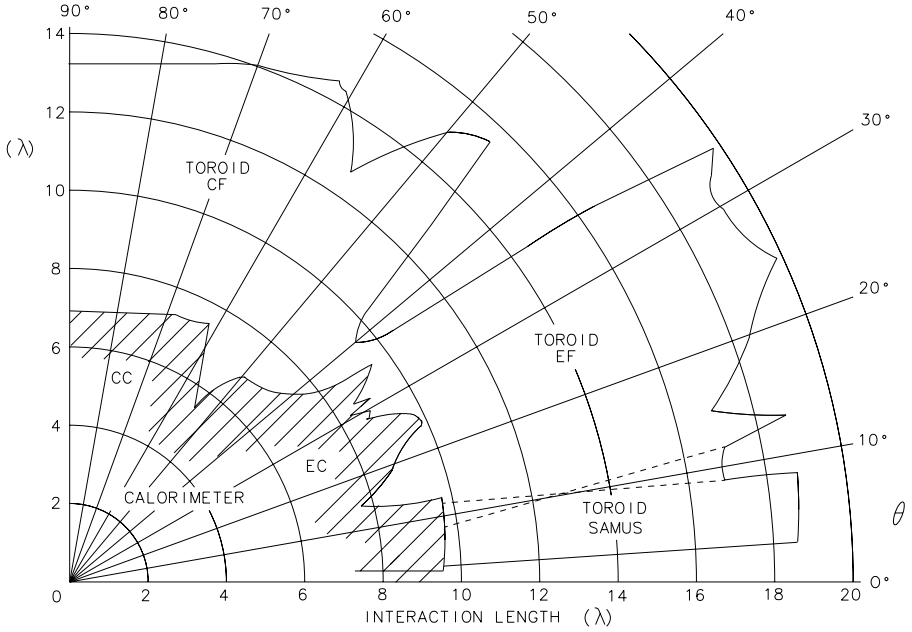

Figure 2.13: Number of *nuclear interaction lengths* as a function of polar angle.

detector, and the muon segments before the toroid. A minimum-ionizing trace in the calorimeter is also used as a confirmation for isolated muon tracks. After these selections, a relatively pure muon sample survives and their momenta are determined by measuring the bent angle through the 2 Tesla field between the incident and exit muon directions.

The five magnets are the CF (central Fe), the two EFs (end Fe), and the two SAMUS (Small Angle MUon System) magnets (Fig. 2.12). The CF and the EFs combined are referred to as the Wide Angle MUon System (WAMUS). Figure Figure 2.13 shows the amount of effective material in the calorimeters and toroids. Their 'thickness' varies from 13 at $\eta = 0$ to 18 *nuclear interaction lengths*. The large thickness allows only a small amount of background due to hadronic punchthrough. A factor weighing against the thickness include the

fact that only high momentum muons can make themselves through both the calorimeters and toroids. The muon momentum has to be greater than 3.5 GeV/c at $\eta = 0$, and greater than 5 GeV/c at high η.

2.5.1 WAMUS System

The WAMUS system comprises of 164 distinct proportional drift tubes, with size 2.5 $\times$ 5.8 m^2. The chambers are deployed in three layers: the "A" layer before the iron toroids and the "B" and "C" layers after. The distance between the B and C layers is $\geq$ 1 m, so as to provide a sufficient lever arm for an accurate measurement of the muon exit direction (see Fig 2.12).

The proportional drift tube (PDT) is the same for all WAMUS chambers, in the form of a rectangular cell with size 10.1 $\times$ 5.5 cm. The "A" layer has four planes of PDTs, and the "B" and "C" layers have three planes each. Cathode pad strips are attached to the top and bottom of each PDT cell, and a single anode wire is mounted at the center of the cell. A drift field is formed by holding the aluminum extrusion at ground and the cathode pads and anode wires at 2.3 kV and 4.6 kV respectively. The chambers are operated using a gas mixture of Ar(90%)CF_4(5%)CO_2(5%). The drift velocity is around 6.5 cm/μs. The wires are oriented along the primary $\vec{B}$-field direction ($\vec{B} \approx B\vec{\phi}$), and the drift direction is parallel to the pseudorapidity η. The drift distance resolution is $\approx$ 0.2 mm, which transforms to an "A" layer position resolution of $\approx$ 0.1 mm and the "B" and "C" layers position resolution of $\approx$ 0.17 mm.

The measurement along the wire direction is made using cathode pad

strips. Each strip contains two pads. With charges are induced at the cathode strips, the charge ratio of inner and outer pads provides a determination of the longitudinal coordinate. This method yields a hit resolution of about 2.0 mm.

2.5.2 SAMUS System

The SAMUS system [44] is also arranged in 3 layers, one preceding the toroid and two after. Due to the high occupancies in the forward regions, the SAMUS PDTs are smaller. The chambers are operated using $CF_4(90\%)CH_4(10\%)$ gas, with a drift velocity of about 9.7 cm/μs and a maximum drift time $\approx$ 150 ns. The drift resolution is $\approx$ 0.4 mm.

2.6 DØ Trigger System

The DØ trigger and data acquisition systems are designed to select and record interesting physics and calibration events. The trigger system has three levels of selection, the level Ø, the level 1 and the level 2, shown in Figure 2.14

2.6.1 Level Ø

The level Ø system consists of two hodoscopes of scintillation counters mounted on the front of the end calorimeters. The system is used to detect the presence of inelastic $p\overline{p}$ collisions, to make a fast measurement of the collision

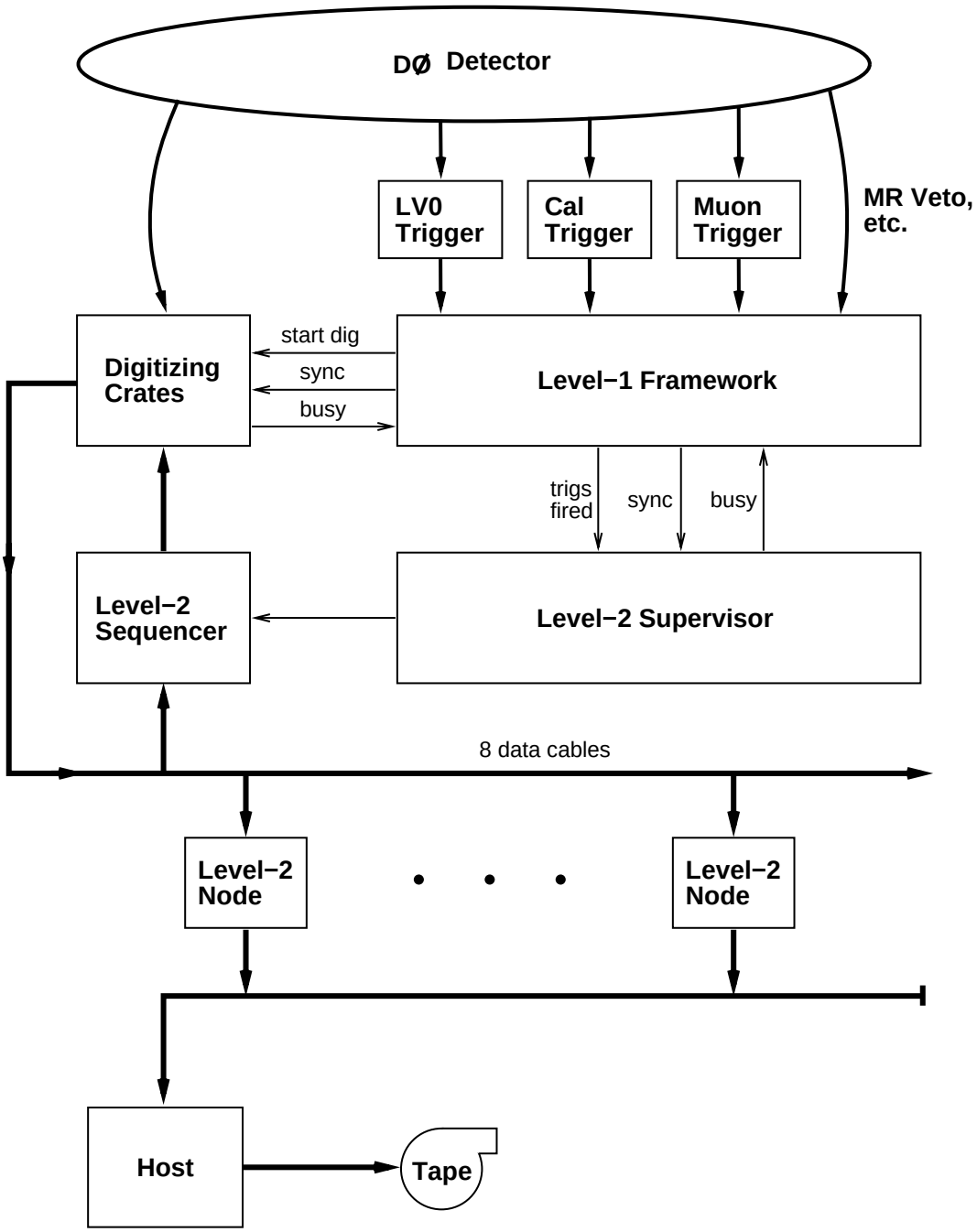

Figure 2.14: Block Diagram of the DØ Trigger System.

vertex, and also to serve as the luminosity monitor(see Section 2.1.3) for the whole DØ experiment. There is nearly complete coverage in the range 2.2 $< |\eta| <$ 3.9 and partial coverage between 3.9 $< |\eta| <$ 4.3. When an inelastic $p\overline{p}$ collision occurs, a large amount of activity and energy is generated in the forward region; so one looks for coincidence between the signals from the south and north counters. This requirement is more than 99% efficient for non-diffractive inelastic collisions. The collision vertex can also be determined by measuring the arrival time difference from the two scintilator arrays. A fast vertex determination can be accomplished with a resolution of 15 cm in less than 800 ns after a collision. A more accurate measurement is available within 2.1 μs, with a resolution of 3.5 cm. The level Ø firing rate is $\approx$ 150 kHz at an average instantaneous luminosity $\mathcal{L} = 5 \times 10^{30}$ cm$^{-2}s^{-1}$. The detection of the collision and the position of the vertex are then passed on to the next level trigger, the hardware trigger level-1, where the event rate is reduced to $\approx$ 200 Hz.

2.6.2 Level 1 Framework

At the heart of the DØ trigger system is the level-1 trigger framework [74, 75]. It is a very flexible and highly programmable hardware system that collects prompt detector data and makes a fast trigger decision. The system is synchronized with the beam crossings in the detector; most level-1 trigger decisions are made within the 3.5 μs time between crossings so that no deadtime penalty is incurred. Raw detector data is available from the central detector,

the calorimeters, the muon system and the level-Ø for the level-1 trigger to make decision.

The core of the level-1 framework is a two-dimensional fully programmable AND-OR logic network, incorporating 256 inputs, each of which is a latched bit containing specific detector information. The output has 32 terms, corresponding to the 32 specific level-1 triggers. Each of the triggers is formed by a logical state of the 256 inputs, requiring each bit in turn to be asserted, negated or ignored, depending upon the configuration of the trigger. The framework also provides the prescaling of some triggers too copious to pass through. A block of information is assembled by the framework, which summarizes the conditions leading to a positive level-1 decision, and is transported to the software level-2 trigger.

Level-1 Calorimeter Trigger

As described in Section 2.4.3, a portion of the signals before the BLS are fed into $\Delta\eta \times \Delta\phi = 0.2 \times 0.2$ level-1 trigger towers. Extending to $|\eta| = 4.0$, there are 1280 trigger towers in total; each tower is split into electromagnetic and hadronic sections, making up 2560 voltage signal pulses. Each pulse is analog-weighted in order to convert to a transverse energy and then digitized using a fast 8-bit flash ADC.

The digital information from the FADC provides the address for lookup memories, which store both electromagnetic and hadronic transverse energies for each trigger tower above thresholds. In addition, seven global energy sums, which are uncorrected electromagnetic, hadronic and total scalar E_T, corrected

electromagnetic, hadronic and total scalar E_T, and the missing $\not\!\!E_T$, are calculated and also stored in the lookup memories for more sophisticated analysis. Each global sum can be compared to 32 different thresholds, the results are used as input to the level-1 trigger framework AND-OR terms.

The trigger decision is very flexible. Besides using the global sums, the trigger decision can be made based on the transverse energy of an individual trigger tower. Each EM trigger tower E_T can provide an input to the level-1 framework by comparing to four programmable reference values. So can each hadronic trigger tower E_T, with comparison to four independently-selected reference values. There are also four reference values provided for the total E_T (sum of electromagnetic and hadronic) in each tower, resulting in twelve reference values which can be programmable for every individual trigger tower.

The interesting physics events consist of electrons, photons, muons, jets and neutrinos (neutrinos don't interact with the detector, being detected as unbalanced transverse energy). Except muons, all the objects leave considerable amount of E_T in the calorimeters, depending upon the level-1 calorimeter triggers to pick them up. For electrons and photons, any EM level-1 trigger is designed so that at least one EM trigger tower E_T has to pass a certain threshold, chosen as one of the four EM reference values, and the hadronic E_T of the same tower has to be less than a hadronic threshold. For jets, the total trigger tower E_T is compared to one of the total reference values. For each event having fired level-Ø, a global count of the number of EM and TOTAL trigger towers which have satisfied the requirements is evaluated, and the resulting count is then compared with up to 32 programmable count thresholds

to provide level-1 framework AND-OR input terms. The level-1 rate is $\approx$ 200 Hz.

2.6.3 Level 2

The level 2 trigger system is essentially a large farm of processors connected to the detector electronics by a set of eight 32-bit high-speed data cables. The level-2 system collects all detector and trigger block data at the rate $\approx$ 100 Hz after events have successfully passed the level-1 triggers, and then applies sophisticated software filters to the data to select interesting physics events, with an output rate of about 2 Hz.

The level-2 filter tools are designed to have large rejection factors while keeping the signal efficiencies reasonably high. Only the level-2 EM filters are relevant to the direct photon analysis, and the detailed algorithms will be described later in Section 4.1.1. If an event is passed by at least one level-2 filter, it is transferred to the host computer and written to tape (see Fig. 2.14).

Chapter 3

Event Reconstruction

When a proton collides with an anti-proton, produced are physics objects, like electrons, photons, muons, jets and missing $\not\!\!E_T$. These objects interact with the detector in different ways, and their presence and kinematics are recorded on tape in the form of raw data. The raw data of an event consists of digitized counts from the DØ detector: the central detectors, the calorimeters, the muon chambers, and the trigger block from level-Ø, level-1 and level-2. The process of turning the raw detector data into descriptions of objects is usually called *reconstruction*, using a program named *RECO*. The *reconstruction* process is very complicated, but crucial to any physics analysis; the double-photon cross section measurement in this thesis has to determine signal efficiencies and background contamination partially based upon what *RECO* does. This chapter will describe in detail the relevant processes in *RECO*. (For reference, see [76].)

3.1 Raw Detector Data

When an event passes the requirements of the triggers (level 1 and 2), fully digitized data are transported from VME crates onto eight high-speed data cables, each cable being responsible for one detector sector. The output data from the cables is mapped directly into the desired raw data ZEBRA [78] bank structure (see Table 3.1).

The central detectors have each signal flash-digitized in flash-analog to digital connecters(FADCs), one byte being written for every time slice that passes the zero-suppression algorithm. The volume of raw data from the CD is much bigger than that from the calorimeters or muon chambers (see Table 3.1). The size of the raw data limits the DØ data recording rate to only $\approx$ 2 Hz.

3.2 Calibration and Run Condition Monitoring

The digitized detector data need to be calibrated before they can be interpreted into meaningful quantities; calibration data include pedestals, gains and time information, which are usually stored in stand-alone databases. For each readout cell in the calorimeters, the raw ADC counts are converted into energy in GeV by a package called *CAHITS*. Assuming the pedestal is PED, the gain is G and the ADC-GeV convertion factor is A, a number of ADC counts X gives a deposited energy E:

$$E = A \times G \times (X - PED) \tag{3.1}$$

Raw Data Bank	Descriptions	Size(kB)
CDD1 Data Cable 3	Vertex Chamber (VTX) raw FADC and address from each sense wire	120
CDD2 Data Cable 4	Central Drift Chamber (CDC) raw FADC and address from each sense wire or delay line	115
CDD3 Data Cable 5	Forward Drift Chamber (FDC) raw FADC and address from each sense wire or delay line	150
CDD4 Data Cable 6	Transition Radiation Detector (TRD) raw FADC and address from each Cathode strip	125
CAD1 Data Cable 7	NORTH Section of Calorimeters raw ADC and address from each readout cell	15
CAD2 Data Cable 8	SOUTH Section of Calorimeters raw ADC and address from each readout cell	15
MUD1 Data Cable 2	All Muon Chambers: WAMUS and SAMUS raw ADC and address from each anode wire or cathode pad	25
TRGR Data Cable 1	Trigger Block from Level Ø, 1, 2	25

Table 3.1: List of eight raw data banks corresponding to eight data cables transporting data out of individual readout section.

For the CC electromagnetic calorimeter, A $\approx$ 4 MeV/ADC.

The calibration information can change with time due to drift of electronics, or the replacement of broken parts. Special calibration runs are taken every once in a while to keep the calibration data updated. The pedestals are measured for each channel when there is no input signal. For gain or time information, a well-known test pulse is distributed to each channel, and the pulse area or time is measured to determine the calibration constants. The electronics calibration was very stable and had low noise during the 1992 - 1995 collider run.

In addition, it is important to carefully monitor environmental and detector conditions while data are collected. Some conditions, including atmospheric pressure, temperature, voltages applied in the detectors, the liquid argon purity and etc., have to be taken into account to correct the calibration data. Occasionally, some runs are not used in the analysis because some sections of the detector were not under the right conditions.

3.3 Event Vertex Finding

In a $p\overline{p}$ collider detector, the transverse energy or momentum is a useful quantity to indicate the presence of a hard collision. For electrons, photons or jets, the calorimeter shower centers and event vertices are used to determine the direction of an object (all objects except muons travel through the DØ detector in a straight line); its transverse energy or momentum is calculated

as

$$E_T = E \times sin(\theta) \tag{3.2}$$

$$P_T = P \times sin(\theta) \tag{3.3}$$

where θ is the angle between the object trajectory direction and the beam line.

The determination of the interaction point or points (for multiple interactions) is very important. The (x,y) positions of the interaction vertex were found to be stable [79]; very little change is observed on a store-by-store basis. They are located at about 3-4 mm, and can be considered as (0,0) for most analyses. The z position(s) of vertex(vertices) are determined by using the tracks found in the central drift chamber (CDC) to extrapolate to the beam pipe. The CDC is rather far from the beam pipe (the inner radius of CDC is 49.5 cm), and therefore the z position resolution of a vertex is not so good.

3.3.1 Track Building

For each event, full tracking is applied to the CDC raw data bank CDD2. The track building procedures can be divided into three steps, which are hit-finding, segment-finding and finally track-building [56]:

- The raw data are unpacked, and a hit-finding algorithm [80] is applied to the unpacked data. The time and the pulse area are measured for each hit. Then the time is converted into a drift distance for each sense wire, and for each delay line, the time measurement is converted into a z-position on the delay line.

- The segment-finding process is applied to the hits within a single layer. Only the $r\phi$ positions of the found hits are used to find a segment; the z information is added onto the segment afterwards. First, a straight road in $r\phi$ is defined by two hits, one from an inner wire and the other from an outer wire, which spans the sector in a nearly radial direction. The width of the road is about 5 times the single-hit resolution and is fully efficient for segment-finding. All hits within the road are considered, and all possible combinations of hits from different wires are used for a straight-line fit and the smallest χ^2_{min} is stored for later use. If the χ^2_{min}/degree-of-freedom ≤ 10 and the number of hits used in the fit ≥ 5 (out of 7 wires in total), a segment is formed.

- After all segments are found, the track-building process is achieved by linking segments together and fitting a straight line through the CDC. In order to be linked, two different-layer segments must have nearly the same η and ϕ (i.e. being parallel to each other), and have a very small distance between their intercepts on the perpendicular bisector of the center points on the two segments. In general, at least three or more (four in total) segments are included in a link before a track can be formed; the final track fitting is performed by requiring a straight line fit using all the hits in the linked segments. If the fit has a good χ^2/degree-of-freedom, a CDC track is built.

3.3.2 Vertex z-position Determination

To determine the z-coordinate(s) of the interaction vertex (vertices) , each CDC track is projected back towards the center of the detector. The impact parameter is calculated for each track, which is defined as the minimum distance between the track and the beam-line. Only the tracks with small impact parameter (less than a cutoff value) are kept. The remaining tracks are then projected onto the (r,z) plane, and their intercepts on the beam-line are calculated and filled into a histogram. The rms width of the histogram is compared to a cutoff value; only those histograms with an rms width exceeding the cutoff are considered as possible multiple interaction candidates and then a search for more vertices will be carried out. The outlying regions in the histogram, with the distance more than the rms width away from the mean, are used to find other clustered distributions. One additional vertex is recorded for each cluster if the cluster includes three or more tracks, and the vertex z is computed as the mean of the intercepts of all the tracks in the cluster. For an event with more than one vertex found, the cluster including the highest number of tracks is ordered as the primary vertex.

Using the above method, the z position resolution of the vertex is around 1-2 cm if only one vertex is found. Multiple vertices can be separated if they are more than 7 cm apart.

3.4 Photon and Electron Identification

Photons and electrons induce narrow localized electromagnetic showers when they pass through the calorimeters (see Section 2.4.1). Their shower shapes are usually different from that of jets, except those few jets dominantly fragmenting into a leading-energy π^0 or η. Since the TRD is not widely used, DØ makes full use of the fine segmentation of the calorimeters, and the identification of photons and electrons is achieved using their detailed longitudinal and transverse shower profiles. In addition to the calorimeters, the central tracking chambers are used to classify an EM cluster as an electron when one or more charged tracks are pointing to the cluster, and to classify an EM cluster as a photon when no trace is found in the tracking chambers. At the $p\overline{p}$ collider, jets are produced copiously and form an overwhelming background to photons and electrons. In order to reduce the background, a tracking road is built between the interaction vertex and the EM shower center of a photon, and the number of 2D and 3D hits in the tracking chambers are counted and required to be low for a photon; this is later referred to as the 'hits-in-road' cuts.

3.4.1 Preliminary Candidate Finding

After ADC counts of each calorimeter cell are converted into energy (see Section 3.2) and primary event vertex is determined, the energies of the cells within each tower are summed to form the energy of the tower and the

E_T's of the cells (here E_T of each cell is calculated assuming the primary vertex) are summed to be the E_T of the tower. Based upon the towers (not cells), the preliminary photon and electron candidates are constructed by building EM clusters as follows:

- All towers are sorted according to their E_T, and a nearest-neighbor (NN) algorithm [81] is used to construct clusters from the towers. Starting from the highest E_T tower, a loop over all the eight neighboring towers is made to find the highest energy one, which will be connected to the center tower if its energy is above a threshold, chosen as 50 MeV. Going to the next tower, the same process is applied to all the eight neighboring towers except the ones which have already been connected, and so on for all towers. All the towers connected form one cluster.

- After each cluster is constructed, its EM fraction is calculated, which is defined as the sum of the energies of all the cells in the EM layers 1-4 divided by the sum over the EM layers 1-4 and the FH layer 1. The EM fraction must be $\geq 90\%$ before the cluster can be considered as an EM cluster. For high P_T objects ($\geq$ 10 GeV), an EM cluster becomes a photon or an electron candidate when its E_T is greater than 1.5 GeV and at least 40% of its energy is contained in the hottest tower of the cluster.

For each found EM cluster, its kinematic quantities are computed and the centroid of the shower cluster is determined using the cells in the EM layer 3. When the DØ detector was turned on to collect data in 1992, an algorithm

was used to calculate the centroid of a shower $\vec{x_{cos}}$ as the log-weighted center of gravity:

$$\vec{x_{cos}} = \frac{\sum_{i=cells} w_i \times \vec{x_i}}{\sum_{i=cells} w_i} \tag{3.4}$$

where the weight w_i was optimized as $w_i = max(0,\ w_0 + \ln(E_i/\sum_{j=cells} E_j))$; the parameter w_0 was chosen to optimize the position resolution [82].

A systematic bias in the z position of the centroid was discovered later (for details, see [83]), and a new algorithm using "Big Cells" instead of single cells was implemented and applied to all the data to be reported by this thesis. All cells are combined to build two types of "Big Cells", one type is constructed by cutting the CC into 256 equal slices along the ϕ direction and all the cells within one slice are summed up to make one $\phi_{\phi bc}$ "Big Cell":

$$\phi_{\phi bc} = \Big(\sum_{i=cells}^{one\ \phi\ slice} \phi_i\Big)\Big/\Big(\sum_{i=cells}^{one\ \phi\ slice}\Big) \tag{3.5}$$

$$E_{\phi bc} = \sum_{i=cells}^{one\ \phi\ slice} E_i \tag{3.6}$$

The log-weighted centroid of the shower ϕ_{cos} is,

$$\phi_{cos} = \Big(\sum_{i=\phi bc}^{256} w_i \times \phi_i\Big)\Big/\Big(\sum_{i=\phi bc}^{256} w_i\Big) \tag{3.7}$$

where the weight w_i is $w_i = max(0,\ w_0 + \ln(E_i(bc)/E_{tot}))$. The other type is through making 80 equal slices of the CC along the η direction and all the cells within one η slice are combined to build one $z_{\eta bc}$ "Big Cell":

$$z_{\eta bc} = \Big(\sum_{i=cells}^{one\ \eta\ slice} z_i\Big)\Big/\Big(\sum_{i=cells}^{one\ \eta\ slice}\Big) \tag{3.8}$$

$$E_{\eta bc} = \sum_{i=cells}^{one\ \eta\ slice} E_i \tag{3.9}$$

The log-weighted centroid of the shower z_{cos} is,

$$z'_{cos} = (\sum_{i=\eta bc}^{80} w_i \times z_i)/(\sum_{i=\eta bc}^{80} w_i) \quad (3.10)$$

where the weight $w_i = max(0,\ w_0 + \ln(E_i/E_{tot}))$. Finally the 3-d position(x_{cos},y_{cos},z_{cos}) of the center-of-shower is determined as

$$x_{cos} = R \times cos(\phi_{cos}) \quad (3.11)$$

$$y_{cos} = R \times sin(\phi_{cos}) \quad (3.12)$$

$$z_{cos} = z'_{cos} - \Delta z \quad (3.13)$$

where R is the radius of the calorimeter EM layer 3, and the correction Δz is to fix the θ-dependent z bias (for details, see the source code d0$calor_util$source:cm3pos_pv.for). The resulting resolutions for the shower centroid are $\Delta(r\phi) = 0.26$ cm, $\Delta(z) =$ 0.21 cm (see Table 2.4).

After the center of a shower is found, a straight road for tracking is built between the cluster centroid and the event vertex. The size of a road is

$$\Delta\phi = 0.1 \quad (3.14)$$

$$\Delta\theta = max(0.1, \frac{\theta_+ - \theta_-}{2}) \quad (3.15)$$

where

$$\theta_+ = tan^{-1}(\frac{R}{z_{cos} - z_{vertex} - 5\delta z})$$

$$\theta_- = tan^{-1}(\frac{R}{z_{cos} - z_{vertex} + 5\delta z})$$

δz the error of the vertex z position.

Looping over all the tracks constructed during track-building (see Section 3.3.1), the *RECO* program will identify the EM cluster as an electron candidate if at least one track is found in the road; otherwise, it becomes a photon candidate.

3.4.2 Tight Identification Cuts

The algorithms to find photon and electron candidates are chosen to be highly efficient for signals ($\approx 99\%$), and therefore allow a fair amount of background to get into candidate samples. Further cuts need to be applied to the data, and can be tuned for one particular analysis by optimizing the signal-to-background ratio. Here we will concentrate on photon identification for the purpose of this thesis; the electron identification(ID) is similar except it requires that at least one track is found in the road between the cluster and the primary vertex and the shower centroid matches the extracted track (see [84, 85]). Photon Identification is accomplished using three types of variables: the shower profile quantity "H_matrix χ^2", isolation quantity E_T^{iso}, and "Hits-in-road" quantities.

H_matrix χ^2

The DØ calorimeter is finely segmented, and the EM showers generated by photons can be distinguished by their profiles both longitudinally and transversely. To recognize the energy-distribution pattern, such as the fraction of energy in a given layer and in a certain cell within the shower maximun EM

layer 3, a covariance matrix V of 41 observables x_i is constructed [86, 87, 88]. The matrix elements are defined as

$$V_{ij} = \frac{1}{N}\sum_{n=1}^{N}(x_i^n - \bar{x}_i)(x_j^n - \bar{x}_j) \tag{3.16}$$

where x_i^n is the value of the ith observables for the nth electron and $\bar{x}_i$ is the mean of the ith observable. The 41 observables are the fractional energies in EM layers 1, 2, 4, the fractional energies in EM 3 cells of a 6×6 array centered on the hottest tower, the event vertex z and the logarithm of the total cluster energy. The matrix elements are determined using training samples and are then stored as a data file. DØ uses 37 independent training samples, each for one IETA tower (total 37); each sample consists of single electrons with energies evenly ranging between 10 and 150 GeV and their event vertex smeared as a gaussian. The sample is run through a detailed Plate-level Monte Carlo shower simulation [96]. There are 37 matrices in total.

The *H-matrix* is the inverse of the covariance matrix $\mathbf{V}$, $\mathbf{H} = \mathbf{V}^{-1}$. To measure how closely an EM shower resembles a true electron, taking into account the energy distribution profiles and all correlations, we can define a quantity called *H_matrix* χ^2:

$$\chi^2 = \sum_{i,j=1}^{41}(x_i^{candi} - \bar{x}_i) \times H_{ij} \times (x_j^{candi} - \bar{x}_j) \tag{3.17}$$

Fig. 3.1 shows a comparison of the distributions of H-matrix χ^2s for 'electrons' and EM 'jets'. The samples of electrons and their background are selected in the following steps:

1. requiring at least two or more preliminary photon(or electron) candidates in total.

2. each candidate must have $E_T > 10$ GeV.

This makes up a sample of nearly all EM jets, as demonstrated in the plot (b1) of Fig. 3.1. The plot (b1) shows the mass spectrum of two leading E_T candidates; its shape is like the QCD Dijets mass spectrum except a little resonance bump from $Z \rightarrow ee$. Based upon this sample, more clean-up cuts are applied:

1. requiring both candidates are electrons, and the significance S of the match of the track and the shower centroid must be $S < 5$. Here S is defined as $S^2 = (\frac{\Delta R\phi}{\sigma_{r\phi}})^2 + (\frac{\Delta z}{\sigma_z})^2$

2. H-matrix χ^2 cut: $\chi^2 < 100$, and isolation E_T^{iso} cut: $E_T^{iso} < 2$ GeV.

3. a window cut on the pair mass: $80 < M_{ee} < 100$.

From the plot (b1), the sample selected within the mass window (the shaded area) is a highly enriched electron sample, the background of which is less than 10%. This sample will be used for later efficiency studies.

Isolation E_T^{iso}

The overwhelming source of background to direct photons is the production of high P_T electromagnetic jets when they fragment into one or more high P_T π^0 and η which decay into photon pairs so close to each other that each pair cannot be resolved. Direct photons are colorless objects, usually produced as isolated EM showers, whereas the jet background comes from the color object partons which fragment into multiple particles. Therefore an 'isolation cut' is

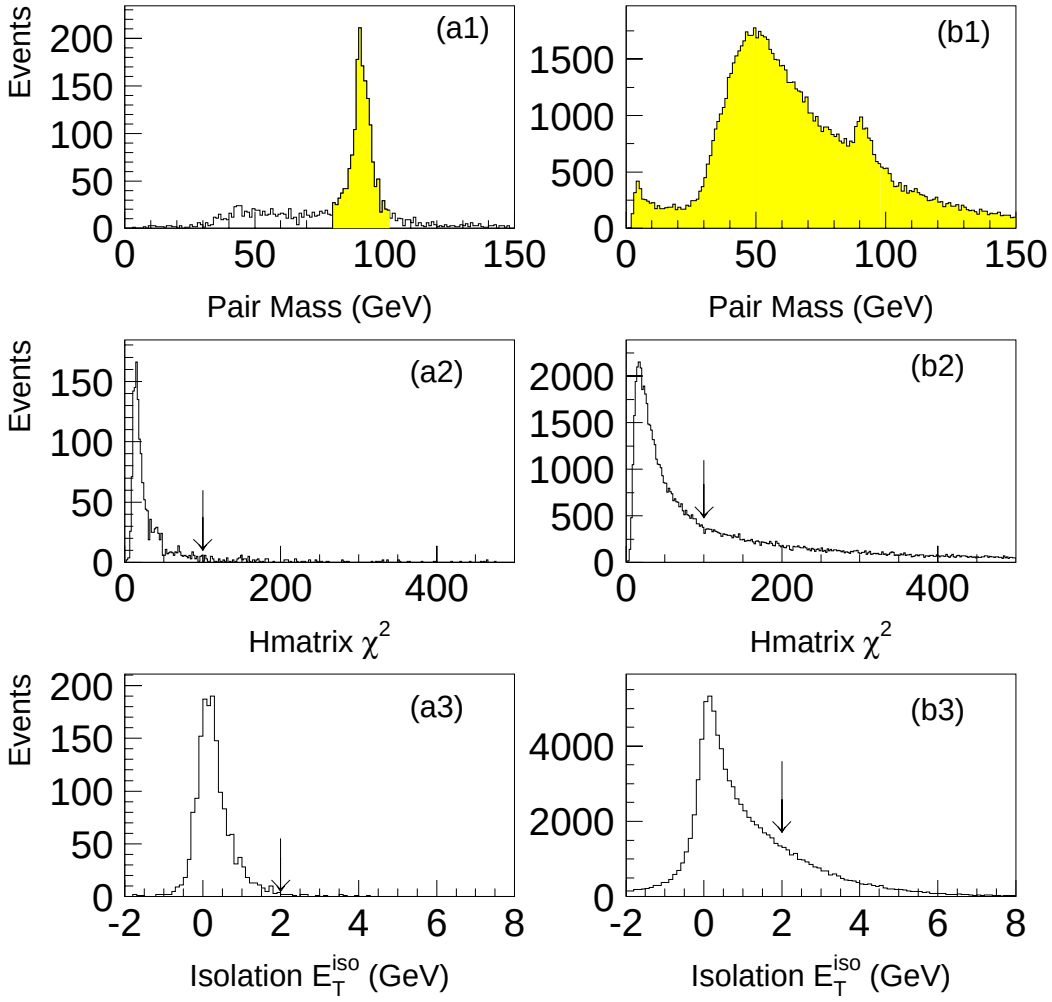

Figure 3.1: The distributions of H-matrix χ^2 and isolation E_T^{iso}. Fig.(a2) and (a3) are for clean electrons from Z $\rightarrow$ ee decays, whose mass spectrum is the shaded area in figure (a1); Fig.(b2) and (b3) are for an electron background sample composed mainly of EM jets, whose mass spectrum is shown in figure (b1). The arrows indicate where the selection cuts are placed.

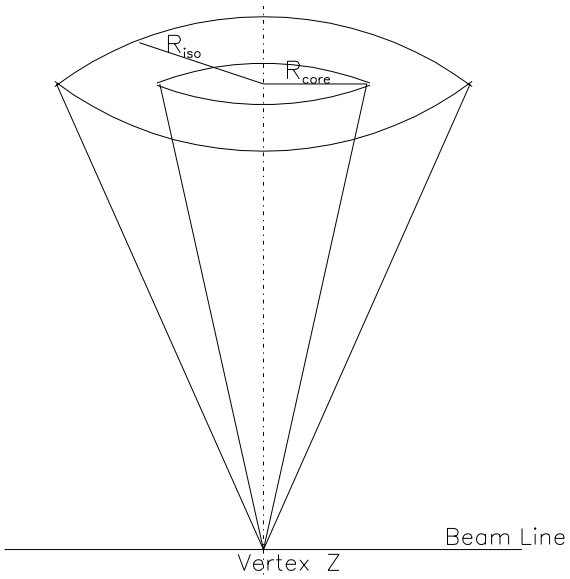

Figure 3.2: Schematic View of a Isolation Cone. The central core cone and the outer isolation cone have the same axis, with ΔR equal to R_{core} and R_{iso} respectively.

very effective in reducing the jet background. DØ defines a photon isolation cone as shown in figure 3.2. A line is made between the event vertex and the shower centroid of a photon, and its orientation is labelled in the (η_γ, ϕ_γ). A core cone is built from the point of the vertex with the span $\Delta R \leq R_{core}$, where ΔR is deifned as

$$\Delta R = \sqrt{(\eta - \eta_\gamma)^2 + (\phi - \phi_\gamma)^2} \tag{3.18}$$

Similarly, an isolation cone is constructed, requiring $\Delta R \leq R_{iso}$. We chose to use the core cone $R_{core} = 0.2$ because it contains most of the shower energy from a photon (or an electron), and two isolation cones with $R_{iso} = 0.4$ and $R_{iso} = 0.7$ for this analysis. The cuts are:

$$E_T^{iso-4} = E_T(coneR = 0.4) - E_T(coreR = 0.2) < 2.0\ GeV$$
$$E_T^{iso-7} = E_T(coneR = 0.7) - E_T(coreR = 0.2) < 7.0\ GeV$$

Fig. 3.1 presents a comparison of the E_T^{iso-4} distributions between clean electrons (a3) and EM jets (b3). The cut $E_T^{iso-4} < 2$ GeV is highly efficient for electrons and photons.

Hits-in-Road Cuts

As described in Section 3.4.1, photons are defined as EM cluster candidates with no tracks in the road. Because the central tracking chambers are not fully efficient ($\approx$ 86% efficient), some electrons fail to have reconstructed tracks in their roads and end up in the photon sample. But since the CDC has a high gas gain and a high hit-finding efficiency ($\approx$ 94%, see Table 2.2), electrons still generate a lot of hits on their trajectory even though the track reconstruction has failed. The plots (a1) and (b1) in Fig. 3.3 are the distributions of the ratio of hit wires over total (RHCDCW) and the number of 3D hits (NHCDC3D) respectively for no-track electrons, where 3D hits indicate the sense wire hits with delay line information). The two cuts, referred as "hits-in-road" cuts later, are defined as:

$$\text{RHCDCW} = \frac{\text{Number of CDC Hit Wires in the Road}}{\text{Tot Number of Wires in the road}}$$
$$\text{NHCDC3D} = \text{Number of CDC 3D Hits in the Road}$$

where the road size is given as $\Delta\theta = 0.05$ and $\Delta\phi = 0.0075$ around the axis from the vertex to the shower centroid (note it is smaller than the road $\Delta\theta \times \Delta\phi \geq 0.1 \times 0.1$ used to identify an EM cluster to be an electron or a

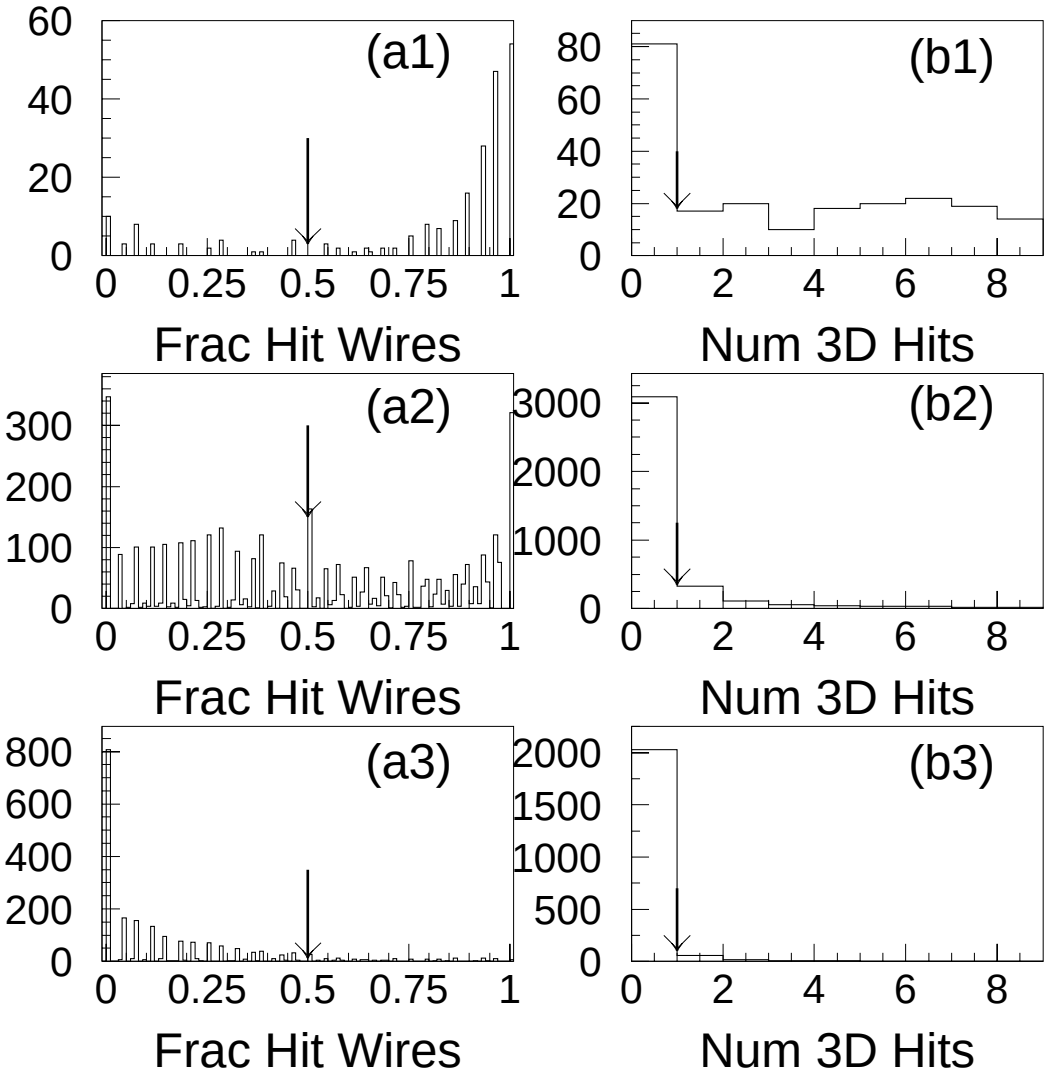

Figure 3.3: Distributions of the fraction of hit CDC sense wires over total wires and found 3D hits in the road. The three samples used include 'photons' from Z $\rightarrow$ 'γ''γ' (a1) and (b1), background 'photons' from an EM jet sample (a2) and (b2), and the emulated 'photons' sample (a3) and (b3).

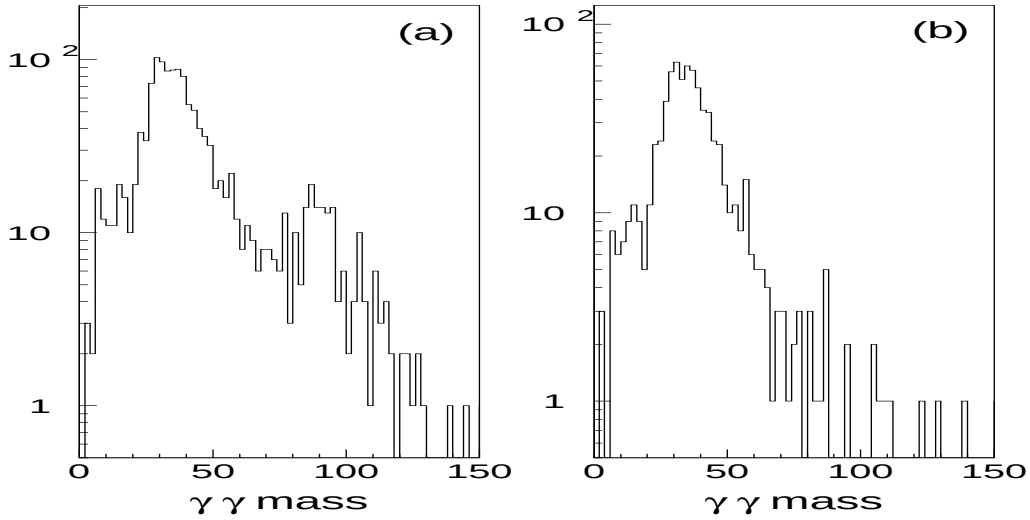

Figure 3.4: Mass Spectra of photon pairs for an inclusive double-photon sample, (a) without and (b) with hits-in-road cuts

photon). In addition to no-track electrons, some jets fragment into a leading energy π^0 and some soft charged or neutral particles. The soft charged particles leave scattered hits along their path due to multiple scattering, and most of the time they do not form charged tracks if they fail the track-fitting χ^2 cuts (for detail, see Section 3.3.1) or if they are kicked out of the tracking road before making it through the whole chamber. Their distributions of RHCDCW and NHCDC3D are shown in the plots (a2) and (b2) of Fig. 3.3. By comparison, the plot (a1) peaks around RHCDCW = 1.0 (like electrons), whereas the plot (a2) is rather flat over the whole range $0.0 <$ RHCDCW < 1.0.

In order to understand the effects of hits-in-road cuts upon true direct photons , an 'emulated' photon sample is constructed based on tightly selected $Z \rightarrow ee$ events. A detailed description of how 'emulated' photons are built can be found later in Section 4.3.2. The 'emulated' photon sample simulates the

distribution of tracks and hits within the road between the vertex and the neutral photon, the sources of which are underlying particles and noisy from CDC sense wires and delay lines. The plots (a3) and (b3) are RHCDCW and NHCDC3D distributions for 'emulated' photons; the (a3) distribution peaks around RHCDCW = 0. The cuts, which are optimized to be efficient for 'emulated' photons and at the same time to have high rejection power over the two types of background, the no-track electrons and the EM jets, are chosen to be:

$$\text{RHCDCW} < 0.5 \qquad \text{NHCDC3D} < 1$$

The efficiency of the cuts will be discussed later in Section 4.3.2. Fig. 3.4 shows the mass distributions of the double-photon sample without (a) and with (b) hits-in-road cuts. The Z resonance peak can be seen in the plot (a) of Fig. 3.4, whereas it is mostly rejected in the plot (b) after applying hits-in-road cuts. The cuts reject more than 80% of no-track electrons.

3.5 Photon and Electron Energy Scale

Since there is no central magnetic field, the calorimeters provide the determination of both energy scale and resolution for photons and electrons. The absolute EM energy scale (for photons and electrons) was initially determined from test beam single electron data, using CC modules.

3.5.1 Calibration at Test Beam Load 2

First, the calibration of the calorimeter electronics is accomplished by using a precision pulser system [89]. By forming the ratio of digitized signal (as ADC counts) and injected charge, one measures the gain G of each readout channel. The live ionization energy, collected by each cell, can be determined as Eqn. (3.1).

To determine the true deposited energy, we can use the conventional definition of the *sampling fraction* as follows:

$$\text{S.F.} \quad = \quad \frac{\text{Average Live Energy in a layer}}{\text{Average Deposited Energy in a layer}} \tag{3.19}$$

Another approach is to minimize the deviation of the summed energy from the true deposited energy [90]. Let us denote the *sampling weights* by w_i (i = 1-5) for EM layers 1-4 and FH layer 1, the overall ADC-to-GeV conversion constant as A and the offset δ_{SF}, the total energy is

$$E = A \sum_{l=1}^{5} \frac{1}{w_l} E_l + \delta_{SF} \tag{3.20}$$

where E_l is the measured ADC counts in the layer l.

To find the best calibration constants (w_i, A and δ_{SF}) in the sense that the set of constants provides good resolution, linearity and uniformity of the electron response in the calorimeter [91], we want to optimize the following χ^2:

$$\chi^2 \quad = \quad \sum_{\eta}^{0.05,0.45,1.05} \sum_{E} \sum_{i}^{N^{E\eta}} \frac{(p_i^{E\eta} - E_i^{E\eta})^2}{\sigma_E^2} \tag{3.21}$$

where $E_i^{E\eta}$ is the reconstructed energy according to eqn. (3.20) for each electron i with energy E and pseudorapidity η, p_i is the beam momemtum measured

EM1 weight, w_1	0.9610
EM2 weight, w_2	0.6260
EM3 weight, w_3	0.7350
EM4 weight, w_4	0.7100
FH1 weight, w_5	1.3520
A (GeV/ADC)	4.0255E-03
δ_{SF} (GeV)	0.347

Table 3.2: Optimized Calibration Constants for the CC Calorimeter

from PWCs (PWC stands for proportional wire chamber), and σ_E is the energy resolution. Fixing w_5 (FH1 weight) at the $\frac{dE}{dx}$ value and letting the rest w_1, w_2, w_3, w_4, A and δ_{SF} float, the optimized set is obtained through minimizing the χ^2 defined by (3.21). Table 3.2 list the optimized set.

3.5.2 Energy Scale Carryover and Corrections

The calorimeter modules were operated in a slightly different setup at the Test Beam from that at DØ. The electronics differ a little regarding the lengths of cables, the times within which the analog signals are sampled and gains are different. The high voltage across the liquid argon gap and the temperature and purity of the liquid argon are also different. Without the beam pipe and the central detectors in front of the calorimeter, the test beam had less upstream material than DØ. Because of the high particle multiplicity at the $p\overline{p}$ collider, DØ adopts a nearest-neighbor clustering algorithm to build electrons and photons, and therefore their energies are measured as the energy sum over all the towers in the cluster, whereas the test beam defined an electron

energy as the energy sum over all readout cells within a fixed window of $\Delta\eta \times \Delta\phi = 0.5 \times 0.5$. In DØ, when an event vertex z is significantly displaced from the nominal position z = 0, the energy reconstructed from towers can differ sizeably from that reconstructed using cells.

An initial indication of the accuracy of the simple calibration carryover was obtained from the measured $Z \rightarrow e^+e^-$ mass peak. It was lower than the combined result from the LEP experiments. Because of the differences listed above, this was not unexpected and *in situ* calibration was carried out to find all the corrections.

The central calorimeter consists of 32 EM modules, and one might expect response variations among the modules since the two modules in the test beam studies show a 1-2% difference in their responses to electrons. A relative calibration, assuming the responses to be uniform along ϕ, were also performed [92]. The resulting weights for CC EM modules are around 0.97 - 1.03, with errors $\leq 0.5\%$.

After all the corrections listed in Table 3.3, the energy is then scaled up to the Z mass from LEP measurements by a constant factor. The uncertainty on the EM energy scale constant is determined by using three calibration data samples $\pi^0 \rightarrow \gamma\gamma$, $J/\psi \rightarrow e^+e^-$ and $Z \rightarrow e^+e^-$ with their well-known masses [66, 92]. Assume the measured energy in the calorimeter and the true energy are related as:

$$E^e_{meas} = \alpha\, E^e_{true} + \delta \tag{3.22}$$

the measured and the true mass values for a resonance can be expressed to

Source of Correction	factor in CC
from test beam	
HV change: 2.5 kV $\rightarrow$ 2.0 kV	+1.5%
PWC Beam Momentum Re-calibration	+0.49%
from in situ	
Calibration Pulser Instability	-0.40%
Liquid Argon Purity and Temperature	+1.0%
Reconstruction Algorithm	+0.30%
Pulser Time Dependence	$\approx$ -0.04%
ϕ Uniformity Weights	$\approx \pm 3\%$
TOTAL CORRECTION	$\approx +7.51\% \pm 0.02\%$

Table 3.3: Corrections applied to the EM energy Calibration carryover from Test beam.

the first order as:

$$M_{meas} = \alpha\, M_{true} + \delta\, f \tag{3.23}$$

where f depends upon the decay topology and is given by $f = 2(E_1+E_2)sin^2(\gamma/2)/M$. Here E_1 and E_2 are the measured energies of the two decay particles, and γ is the opening angle between them. A χ^2 test on each of the three samples results in three independent constraints on α and δ. The combined constraints restrict α and δ(see reference [66]); from it, the scale constant α and the offset δ are determined to be:

$$\alpha = 0.9514 \pm 0.0018(stat)^{+0.0061}_{-0.0017}(syst) \tag{3.24}$$

$$\delta = -0.158 \pm 0.015(stat)^{+0.03}_{-0.21}(syst)\ \ GeV \tag{3.25}$$

Chapter 4

Data Sample and Selection Efficiencies

The candidate data sample was collected during the 1994-1995 run (referred to as run 1B, see Fig. 4.1), corresponding to an integrated luminosity $L = 82.36 \pm 4.40$ pb^{-1}. This chapter will describe the event selection, the trigger, the acceptance and the background subtraction.

4.1 Event Selection

Because of some problems with the hit information of the central tracking chamber CDC in *RECO*, this analysis needs STA-type data(STA refers to standard data, including all the information) which are not available on disk. Only the micro-DST type data(DST refers to data summary type data, including compressed physics data; micro-DST is further compressed from DST) exists on disk. In order to get a data sample with one *RECO* version, a pre_candidate selection is performed on all 1B data. The resulting sample is re-reconstructed using one *RECO* version 12.20. The procedures are as follows:

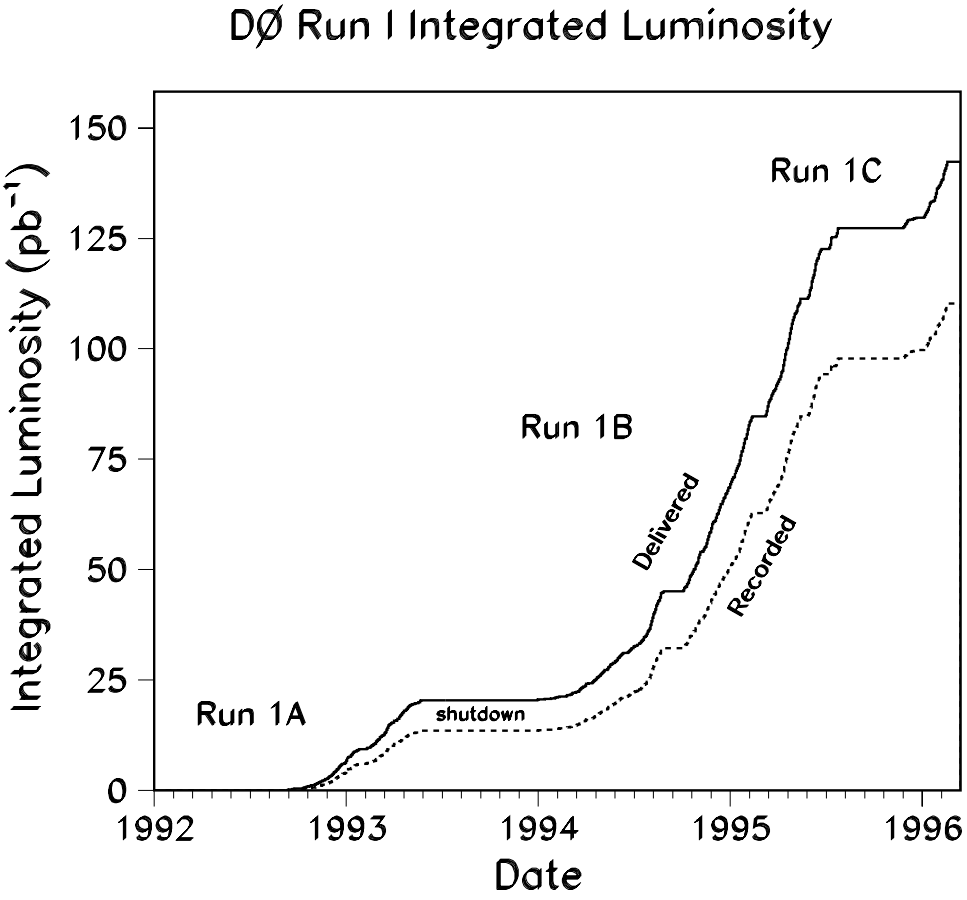

Figure 4.1: Accumulated Luminosity during Run 1

1. Ntuples are created using the information available on the disk-resident micro-DST data. A pre_candidate sample is selected by applying loose cuts:

Number of Photons(PPHO) ≥ 2
Each Photon satisfies the following cuts
Detector $\eta_{det} < 1.1$
$E_T > 10.0$ Gev
Isolation Energy between $R = 0.4$ and $R = 0.2 < 4.0$ Gev
Calorimeter Shower Hmatrix $\chi^2 < 250.$

2. A list is generated with run and event number of all the events which have passed the loose selection cuts. Their STA-type data are picked up by hand. Total number of pre_candidates is **3477**.

3. All the picked events are then re-reconstructed using the *RECO* version 12.20. The output sample is ready for analysis.

4.1.1 Trigger Requirements

Because of the huge EM jet background to photons and the limited rate DØ DAQ (DAQ refers to data acquisition system) can handle (≈ 2 Hz), rather sophisticated algorithms have been developed to trigger on high P_T photons efficiently while keeping the rate manageable.

Hardware Trigger, Level Ø and Level 1

The hardware trigger systems are described in Sections 2.6.1 and 2.6.2. For the double-photon sample, the level Ø scintillator counters are required to detect a $p\overline{p}$ collision. There must be no or very low main ring activity when the data are recorded. Two types of main ring vetoes are available [93]; one, called MRBS_LOSS, vetoes events during the main ring cycle from injection through transition, and the other, called MICRO_BLANK, vetoes the time when the main ring batches pass through the DØ detector in coincidence with a Tevatron bunch crossing. The double-photon trigger was only blanked when both MRBS_LOSS and MICRO_BLANK vetoes were satisfied.

After the level-Ø, the level 1 calorimeter trigger makes a fast sum over all cells within each trigger tower (its size being $\Delta\eta \times \Delta\phi = 0.2 \times 0.2$). The EM energy sum of one trigger tower must be above the threshold $E_T^{thr} = 7.0$ GeV before it becomes a candidate. The number of candidate towers must be ≥ 2. The term for this level 1 configuration is *em_2_med*.

Software Filter Level 2

If an event has fired level 1, it is transferred to a large farm of processors, i.e. Level 2 (see Section 2.6.3). Sophisticated software algorithms are applied to the data in order to select interesting events at the rate ≈ 2 Hz. The selection requirements for double-photon candidates form a level-2 term called *em2_gis_gam*. Its prescription is described as follows:

Hardware Level Ø and Level 1 Trigger	
Level Ø	Level 1
detect one or more $p\overline{p}$ collision MRBS_LOSS.and.MICRO_BLANK	*em_2_med* num EM trigger towers ≥ 2 each trigger tower $E_T^{thr} > 7.0$ GeV
Software Level 2(L2) Filter	
em2_gis_gam num L2 EM clusters ≥ 2 each cluster $E_T^{thr} > 12.0$ GeV	
one L2 EM cluster	the 2nd L2 EM cluster
photon_shape isolation	photon_shape

Table 4.1: Trigger Requirements for the Direct Double-Photon Data Sample

- At level 2, an EM object starts from what has passed the level 1 EM trigger tower. The number of EM objects must be two or more.

- Both EM objects have to have $E_T^{thr} \geq 12\ GeV$.

- An isolation cone is built around each object with the core cone $R = 0.2$ and the isolation cone $R = 0.4$, where $R = \sqrt{\eta^2 + \phi^2}$. At least one object must satisfy the isolation requirement, which is defined as:

$$\frac{E(R=0.4) - E(R=0.2)}{E(R=0.2)} < 15\%$$

- Longitudinal and transverse photon shape cuts are required for both EM objects, where the photon_shape cuts are as follows:

1. The fraction of the energy in the third EM layor(EM3) within 3×3 readout towers is required to satisfy 0.1< EM3 <0.9.

2. The fraction of the energy in the first hadronic layor(FH1) within 3×3 readout towers is required to satisfy FH1 < cut_offset

3. Transverse shower quantities as energy weighted shower radia, SIGMA3 and SIGMA5, are calculated for EM3 cells within 3×3 and 5×5 windows. They are required to satisfy

$$\text{SIGMA5 - SIGMA3} \leq \text{cut\_offset}$$

where the cut_offset is tuned for several energy bins and eta bins.

All the cuts listed above are tuned to be $\geq$ 98% efficient for testbeam electrons. The trigger requirements are summarized in Table 4.1.

4.1.2 Offline Cuts

After events pass the Level 2 filters, they are further selected by offline cuts. Using the nearest-neighbor(NN)algorithm, preliminary photon(PPHO) and electron(PELC) candidates are found (see Section 3.4.1). The number of PPHOs must be $\geq$ 2. Each PPHO is required to satisfy fudicial cuts, kinematic cuts and photon ID cuts, as shown in Table 4.2. The number of candidates found after cuts is **333**.

Offline Selection Cuts for Each PPHO
fudicial cuts
$\lvert\eta_{det}\rvert < 1.0, \quad \lvert\eta\rvert < 1.0$ $\frac{min(\lvert\phi_\gamma - \phi^i_{crack}\rvert, \lvert\phi^{i+1}_{crack} - \phi_\gamma\rvert)^a}{2\pi/32} > 0.05$
kinematic cuts
$E_T^1 > 14.0$ GeV, $E_T^2 > 13.0$ GeV
photon ID cuts   (see Section 3.4.2)
Hmatrix $\chi^2 < 100$ $E_T^{iso-4} < 2.0\ GeV$ .and. $E_T^{iso-7} < 7.0\ GeV$ RHCDCW < 0.5, NHCDC3D < 1

Table 4.2: Offline Selection Requirements for Double-photon sample

[a] ϕ_{crack} refers to the cracks between the calorimeter modules, see Section 4.2.3

4.2 Geometric Acceptance

Theoretical predictions usually assume perfect detectors with no crack and edge losses, whereas the measured results, using a particular apparatus, always have these effects folded in. When one wants to compare experimental measurements to theoretical predictions, these effects have to be corrected in measurements, or in the theoretical calculations, so that one is comparing apples to apples. The measured data are usually corrected for the losses due to the apparatus defects; a quantity, called *Geometric Acceptance* (A), is defined to account for them:

$$\mathcal{A} = \frac{\text{Number of Events Detected by the Detectors}}{\text{Number of Events Incident onto the Detectors}} \qquad (4.1)$$

4.2.1 Event Generator: PYTHIA

To describe the topology of direct double-photon events reasonably well, we chose PYTHIA [94, 95] as the Monte Carlo event generator. The physics processes contributing in PYTHIA are:

$$q\ q \ \rightarrow \ \gamma\gamma \tag{4.2}$$

$$g\ g \ \rightarrow \ \gamma\gamma \tag{4.3}$$

where the cross sections for the processes (4.2) and (4.3) are at the order of $\alpha_{EM}^2\alpha_s^0$ and $\alpha_{EM}^2\alpha_s^2$ respectively. The PDF used is CTEQ2M, both initial and final state radiation are turned on, and the emerging quarks and gluons are allowed to fragment after the hard collision.

Later, we will discuss more a complete NLO QCD calculation [35] and a resummed calculation, RESBOS [28]. As far as the ϕ and η distributions and their correlations are concerned, PYTHIA provides a close description of what the resummed calculation(RESBOS) does. The difference in the acceptance between PYTHIA and RESBOS are $\leq 0.5\%$.

In order to enrich events in the high E_T and central rapidity region, phase space cuts, $E_T < 7.$ GeV and -3 $< \eta <$ 3, are required during event generation. After the events are generated, the z coordinate of the hard collision vertex is smeared with a gaussian of 25 cm width. Two million events were generated accordingly.

4.2.2 Detector Response Simulation

In this analysis we are only concerned with photons, and the detector response of photons can be modeled using testbeam electrons and decay electrons from $W \rightarrow e\nu$ and $Z \rightarrow e^+e^-$.

The energy resolution of the central EM calorimeter (CCEM) is parametrized as [66]:

$$\frac{\sigma_E}{E} = 0.015 \oplus \frac{0.13}{\sqrt{E_T}} \oplus \frac{0.4}{E} \tag{4.4}$$

where the sampling term $0.13/\sqrt{E_T}$ was measured in the Load2 testbeam [91], the constant term $0.015^{+0.006}_{-0.015}$ was determined directly from the observed width of the resonance $Z \rightarrow e^+e^-$, and the noise term $0.4/E$ was extracted from a full simulation including calorimeter uranium and electronic noise and underlying events contribution.

For photons, the centroids of their showers and the collision vertices determine their travel direction. Using a detailed Plate-level Monte Carlo simulation [96], the position resolutions of the shower centroid of single electrons (the same for photons) are measured as [97]:

$$\delta(r\phi) \approx 0.26 \text{ cm}, \quad \delta(z) \approx 0.21 \text{ cm}$$

Since the (x,y) positions of the collision vertices were stable within a few percent of a centimeter during run I, the azimuthal angular resolution is dominated by the resolution of the shower centroid. Taking into account the radius of EM3, 91.6 cm, the resolution $\delta\phi$ is:

$$\delta\phi = 0.003 \; radians \tag{4.5}$$

When comparing the Monte Carlo hit position z_{MC} with the z_{cal} measured by the calorimeter, the resolution $\delta(z_{cal})$ was found to be dependent upon both the z_{cal} position and the polar angle θ_{cal}. It is parametrized as:

$$\delta(z_{cal}) = (p_1 + p_2 \times |\theta_{cal}|) + (p_3 + p_4 \times |\theta_{cal}|) \times |z_{cal}| \qquad (4.6)$$

where the parameters $p_1 = 0.33183\,\mathrm{cm}$, $p_2 = 0.52281 \times 10^{-2}\,\mathrm{cm}/degree$, $p_3 = 0.41968 \times 10^{-3}$, and $p_4 = 0.75496 \times 10^{-4}/degree$.

4.2.3 Geometric Acceptance, $\mathcal{A}$

The Geometric Acceptance($\mathcal{A}$) is defined as Eqn. (4.1). Two main factors contribute to the loss that some events fail to be detected in the central calorimeter (CC). One is the cracks between CC EM modules. There are 32 EM modules arranged in a ϕ ring in total; the crack regions between neighboring modules are non-instrumented and are cut out by requiring the ϕ distance between the photon hit and the nearby cracks to be more than 5% of the module size. For the double-photon data sample, the ϕ distribution of each photon is uniform, and, assuming the two photons are loosely correlated in ϕ, the fraction of events surviving after the ϕ crack cuts $\approx (90\%)^2 \approx 80\%$.

The other factor is the vertex smearing. The CC calorimeter physics η spans between -1.2 and 1.2 from the nominal vertex position $z_{vert} = 0.0$. When the collision vertex z moves around the nominal position $z = 0.0$, the CC effective η span changes so that some photons travel out of the CC coverage and cannot be detected. This results in losing $\approx 15\%$ of double-photon events.

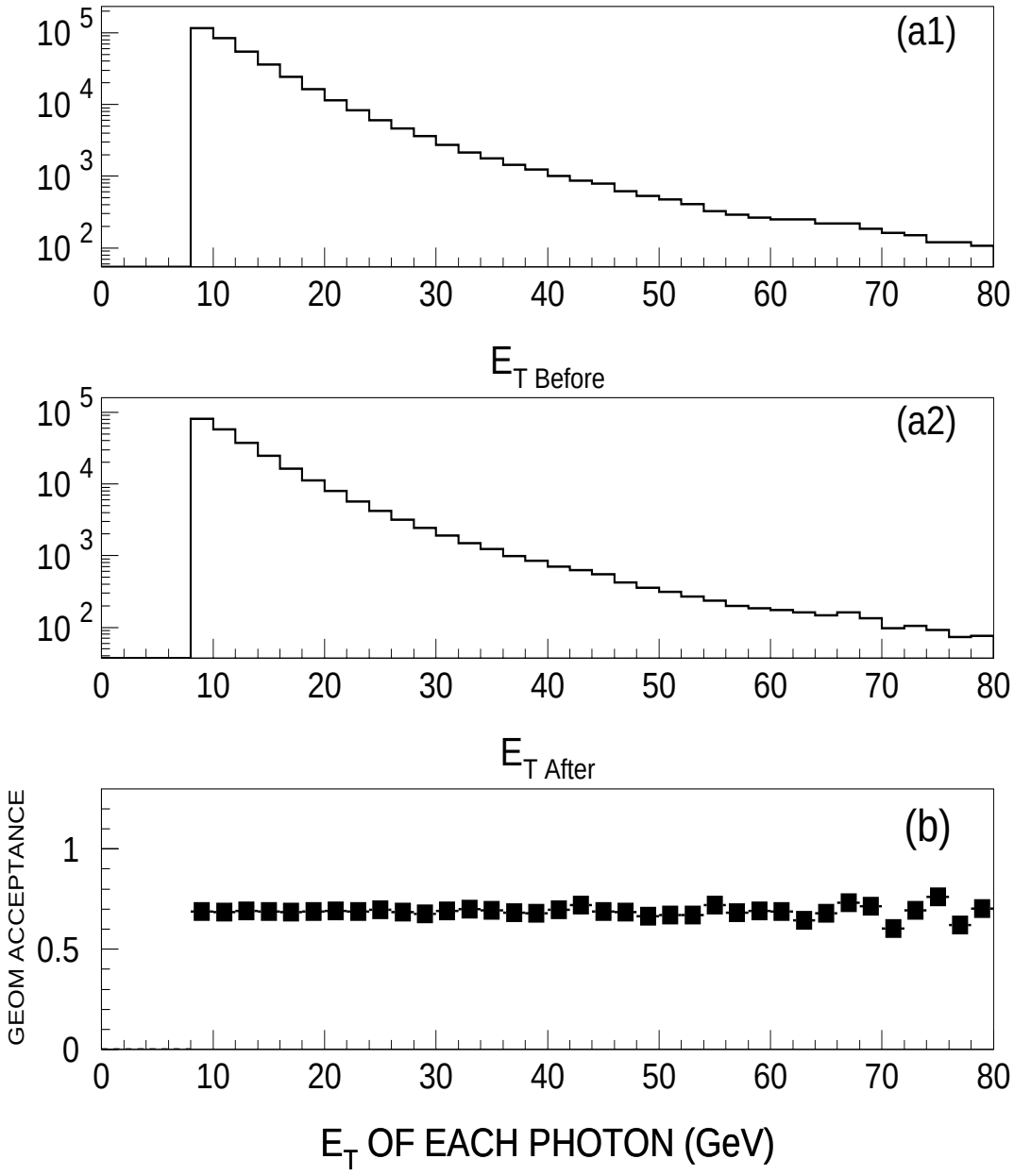

Figure 4.2: Illustration of the determination of the Geometric Acceptance. The distributions of E_T of each photon before (a1) and after (a2) cuts. The ratio of plot (a2) over plot (a1) bin-by-bin is what is shown in plot (b), which is the differential Geometric Acceptance vs.E_T.

	Geometric Acceptance
E_T^γ	0.687 ± 0.001
$P_T^{\gamma\gamma}$	0.688 ± 0.002
$M^{\gamma\gamma}$	0.672 ± 0.003
$\Delta\phi^{\gamma\gamma}$	0.688 ± 0.003

Table 4.3: Geometric Acceptance vs.various kinematic quantities

Combining the two factors, the geometric acceptance of double-photon events is:

$$\mathcal{A} \approx 80\% \times (1 - 15\%) \approx 68\%$$

For a precise determination, 2 million Monte Carlo events are used, which are generated as described in Section 4.2.1 and fast smeared using the resolution parameters given in Section 4.2.2. The acceptance value in each bin of a variable of interest is calculated as:

$$\mathcal{A}/bin = \frac{\text{Events/bin when } |\eta^{\gamma 1,\gamma 2}| < 1.0, |\eta_{\text{det}}^{\gamma 1,\gamma 2}| < 1.0, \phi_{\text{crack}}^{\gamma 1,\gamma 2} \text{ cut}}{\text{Events/bin when } |\eta^{\gamma 1,\gamma 2}| < 1.0} \quad (4.7)$$

Fig. 4.3 shows the dependence of the Geometric Acceptance ($\mathcal{A}$) upon E_T^γ, $P_T^{\gamma\gamma}$, $M^{\gamma\gamma}$ and $\Delta\phi^{\gamma\gamma}$. They are found to be essentially independent of each variable.(see Table 4.3)

4.3 Efficiencies

Before getting into the final candidate sample, all the events are required to pass the selections including the trigger and the offline cuts. To measure the

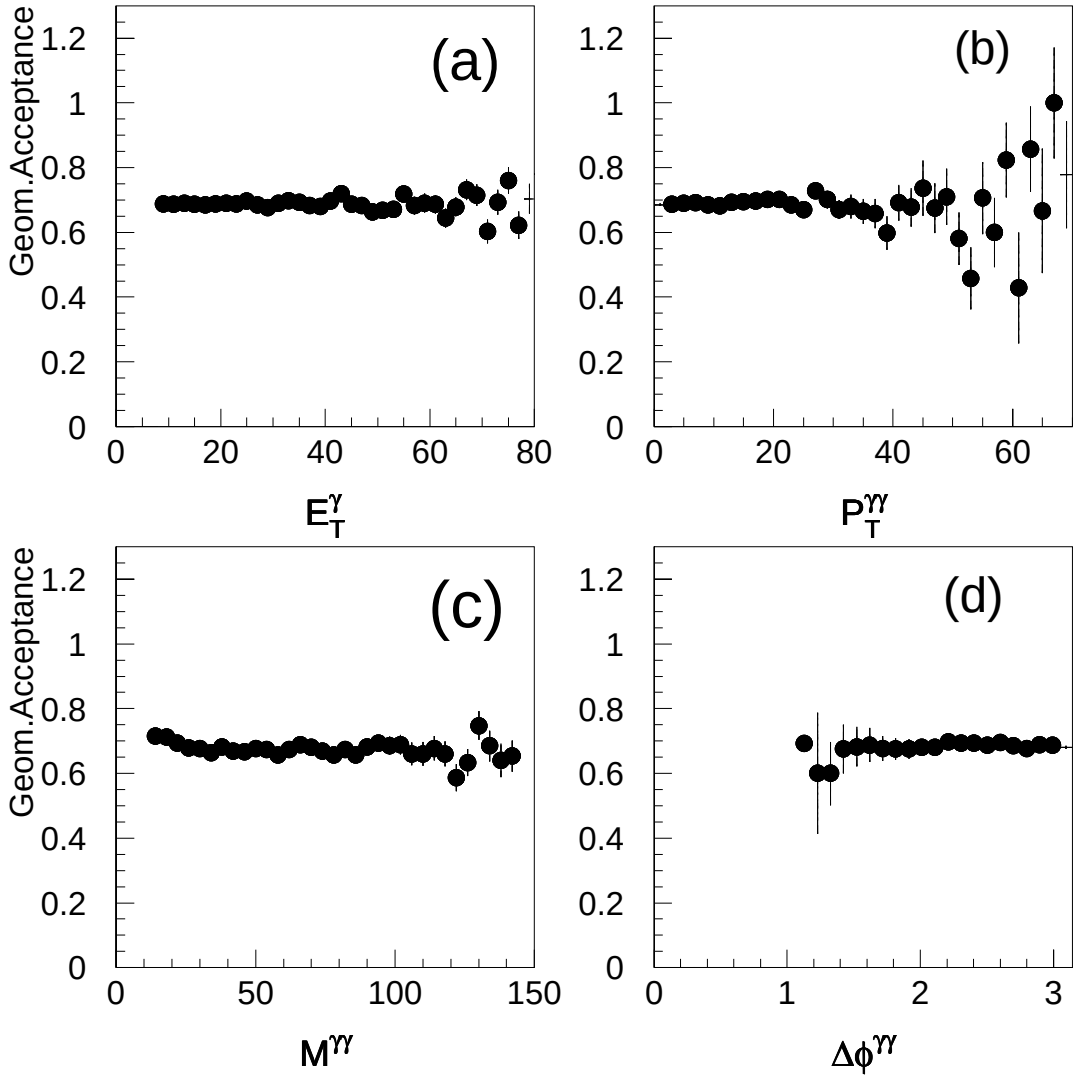

Figure 4.3: Differential Geometric Acceptance vs. (a)E_T^γ of each photon, (b)$P_T^{\gamma\gamma} = |\vec{E_T^{\gamma 1}} + \vec{E_T^{\gamma 2}}|$ of the double-photon system, (c)$M^{\gamma\gamma}$ of the photon pair, and (d)$\Delta\phi = |\phi^{\gamma 1} - \phi^{\gamma 2}|$ of the photon pair. They are nearly constant in all cases.

production cross section, one must understand the efficiencies of each selection step.

4.3.1 Trigger Efficiencies

Level Ø Efficiency

The Level Ø requirement for double-photon events is that the level Ø counters must detect $p\overline{p}$ collisions and yield a fast-z information (see Table 4.1). To study its efficiency, a sample of W $\rightarrow e\nu$ was chosen by requiring one Level-2 filter *EM1_EISTRKCC_MS* having fired; this does not require Level-Ø confirmation(for trigger version 10.0 and later) [56]. Measuring the fraction of events which have fast-z information, the Level-Ø efficiency for requiring fast-z is (see [56])

$$\epsilon_{L\emptyset} = 0.98 \pm 0.01 \tag{4.8}$$

Double-photon Trigger Efficiency

The double-photon candidate sample requires that both the Level-1 trigger *em_2_med* and the Level-2 filter *em2_gis_gam* are satisfied (see Table 4.1 for descriptions). To measure the overall trigger efficiency, we use one "unbiased" electron from $Z \rightarrow ee$ decays as a diagnostic sample and send these electrons through the trigger simulation.

The diagnostic sample is collected by selecting an inclusive $Z \rightarrow e^+e^-$ sample as follows:

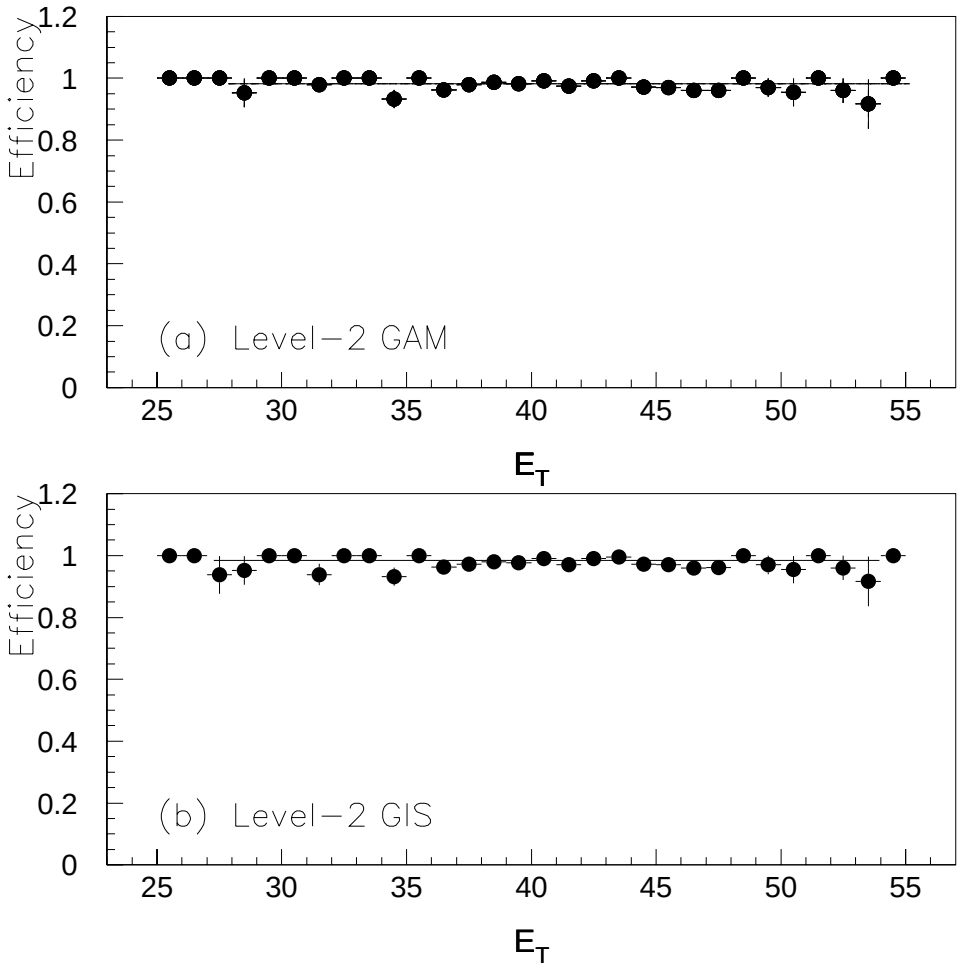

Figure 4.4: Trigger Efficiency Plots (a) and (b) for Level-2 *GAM* and *GIS* configurations. The E_T range shown is far above the threshold of 12 GeV.

- Requiring at least two high E_T electrons or one electron and one photon both having $E_T > 20$ GeV.

- Requiring both EM objects to be in the central region, $|\eta^{1,2}| < 1.0$, $|\eta^{1,2}_{det}| < 1.0$, and being away from ϕ cracks.

- Requiring both EM objects to satisfy electron or photon ID cuts:

$$\chi^2_1 < 100, \quad \chi^2_2 < 100.$$
$$\text{isol\_frac}_1 < 15\%, \ \text{isol\_frac}_2 < 20\%$$

  Their pair mass must be in the resonance window $75 < M_{ee} < 95$ GeV.

- Requiring the Level-2 filter *em2_eis_esc* to have been fired.

A trigger simulation is setup with some special Level-2 filters: *EIS, ELE, ESC, GIS, GAM, ISO*, where *EIS* means electron_shape and isolation, *ELE* means electron_shape only, *ESC* means no shape and isolation cuts, *GIS* means photon_shape and isolation, *GAM* means photon_shape only, and *ISO* means isolation only.

The diagnostic sample has passed the level-2 requirement, *em2_eis_esc*. If both EM objects have passed the Level-2 *EIS* requirement, either of them may have passed the Level-2 *ESC* requirement. They are considered unbiased and both of them get into the "unbiased" electron sample. If one object satisfied the Level-2 *EIS* requirements and the other failed, the failed one must have passed through the *ESC* and therefore gets into the "unbiased" electron sample. The "unbiased" electron is hence put through the trigger

simulation, and the resulting trigger efficiencies for the Level-2 terms *GIS* and *GAM* are measured as:

$$\epsilon_{\rm trig} = \frac{\text{Num of Electrons passed the trigger in the "unbiased" sample}}{\text{Num of all Electrons in the "unbiased" sample}} \tag{4.9}$$

Fig. 4.4 shows the trigger efficiencies for *GIS* and *GAM* respectively. The efficiencies are constant over the E_T range $26 < E_T < 55$; the fitted values are

$$\epsilon_{\rm trig}^{GIS} = 0.983 \pm 0.003, \qquad \epsilon_{\rm trig}^{GAM} = 0.987 \pm 0.003$$

Because of the kinematics of $Z \rightarrow e^+e^-$ decays, the E_T of the electrons populate the range between 25 and 55 GeV. For the double-photon data sample, photons have E_T down to 13 GeV. To understand the low E_T ($13 < E_T < 30$) trigger behavior, data from special GAMMA runs with a lower threshold of $E_T^{thres} = 6\ GeV$ were used for efficiency studies. The special run trigger requires the *GAM* in Level-2 term, and the threshold (6 GeV) effect in the data is negligible for $E_T > 12$ GeV (the effects on the efficiencies are $< 0.5\%$). The set of data is run through the same trigger simulation as above; the measured efficiencies $\epsilon_{\rm spec}^{GIS}, \epsilon_{\rm spec}^{GAM}$ are corrected by the efficiency $\epsilon_{\rm GAM} = 0.987$ of the *GAM* requirement in the data set. The trigger efficiency is therefore determined in each E_T bin as:

$$\epsilon_{\rm trig}^{GIS} = \epsilon_{\rm spec}^{GIS} \times 0.987$$
$$\epsilon_{\rm trig}^{GAM} = \epsilon_{\rm spec}^{GAM} \times 0.987$$

Fig. 4.5 shows the combined trigger turn-on curves for *GAM* and *GIS*, with the threshold $E_T^{thr} = 12$ GeV for a range of $12 < E_T < 60$. The curves can be

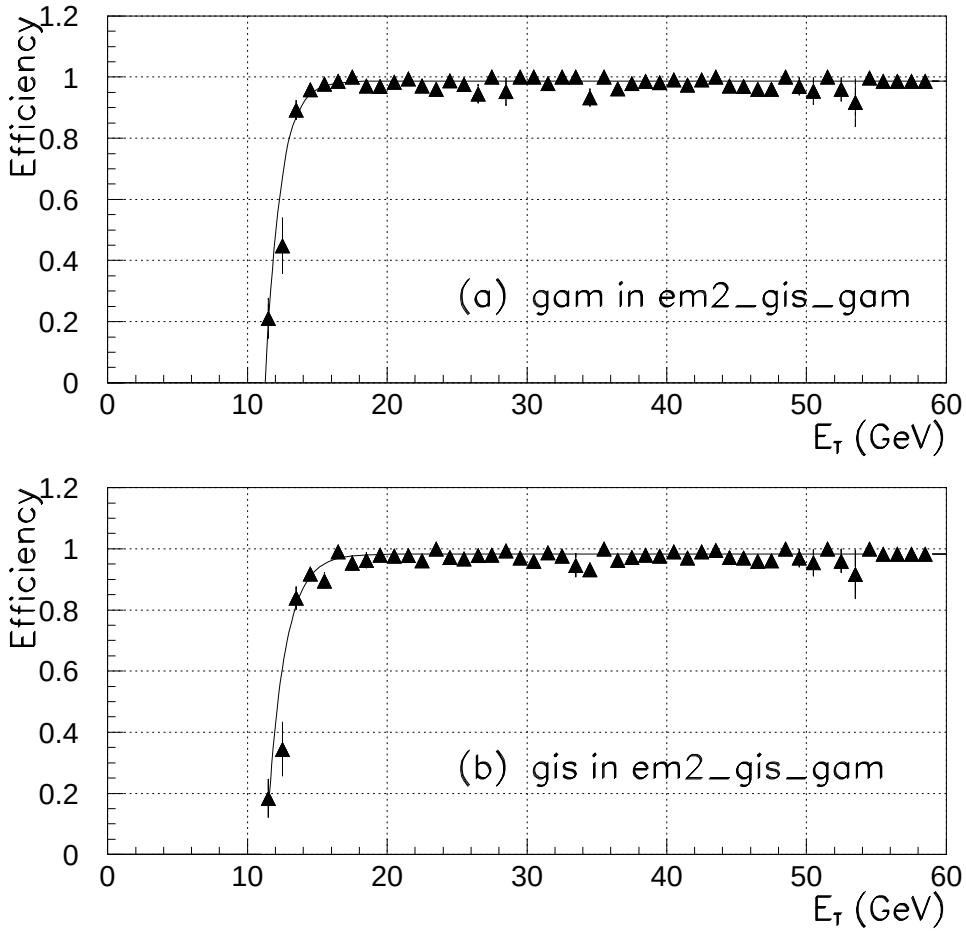

Figure 4.5: The trigger efficiency curves for (a) *GAM* and (b) *GIS* with a threshold of $E_T^{thr} = 12$ GeV.

fitted as the following functions:

$$\epsilon_{\rm trig}^{GIS}(E_T) \;=\; 0.9831 \times (1.0 - e^{9.178 - 0.812 E_T}) \tag{4.10}$$

$$\epsilon_{\rm trig}^{GAM}(E_T) \;=\; 0.9874 \times (1.0 - e^{10.890 - 0.965 E_T}) \tag{4.11}$$

4.3.2 Emulated Photons

After events pass the trigger requirements, they are run through the *RECO* program and preliminary photon candidates are filled into the ZEBRA [78] bank PPHO. These PPHOs are further selected using fudicial cuts and photon ID cuts (Table 4.2 gives a complete list of the cuts). The offline selection efficiency $\epsilon_{\rm offl}$ includes all the steps starting from *RECO*.

Before embarking on efficiencies, it is useful to introduce the "emulated photon" sample. The idea is that if we choose an average area of the calorimeter, away from jets and real objects, build an emulated photon and construct a road associated with it. We can learn a lot about the tracking chamber response from underlying particles and noise by looking at the hits and tracks within the road of the emulated photon. The procedures are as follows:

- Selecting a tight $Z \rightarrow e^+e^-$ sample similar to the diagnostic sample in Section 4.3:

  1. Both PELCs, $E_T^1 > 20, \quad E_T^2 > 20$ GeV.
  2. $|\eta^1| < 1.0$ or $|\eta^1| > 1.5, \quad |\eta^2| < 1.0$ or $|\eta^2| > 1.5$.
  3. $\chi_1^2 < 100, \quad \chi_2^2 < 100$.
  4. Isol_frac$_1 < 15\%, \quad$ Isol_frac$_2 < 15\%$.
  5. $70 < M_{ee} < 100$ GeV for pair mass.

- Determining the bisector of two electrons as $\eta = \frac{1}{2}(\eta_1 + \eta_2)$, $\phi = \frac{1}{2}(\phi_1 + \phi_2)$. Using the bisector as the shower centroid of an emulated photon, we build a core cone (R=0.2) and a isolation cone (R=0.4) and fill their E

and E_T by summing over all towers. A tracking road is also constructed between the centroid and the vertex, and hits and tracks are found within the road.

The constructed emulated photon sample will be used for several studies later.

4.3.3 Offline Efficiencies

Section 3.4.1 describes how *RECO* programs find preliminary photon candidates (PPHOs). Since double photons have a high E_T (> 12 GeV) and are usually isolated, they can always be found by the DØ nearest-neighbor algorithm and satisfy the E_T cut of 1.5 GeV. The EM fraction cut($> 90\%$) is not so easy to verify in efficiency. At the test beam load2, single electron beams were used to test the CC calorimeter. Using the same algorithm as in DØ, the EM fraction cut (defined as $\mathrm{EM_{frac}} < 90\%$) is 100% efficient up to 75 GeV and is $\approx 1\%$ inefficient for 100 GeV electrons. Before applying the results at DØ, one has to consider the differences between the test beam and DØ. The sampling fraction at the test beam is different from that used for the run 1B data, the test beam has less upstream material than DØ does, and the test beam electrons only come from vertex z=0 while the event vertex at DØ has a wide gaussian distribution with RMS = 25 cm. Taking into account these differences, the EM fraction cut at DØ remains $> 99\%$ efficient for photons up to $E_T = 75$ GeV, based on Monte Carlo simulation.

A further cut, which requires the fraction of the energy of the highest-energy tower over the whole cluster energy must be $> 40\%$, is studied using

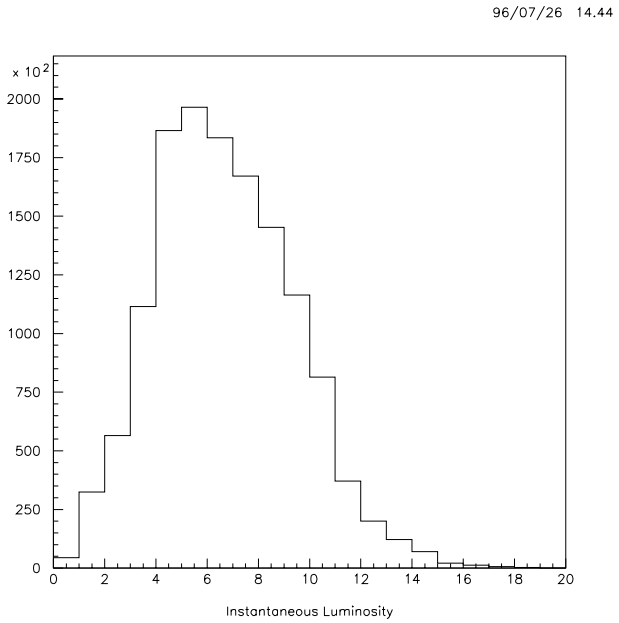

Figure 4.6: The instantaneous luminosity L spectrum for run 1B, in the unit of $10^{30} cm^{-2} s^{-1}$.

both the test beam and the Plate level Monte Carlo electrons (their vertex being smeared as a gaussian of RMS = 25 cm). No events fail the cut.

No Tracks in the Road

The preliminary EM objects are considered as PPHOs or PELCs, depending on whether any tracks can be found in the road between the EM objects and the vertex. What is the efficiency for true photons to satisfy the no-track requirement? Two effects will make true photons fail, listed below:

- True photons may convert when they pass through the material before the central drift chamber (CDC). The amount of upstream material is $\approx 0.1 X_0$ (X_0 being *radiation length*) in the central region, including the beryllium beam pipe, the VTX chamber and the TRD. The conversion

probability (p_{conv}) is expected to be ≈ 0.1 for a photon to convert into e^+e^- pair before it reaches the CDC. A Monte Carlo single photon sample was generated and run through the DØ detector simulation. It confirmed that the fraction of converted photons $\approx$ 10%, i.e. the efficiency for photons not to convert is

$$\epsilon_{\text{dont\_convert}} \approx 0.90 \tag{4.12}$$

- Even if a true photon has not converted, some charged tracks from underlying particles may happen to fall in the tracking road of the photon. This loss is measured using the emulated photon sample, with an additional requirement that the E_T in the isolation cone (R=0.4 - R=0.2) $<$ 2 GeV. This isolation cut makes sure that the emulated photons have the same environment as the true photons. The efficiency for the emulated photons not to have tracks in the road is

$$\epsilon_{\text{no\_underlying\_tracks}} = 0.917 \pm 0.001 \tag{4.13}$$

The two efficiencies are uncorrelated, and the overall efficiency for true photons not to have tracks in their road is

$$\begin{aligned} \epsilon_{\text{no\_tracks}} &= \epsilon_{\text{dont\_convert}} \times \epsilon_{\text{no\_underlying\_tracks}} \\ &\approx 0.82 \pm 0.01 \end{aligned} \tag{4.14}$$

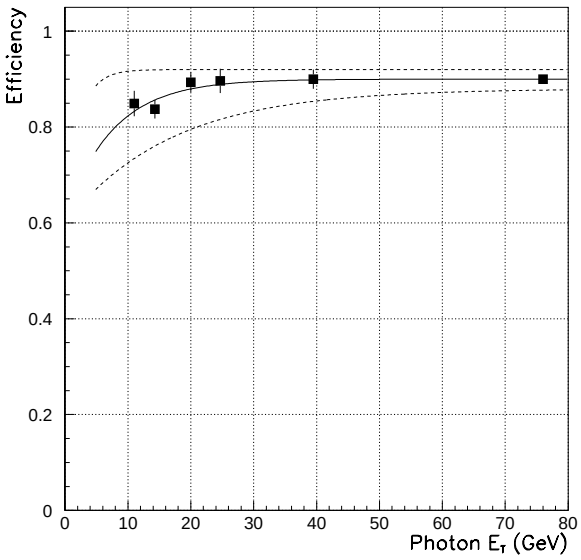

Figure 4.7: Efficiency Curve of the cuts $\chi^2 < 100$, $E_T^{iso-4} < 2.0$ GeV for photons. The dashed lines show the range of uncertainty.

Calorimeter χ^2 and Isolation Cuts

Further tight photon ID cuts are applied to the data sample(see Section 3.4.2). To understand the efficiencies of χ^2 and E_T^{isol} cuts, we generated a single photon Monte Carlo sample and put it through Plate level Geant simulation [96]. The photons are then overlaid with four sets of minibias events which were collected at four different instantaneous luminosities, covering the range in the fig. 4.6). Here the minibias events indicate the events that are collected when the level-Ø detects hard collisions. The minibias events include the contributions from both underlying particles and electronics and uranium noise. Due to strong correlation, the shape of the combined efficiency of the two cuts,

$$\chi^2 < 100, \quad E_T^{iso-4} < 2.0 \text{ GeV} ,$$

is measured using the single photon MC sample. The normalization is determined by using a clean $Z \rightarrow e^+e^-$ sample. Four different curves were obtained corresponding to the four instantaneous luminosities, and they are weighted according to the Figure 4.6. The resulting efficiency curve as a function of E_T^γ is shown in Fig. 4.7.

An additional isolation cut $E_T^{iso-7} < 7.0$ GeV is applied to the data to reduce the jet background. This is a cut more on the environment around the photon rather than the photon itself. The efficiency is therefore measured by studying the E_T flow of underlying particles. The emulated photon sample (see Section 4.3.2) describes a region away from any high E_T objects, and so the E_T distributions in the core cone R=0.2, the isolation cones R=(0.4 - 0.2) and R=(0.7 - 0.2) provide a spectrum for the E_T flow from underlying particles (see Fig. 4.8).

The EM showers from electrons and photons are very narrow transversely, with nearly all the energy being contained in the core cone R=0.2. Fig. 4.9 shows the E_T leakage for 15, 20, 25 GeV testbeam electrons. Even with underlying particles, the isolation cut $E_T^{iso-4} < 2$ GeV is $> 90\%$ efficient. Using the distributions in Fig. 4.8, we measured the ratio of events satisfying both $E_T^{iso-4} < 2.0$ and $E_T^{iso-7} < 7.0$ GeV over those satisfying $E_T^{iso-4} < 2.0$ GeV. The resulting efficiency value is:

$$\epsilon_{\rm isol7} \quad = \quad 0.967 \pm 0.010 \tag{4.15}$$

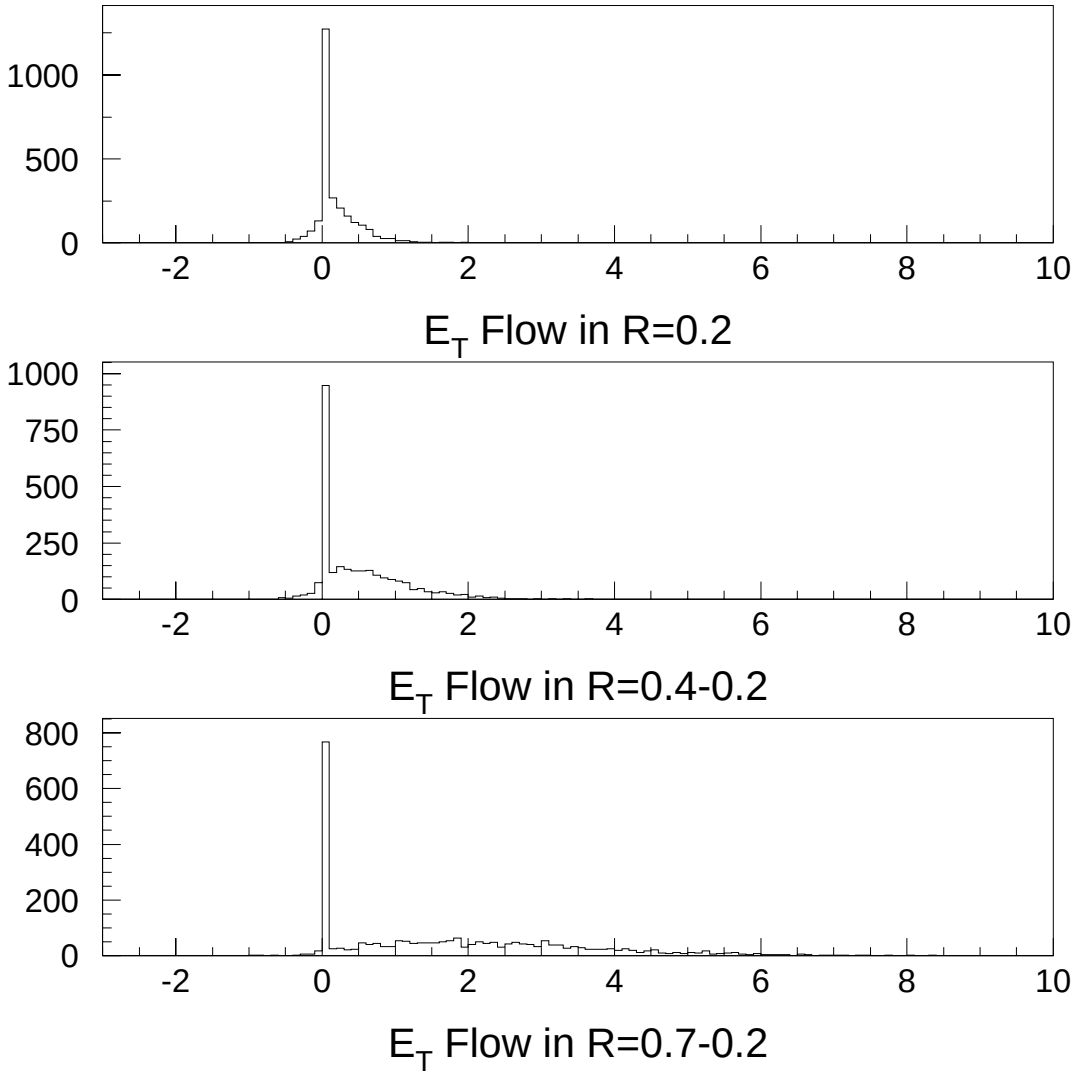

Figure 4.8: E_T flow spectrum of the underlying particles in $Z \rightarrow e^+e^-$ events, with the core cone R=0.2, the isolation cones (R=0.4 - R=0.2) and (R=0.7 - R=0.2)

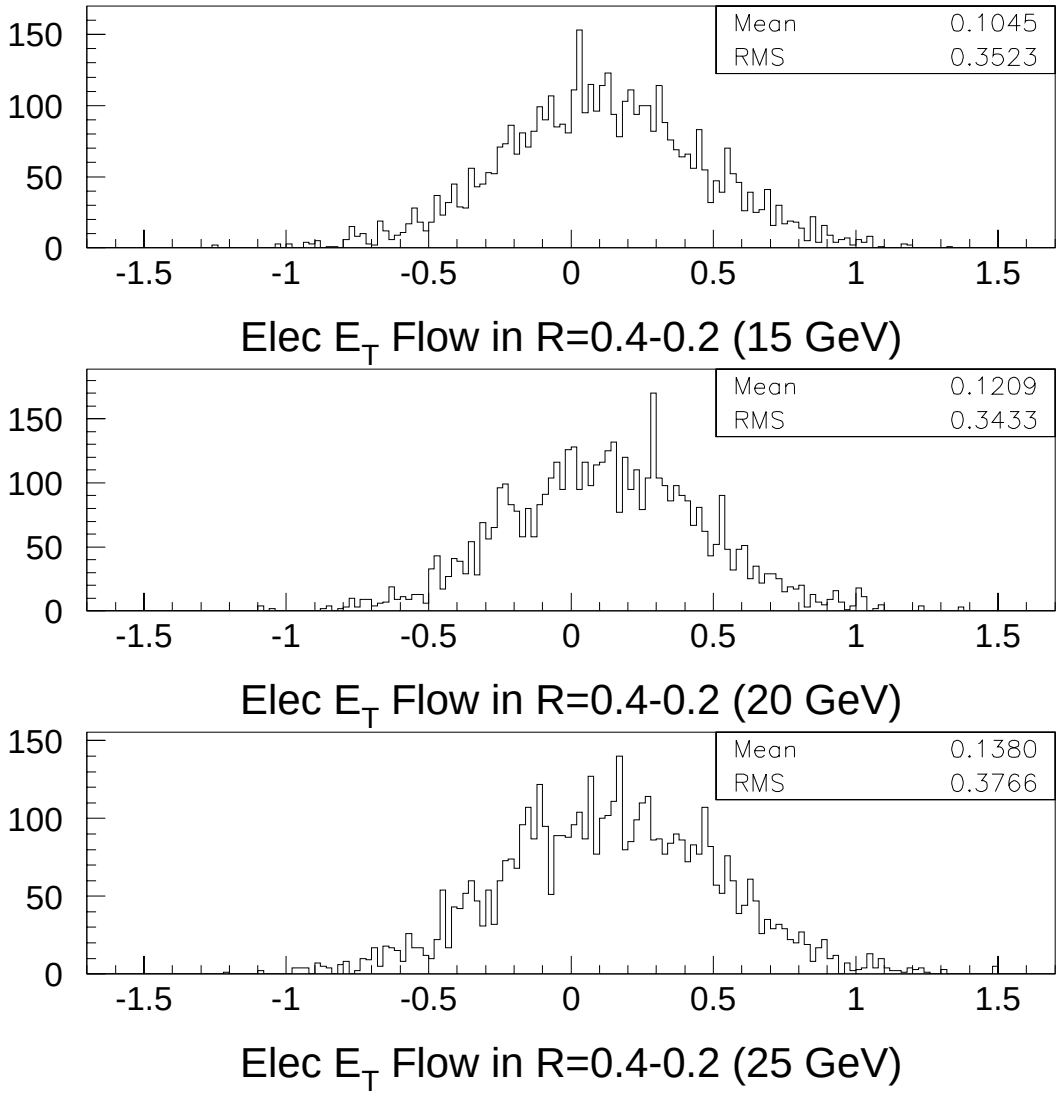

Figure 4.9: E_T flow spectrum in the isolation cone (R=0.4 - R=0.2) for test-beam electrons with energies E = 15, 20, 25 GeV. Very small fractions of energy leak out of the core cone, and this leakage is nearly energy independent.

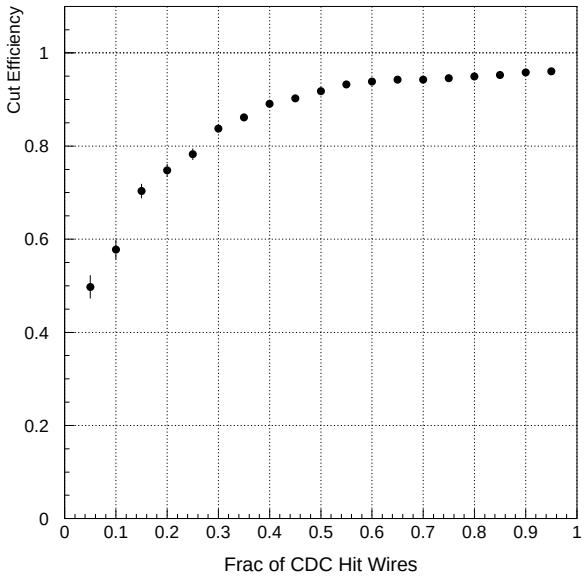

Figure 4.10: Efficiency versus the cut of the fraction of CDC hit wires when the number of 3D hits is required to be 0.

Hits_in_road Cuts

The efficiency of the Hits_in_Road cuts (see Section 3.4.2 for definition) is determined using the emulated photon sample (Section 4.3.2). Requiring NHCDC3D < 1 and varying the RHCDCW cut for the no-track emulated photons, the efficiency curve is shown in Fig. 4.10. The chosen cut is **RHCDCW** $<$ **0.5**, and its efficiency is

$$\epsilon_{\text{hits\_in\_road}} = 0.918 \pm 0.007 \tag{4.16}$$

Tracking Efficiency in CDC

Before applying the hits_in_road cuts, some electrons from Z decay enter the double-photon sample, as shown in Fig. 3.4. To estimate the contamination

from Z $\rightarrow$ ee, we will measure the tracking efficiency in the CDC and the rejection factor of the hits_in_road cuts for electrons when tracks are not found in the road.

A sample of PELC+PELC and PELC+PPHO from Z's is selected for the tracking efficiency study. For each PELC or PPHO, the requirements are

- the level_1 em_2_med and level_2 ele_2_high are fired
- $|\eta| < 1.1$, ϕ_crack_cut, $E_T > 20.$ GeV
- $\chi^2 < 100$, isol_frac $< 15\%$

The sample is further divided into one with only one vertex and the other with any number of vertices. The Z invariant mass spectrum is modelled using a relativistic Breit-Wigner shape with an exponential factor which accounts for the uncertainty of the Z production cross section [92], being further convoluted with a gaussian response function derived from the detector resolution on an event by event basis. A likelihood function $\mathcal{L}$ is constructed for each measurement of the mass m_i and its resolution σ_i:

$$\mathcal{L}(m_i, \sigma_i; M_Z, \Gamma_Z) = \int dm \left(\frac{e^{-\beta m} m^2}{(m^2 - M_Z^2)^2 + \frac{m^4 \Gamma^2}{M_Z^2}} + A e^{-Bm}\right) \frac{1}{\sqrt{2\pi}\sigma_i} e^{-\frac{(m-m_i)^2}{2\sigma_i^2}} \tag{4.17}$$

where M_Z and Γ_Z are the input mass and width of Z from LEP results, A and B are parameters to fit the background, and m is the best fitted mass of Z.

By maximizing $\ln(\mathcal{L})$, A and B can be determined and so the amount of background is measured for both PELC+PELC and PELC+PPHO. Let us call T to be the CDC tracking efficiency, and N_{ee} and $N_{e\gamma}$ to be the number

	one vertex	any number vertices
tracking efficiency in CDC	$(91.4 \pm 2.1)\%$	$(89.8 \pm 1.9)\%$

Table 4.4: Single electron tracking efficiency in CDC

of true ee pairs and true $e\gamma$ pairs within the mass window $80 < M < 95$ GeV. After subtracting the backgrounds, the relation holds as:

$$\frac{N_{ee}}{N_{e\gamma}} = \frac{T \times T}{2 \times T \times (1 - T)} \tag{4.18}$$

The tracking efficiencies in the CDC are measured for the two samples respectively, one with only one event vertex and the other having any number of vertices. The results are summarized in Table 4.4.

Z electrons in the double-photon sample

When an electron fails to have tracks reconstructed in its road, it can be effectively rejected by applying hits_in_road cuts. Using the above sample with both PELC+PELC and PELC+PPHO from Z, the rejection factor is measured as $\mathbf{F_{reject} = 6.6 \pm 5.0}$, namely as the total number of PPHOs over the number of the PPHOs passing the hits_in_road cuts.

Taking the measured $Z \to e^+e^-$ cross section $\sigma_Z B(Z \to e^+e^-) = 0.218$ nb [98], the estimated number of Z events in the double-photon sample is:

$$\begin{aligned} N_{\mathrm{Z-backgr}} &= L \times \sigma_Z B(Z \to e^+e^-) \times A_Z \times \epsilon_Z \times (1 - T)^2 \\ &\approx 82.36 \times 218. \times 0.36 \times 0.9 \times (1 - 0.9)^2 \\ N_{\mathrm{Z-backgr}} &\approx 58 \end{aligned} \tag{4.19}$$

Looking at the mass plot of the photon pair in Fig. 3.4 and assuming a linear background around the Z resonance on a log scale, the background is estimated as $\approx 51 \pm 8$. It is consistent with the estimation in eqn. 4.19. After the hits_in_road cuts, the number of Z remaining in the photon sample is approximately 8 ± 6.

Overall Efficiency

Taking into account of all the cuts which select our photon candidates, the overall efficiency is equal to:

$$\begin{aligned} \epsilon_{\text{offline}} &= \epsilon_{\text{no\_tracks}} \\ &\times \epsilon_{\text{hits\_in\_road}} \\ &\times \epsilon_{\chi^2\text{\_and\_isol4}} \\ &\times \epsilon_{\text{isol7}} \end{aligned} \tag{4.20}$$

4.4 Background Subtraction

The background to direct photons consists of some jets fragmenting into one leading energy π^0, or η, or ω and some soft particles around it. Using the calorimeter shower profile, the two photons from high energy π^0 (or η, or ω) travel nearly collinearly (with a very small opening angle) and so they are not distinguishable from directly produced photons on an event-by-event basis. But looking at the longitudinal energy deposition, especially the energy deposited in the first EM layer(EM1), the nearly-collinear two photons

are likely to deposit more energy than a single photon. We can model the distribution of -ln(EM1/ETOT) for true photons and fakes(fakes refer to the EM jets which are indistinguishable from the photons). Their distributions are shown in Fig. 4.11. The data are composed of both true and fake photons, and each fraction can be determined by fitting the distribution of -ln(EM1/ETOT) in the data as a sum of that of true and fake photons.

4.4.1 Discriminant Distributions of True and Fake Photon Samples

To model the discriminant -ln(EM1/ETOT) of photons, a large Monte Carlo sample of single photons is generated and run through plate level detector simulation. It is further smeared by electronic and uranium noise. The plots (a1) and (b1) in Fig. 4.11 show the EM1 fraction and -ln(EM1/ETOT) distributions for photons.

For the fake photon sample, a large jet Monte Carlo sample is generated by using PYTHIA. It is filtered through several steps as below [99]:

- qq, qg, or gg are allowed to collide, and the emerging partons after the hard collision are allowed to fragment and hadronize.
- A seed list ordered in E_T is made by looping through all π^0, η, and γ with $E_T > 5$ GeV.
- The number of total charged tracks, N_{trk}, is counted in the core cone R=0.2 around each seed.

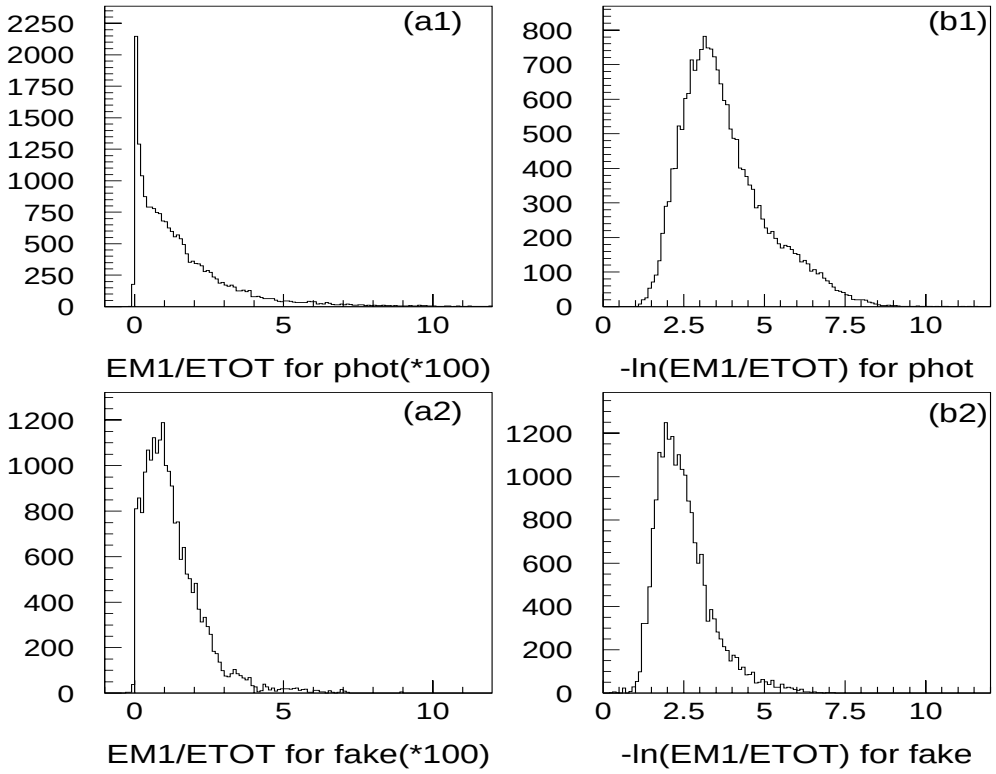

Figure 4.11: Plots (a1) and (a2) show the distributions of the fraction of EM1 over total energy for Monte Carlo photon and fake, and plots (b1) and (b2) describe the distributions of -ln(EM1/ETOT) correspondingly.

- An isolation cone between R=0.4 and R=0.2 is built around each seed particle, within which the E_T sum and E_T^{iso} of all particles are calculated.
- One seed becomes a candidate only when:

$$N_{trk} = 0, \quad E_T^{iso} < 2 \text{ GeV}, \quad \frac{E_T(\text{R=0.2})}{E_T(\text{parent parton})} > 0.6$$

- All candidate seeds are run through the detector simulation and then are superimposed with zero-bias events (including electronic and uranian noise)
- The final fake photon sample is further selected using the same photon ID cuts as the data.

The distributions of the EM1 fraction and -ln(EM1/ETOT) of the fake photons are shown in the plots (a2) and (b2) in 4.11.

The modeling of the (EM1/ETOT) distribution for Z electrons was done as well, and was compared with Z electron data. As shown in Fig. 4.12, the Monte Carlo reproduces the data reasonably well.

4.4.2 Constructing Discriminant Distributions for Double Photons

The double-photon events are assumed to be made up of three possible sources: photon-photon, photon-fake, and fake-fake. We construct the product,

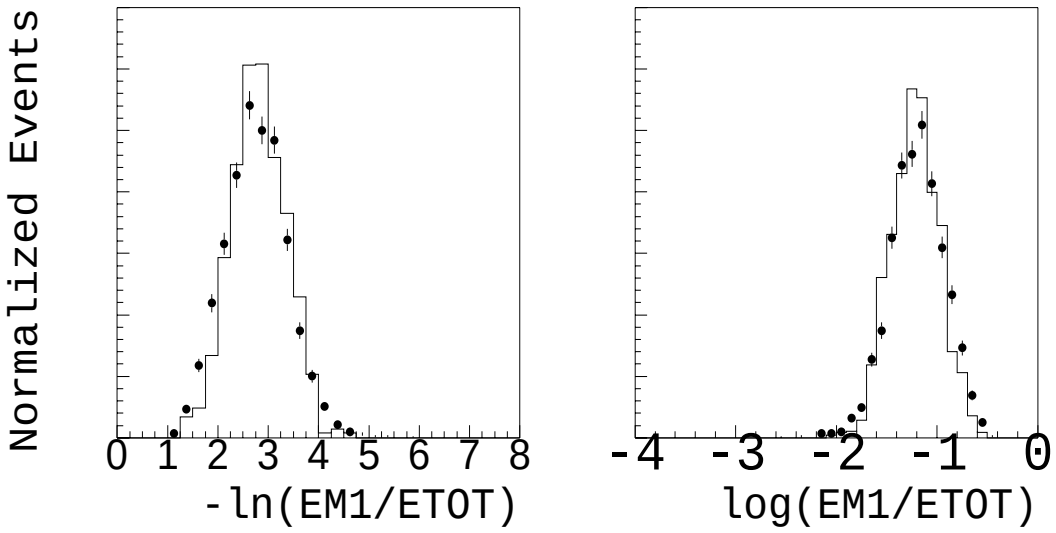

Figure 4.12: -ln(EM1/ETOT)(left) and Log(EM1/ETOT)(right) distributions for Z electrons from data (points) and Monte Carlo (histograms), CC only.

$$(-\ln(EM1/ETOT))_{\gamma 1} \times (-\ln(EM1/ETOT))_{\gamma 2}$$

as the event discriminant. The distributions of the discriminants are shown in Fig. 4.13. Random numbers are generated according to the histograms of photons and fakes. The random numbers are multiplied to make products of three combinations, phot*phot, phot*fake and fake*fake, whose distributions are shown in Fig. 4.13.

4.4.3 Fitting Double-photon purity $\alpha^{\gamma\gamma}$

The distribution of the double-photon event discriminant can be filled into a histogram of n bins, resulting in a set of numbers d_1, d_2...d_n. Let us fill the histograms of the discriminant of the modeled phot*phot, phot*fake and fake*fake in the same bins, and let $f_i(\alpha^{\gamma\gamma}, \alpha^{\gamma f}, \alpha^{ff})$ be the expected number of

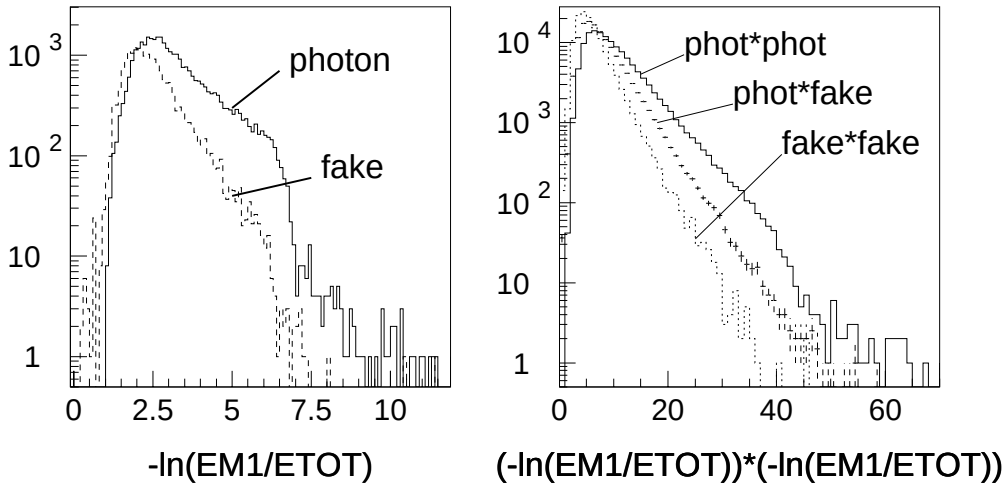

Figure 4.13: The distributions of -ln(EM1/ETOT) for modeled photons and fakes are shown left, and right are the product distributions for phot*phot, phot*fake and fake*fake.

events in the bin i, where $\alpha^{\gamma\gamma}$, $\alpha^{\gamma f}$ and α^{ff} are the fractions of the respective sources. $f_i(\alpha^{\gamma\gamma}, \alpha^{\gamma f}, \alpha^{ff})$ can be expressed as:

$$f_i(\alpha^{\gamma\gamma}, \alpha^{\gamma f}, \alpha^{ff}) = N_D(\alpha^{\gamma\gamma}\frac{a_i^{\gamma\gamma}}{N^{\gamma\gamma}} + \alpha^{\gamma f}\frac{a_i^{\gamma f}}{N^{\gamma f}} + \alpha^{ff}\frac{a_i^{ff}}{N^{ff}}) \tag{4.21}$$

where N_D, $N^{\gamma\gamma}$, $N^{\gamma f}$ and N^{ff} are the total number of events in the samples of data, phot*phot, phot*fake and fake*fake respectively, and $a_i^{\gamma\gamma}$, $a_i^{\gamma f}$ and a_i^{ff} are the number of events in the ith bin from the three modeled sources. The fractions of the three sources have to sum up to unity:

$$\alpha^{\gamma\gamma} + \alpha^{\gamma f} + \alpha^{ff} = 1 \tag{4.22}$$

Let d_i to be the measured number of events in the ith bin from the data sample, the probability distribution for d_i is a Poisson(where f_i is the expected number):

$$e^{-f_i}\frac{f_i^{d_i}}{d_i!} \tag{4.23}$$

The three sources, phot*phot, phot*fake and fake*fake, are modeled using Monte Carlo, and only have finite number of events. Let A_i be the expected number of events for the measured a_i; a_i follows a Binomial distribution. It can be approximated as a Poisson when A_i is much smaller than the total number of events in the sample:

$$e^{-A_i}\frac{A_i^{a_i}}{a_i!} \tag{4.24}$$

The overall log likelihood, including the Poisson distributions for data and the modeled three sources, can therefore be expressed as:

$$\ln\mathcal{L} = \sum_{i=1}^{n} d_i \ln f_i - f_i + \sum_{i=1}^{n}\sum_{j}^{\gamma\gamma,\gamma f,ff} a_i^j \ln A_i^j - A_i^j \tag{4.25}$$

By maximizing $\ln\mathcal{L}$ with respect to $\alpha^{\gamma\gamma}$, $\alpha^{\gamma f}$, α^{ff} and $A_i^{\gamma\gamma}$, $A_i^{\gamma f}$, A_i^{ff}, we can determine the fractions of the three sources. A detailed description of the approach, *Fitting using Finite Monte Carlo Samples*, can be found elsewhere [100, 101].

Due to their physics meaning, the three fraction parameters $\alpha^{\gamma\gamma}$, $\alpha^{\gamma f}$, α^{ff} can only have the value between 0 and 1, and their sum has to be equal to 1. To avoid any boundary anomaly, a transformation on the α parameters is performed, giving the new parameters θs as follows:

$$\alpha^{\gamma\gamma} = \sin^2(\theta^{\gamma\gamma}) \tag{4.26}$$

$$\alpha^{\gamma f} = \sin^2(\theta^{\gamma f}) \tag{4.27}$$

$$\alpha^{ff} = \sin^2(\theta^{ff}) \tag{4.28}$$

The θ parameters can take any value between -π and π to guarantee the α parameters falling in their physical range.

Subsample	$E_T^1 <$ **20.** $E_T^2 <$ **20.**	$E_T^1 >$ **20.** $E_T^2 <$ **20.**	$E_T^1 >$ **20.** $E_T^2 >$ **20.**
Num Evts	113	139	81
$< E_T^1 >$	17.26 GeV	25.50 GeV	34.04 GeV
$< E_T^2 >$	15.85 GeV	16.93 GeV	28.71 GeV
$\theta^{\gamma\gamma}$	$0.76^{+0.26}_{-0.20}$	$0.90^{+0.16}_{-0.28}$	$0.79^{+0.11}_{-0.14}$
$\theta^{\gamma f}$	$0.81^{+0.20}_{-0.49}$	$0.33^{+0.35}_{-0.87}$	$0.00^{+0.49}_{-0.49}$
θ^{ff}	$0.00^{+0.48}_{-0.48}$	$0.56^{+0.15}_{-0.36}$	$0.78^{+0.11}_{-0.14}$
$\alpha^{\gamma\gamma}$	$0.47^{+0.25}_{-0.20}$	$0.61^{+0.14}_{-0.28}$	$0.51^{+0.11}_{-0.14}$
$\alpha^{\gamma f}$	$0.53^{+0.20}_{-0.43}$	$0.10^{+0.28}_{-0.10}$	$0.00^{+0.22}_{at\ limit}$
α^{ff}	$0.00^{+0.21}_{at\ limit}$	$0.28^{+0.14}_{-0.24}$	$0.49^{+0.11}_{-0.14}$

Table 4.5: Summary of Double-photon Purity Fitting Results for three regions.

Assumption	$E_T^1 < \mathbf{20.}$ $E_T^2 < \mathbf{20.}$	$E_T^1 > \mathbf{20.}$ $E_T^2 < \mathbf{20.}$	$E_T^1 > \mathbf{20.}$ $E_T^2 > \mathbf{20.}$
$\alpha^{\gamma\gamma} + \alpha^{\gamma f} + \alpha^{ff} = 1$ $\alpha^{\gamma f} = 0$	$0.72^{+0.18}_{-0.19}$	$0.66^{+0.15}_{-0.16}$	$0.57^{+0.17}_{-0.17}$
$\alpha^{\gamma\gamma} + \alpha^{\gamma f} + \alpha^{ff} = 1$ $\alpha^{\gamma f} = \alpha^{ff}$	$0.63^{+0.19}_{-0.19}$	$0.55^{+0.17}_{-0.17}$	$0.46^{+0.22}_{-0.22}$
$\alpha^{\gamma\gamma} + \alpha^{\gamma f} + \alpha^{ff} = 1$ $\alpha^{ff} = 0$	$0.46^{+0.27}_{-0.25}$	$0.37^{+0.23}_{-0.23}$	$0.31^{+0.33}_{-0.28}$

Table 4.6: Fitted results for three assumed cases.

The double-photon data sample is divided into three subsamples. The log-likelihood fitting is performed for each subsample. The resulting fraction of the true photon*photon events in the data sample is called $\alpha^{\gamma\gamma}$, which will be denoted as the $\gamma\gamma$ purity sometime. The results of these fits are summarized in Table 4.5, where the errors are the statistical errors of the fit.

We notice the strong decrease of one background fraction, $\alpha^{\gamma f}$, with increasing P_T, accompanied by a strong increase of the other background, α^{ff}. This indicates an instability of the fit with two independent parameters. To estimate this effect, we performed some tests by reducing this two-parameter fit into a one-parameter fit. Three cases are considered, listed as follows:

1. assume one background source, phot*fake, is negligible.

   $\alpha^{\gamma\gamma} + \alpha^{\gamma f} + \alpha^{ff} = 1$ and $\alpha^{\gamma f} = 0$

2. assume two background sources, phot*fake and fake*fake, are equal.

Subsample	$E_T^1 < \mathbf{20.}$ $E_T^2 < \mathbf{20.}$	$E_T^1 > \mathbf{20.}$ $E_T^2 < \mathbf{20.}$	$E_T^1 > \mathbf{20.}$ $E_T^2 > \mathbf{20.}$
$\alpha^{\gamma\gamma}\|_{\rm test}$	0.53 ± 0.17	0.49 ± 0.15	0.46 ± 0.15

Table 4.7: Likelihood weighted $\alpha^{\gamma\gamma}|_{\rm test}$ values for three subsamples.

$$\alpha^{\gamma\gamma} + \alpha^{\gamma f} + \alpha^{ff} = 1 \quad \text{and} \quad \alpha^{\gamma f} = \alpha^{ff}$$

3. assume the other background source, fake*fake, is negligible.

$$\alpha^{\gamma\gamma} + \alpha^{\gamma f} + \alpha^{ff} = 1 \quad \text{and} \quad \alpha^{ff} = 0$$

The resulting fits are summarized in Table 4.6. The log likelihood as a function of any two of the three parameters $\alpha_{\gamma\gamma}$, $\alpha_{\gamma j}$ and α_{jj} above shows a strong correlation between the two parameters. Effectively varying the paramters within their full range but using the likelihood function $\mathcal{L}$ as a weight we calculate for each E_T range the average $\gamma\gamma$ purity and its variance, called $\alpha^{\gamma\gamma}|_{\rm test}$ and $\sigma^2(\alpha^{\gamma\gamma}|_{\rm test})$, as follows,

$$\alpha^{\gamma\gamma}|_{\rm test} = \int \alpha^{\gamma\gamma}\mathcal{L}d\alpha^{\gamma\gamma}d\alpha^{\gamma f} \tag{4.29}$$

Its associated uncertainty, called $\sigma^2(\alpha^{\gamma\gamma}|_{\rm test})$, is equal to

$$\sigma^2(\alpha^{\gamma\gamma}|_{\rm test}) = \int(\alpha^{\gamma\gamma} - \alpha^{\gamma\gamma}_{\rm test})^2\mathcal{L}d\alpha^{\gamma\gamma}d\alpha^{\gamma f} \tag{4.30}$$

The resulting values are listed in Table 4.7. Within the fitting statistical errors, we see no evidence for an E_T dependence of the $\gamma\gamma$ purity $\alpha_{\gamma\gamma}$. The fitted fraction $\alpha^{\gamma\gamma}$s in Table 4.5 are consistent with the test results in Table 4.7 within the fitting uncertainties.

Even though the MonteCarlo (EM1/ETOT) distribution has been compared with Z electrons, and has shown good agreement (see Fig. 4.12). The

Subsample	$E_T^1 < \mathbf{20.}$ $E_T^2 < \mathbf{20.}$	$E_T^1 > \mathbf{20.}$ $E_T^2 < \mathbf{20.}$	$E_T^1 > \mathbf{20.}$ $E_T^2 > \mathbf{20.}$
$\frac{\delta(\alpha^{\gamma\gamma})}{\alpha^{\gamma\gamma}}$	42%	52%	22%

Table 4.8: The total errors for $\alpha^{\gamma\gamma}$.

(EM1/ETOT) distribution for electrons from Z decay occupies the range from 0.01 to 0.1, (see Fig. 4.12), whereas the (EM1/ETOT) distribution for photons has a sizable fraction below 0.01 (see Fig. 4.11). In view of the good agreement of the data and Monte Carlo distributions in Fig. 4.12, we assume that the Monte Carlo distribution extrapolates the EM1/ETOT distribution well into the region below 0.01. Later on, we will refer the (EM1/ETOT) distribution as the discriminant distribution.

To estimate the uncertainties resulting from the shapes of the discriminants, each bin of the discriminant distribution is fluctuated by one standard deviation randomly up or down. They are then multiplied to form the products of three combinations, phot*phot, phot*fake and fake*fake, and the resulting histograms are smoothed. The log likelihood fitting is performed once more on data with the three new discriminant distributions. The biggest change in the fitted result $\alpha_{\gamma\gamma}$ is $\approx$ 25 %. The final errors are calculated by adding this 25% and the errors above in quadrature, as listed in Table 4.8. The phot*phot fraction $\alpha^{\gamma\gamma}$, sometimes called purity, will be used in the cross section determination in Chapter 6.

Chapter 5

Cross Sections and Error Analysis

The differential cross sections for direct double-photon production are determined as:

$$\frac{d\sigma}{dX} = \frac{\alpha_{\gamma\gamma}}{\Delta X\ L\ \mathcal{A}\ \epsilon_{\rm trig}\ \epsilon_{\rm offl}} N \tag{5.1}$$

where X refers to the kinematic quantities, the single photon transverse energy E_T^{γ}, the double-photon pair mass $M^{\gamma\gamma}$, the transverse momentum of the double-photon system $P_T^{\gamma\gamma}$ and the azimuthal opening angle of the pair $\Delta\phi^{\gamma\gamma}$. L refers to the integrated luminosity, $\mathcal{A}$ the geometric acceptance, $\epsilon_{\rm trig}$ the trigger efficiency, $\epsilon_{\rm offl}$ the offline efficiency and $\alpha_{\gamma\gamma}$ the fraction of the true photon*photon events. Let us assign a weight w_i to each event as:

$$w_i = \frac{\alpha_{\gamma\gamma}}{\Delta X\ L\ \mathcal{A}\ \epsilon_{\rm trig}\ \epsilon_{\rm offl}} \tag{5.2}$$

The cross section in each ΔX bin is equal to the sum of the w_i. We use the statistical fluctuation of the signal sample in each bin as its statistical error

$$(\delta^{\rm stat})^2 = \sum w_i^2 \tag{5.3}$$

The rest of the chapter will discuss the systematic errors for cross sections from each component in (5.1).

5.1 Systematic Errors

5.1.1 Luminosity and Acceptance

Section 2.1.3 describes how in DØ the *luminosity monitor constant* is determined and from it the integrated luminosity L. The associated error is

$$\frac{\delta L}{L} = 5.4\% \tag{5.4}$$

To determine the systematic error of the geometric acceptance $\mathcal{A}$, three sets of PDF: CTEQ2M, CTEQ3M and MRSA, are chosen to generate PYTHIA double-photon events. The differences are $\approx 3\%$. Taking into account the statistical uncertainties in determining the acceptance, 0.1 - 0.3 % (see Section 4.2.3), the overall systematic error on $\mathcal{A}$ is

$$\frac{\delta_{\mathcal{A}}}{\mathcal{A}} \approx 3\% \tag{5.5}$$

Both errors from the luminosity and the acceptance only affect the normalization of the cross sections, and don't change their shapes.

5.1.2 Trigger and Offline Efficiencies

The trigger turn_on curves are shown in Fig. 4.5. The curves are moved up and down coherently by one standard deviation, derived from the errors of

the fitted parameters. The resulting changes in the cross sections are: 2.3 - 9.0 %, varying from bins to bins.

In the same way, the offline efficiency curves (see Fig. 4.7) are moved up and down to study the resulting errors of the cross sections, which are 0.8 - 2.0 %.

5.1.3 EM Energy Scale

The EM energy scale uncertainties are reflected by the following equation:

$$E^{\gamma}_{meas} = \alpha \, E^{\gamma}_{true} + \delta \tag{5.6}$$

where the uncertainties are (see Section 3.5.2):

$$\alpha = 0.9514 \pm 0.0018^{+0.0061}_{-0.0017} \tag{5.7}$$

$$\delta = -0.158 \pm 0.015^{+0.03}_{-0.21} \; GeV \tag{5.8}$$

If the energy is measured wrongly by one standard deviation from both α and δ, the resulting changes in the cross sections are around 1 - 7 %.

Chapter 6

Summary and Conclusion

Taking the acceptance A, the efficiencies $\epsilon_{\rm trig}$, $\epsilon_{\rm offl}$, and the $\gamma\gamma$ purity $\alpha_{\gamma\gamma}$ in Chapter 4 and the error analysis in Chapter 5, we are ready to present the differential cross sections of direct double-photon production $d\sigma/dE_T^\gamma$, $d\sigma/dM^{\gamma\gamma}$, $d\sigma/dP_T^{\gamma\gamma}$ and $d\sigma/d\Delta\phi^{\gamma\gamma}$.

6.1 The Differential Cross Sections

Equation 5.1 describes how the differential cross sections are determined. Fig. 6.1 shows the double-photon cross section vs E_T^γ, and Figs. 6.2, 6.3 and 6.4 are the cross section vs $M^{\gamma\gamma}$, $P_T^{\gamma\gamma}$ and $\Delta\phi^{\gamma\gamma}$ respectively. The measured values are listed in Table 6.1, 6.2, 6.3 and 6.4. The error bars in the plots are statistical only. The systematic uncertainties include the contributions from the integrated luminosity L, the geometric acceptance $\mathcal{A}$, the trigger efficiencies $\epsilon_{\rm trig}(E_T^1, E_T^2)$ and the offline efficiencies $\epsilon_{\rm offl}(E_T^1, E_T^2)$ discussed in Section 5.1,

and the photon-photon purity $\alpha^{\gamma\gamma}$ in Section 4.4.3. The total systematic uncertainties are calculated by adding them in quadrature.

6.1.1 Theoretical Predictions and Comparisons

The measured cross sections are compared to three theoretical predictions, NLO QCD calculation [35], Resummed QCD calculation [28, 29] and PYTHIA [95], as shown in Figs. 6.1, 6.2, 6.3, 6.4. PYTHIA is a Monte Carlo program, including the Born, the Bremsstrahlung and the Box diagrams(see 1.5), and the parton shower modeling. The resummed QCD calculation(RESBOS) so far does not extend to high transverse momenta($P_T^{\gamma\gamma}$) of photon pair. In Fig. 6.1 and 6.2, data agree reasonably well with the NLO QCD calculation and PYTHIA Monte Carlo. Both models, however, are above the data points at the high E_T^{γ} and $M^{\gamma\gamma}$ tails. At the low $M^{\gamma\gamma}$ end, PYTHIA underpredicts the cross section than the NLO QCD calculation.

One may expect the resummed QCD calculation to describe the data better at small $P_T^{\gamma\gamma}$ and large $\Delta\phi^{\gamma\gamma}$, whearas the NLO QCD prediction is better at large $P_T^{\gamma\gamma}$ and small $\Delta\phi^{\gamma\gamma}$, as shown in Fig. 6.3 and 6.4. Note that PYTHIA Monte Carlo(including parton shower modeling) fits the small $P_T^{\gamma\gamma}$ and large $\Delta\phi^{\gamma\gamma}$ as well, not unexpected. Except the overall normalization in PYTHIA is a little low.

E_T^γ Bin (GeV)	$< E_T^\gamma >$ (GeV)	Events per GeV (Num/GeV)	$d\sigma/dE_T^\gamma$ (pb/GeV) ($\pm$ stat $\pm$ syst)
16 - 18	16.90	54.0 $\pm$ 5.2	1.377 $\pm$ 0.133 $\pm$ 0.524
18 - 20	19.00	48.0 $\pm$ 4.9	1.184 $\pm$ 0.122 $\pm$ 0.452
20 - 22	20.94	37.0 $\pm$ 4.3	1.013 $\pm$ 0.119 $\pm$ 0.641
22 - 24	22.89	26.0 $\pm$ 3.6	0.684 $\pm$ 0.096 $\pm$ 0.256
24 - 28	25.87	16.5 $\pm$ 2.0	0.422 $\pm$ 0.053 $\pm$ 0.145
28 - 32	29.69	10.5 $\pm$ 6.5	0.257 $\pm$ 0.040 $\pm$ 0.080
32 - 40	35.30	3.87 $\pm$ 0.69	0.0922 $\pm$ 0.0167 $\pm$ 0.0279
40 - 56	47.11	1.75 $\pm$ 0.33	0.0402 $\pm$ 0.0077 $\pm$ 0.0118
56 - 80	66.69	0.292 $\pm$ 0.110	0.0068 $\pm$ 0.0026 $\pm$ 0.0020

Table 6.1: The differential cross section values $d\sigma/dE_T^\gamma$ vs E_T^γ.

6.1.2 Integrated Cross Section

With the differential cross sections determined, we can calculate the integrated total cross section within the kinematic cuts. The total cross section is equal to

$$\sigma_{p\bar{p}\to\gamma\gamma+X} = 8.7 \pm 1.5(stat)^{+2.9}_{-3.4}(syst) \tag{6.1}$$

while the predicted total cross section by PYTHIA is equal to

$$\sigma_{p\bar{p}\to\gamma\gamma+X}|^{PYTHIA} = 7.1 \pm 0.2(stat) \tag{6.2}$$

6.2 Conclusions

The measurement of direct double-photon production provides a precise test of QCD. The data sample, corresponding to $\int \mathcal{L}dt = 82.36pb^{-1}$, shows

$M^{\gamma\gamma}$ Bin (GeV/c^2)	$< M^{\gamma\gamma} >$ (GeV/c^2)	Events per GeV/c^2 (Num/GeV/c^2)	$d\sigma/dM^{\gamma\gamma}$ (pb/GeV/c^2) ($\pm$ stat $\pm$ syst)
10 - 20	13.95	0.60 $\pm$ 0.24	0.0178 $\pm$ 0.0073 $\pm$ 0.0091
20 - 28	24.26	2.12 $\pm$ 0.52	0.0609 $\pm$ 0.0148 $\pm$ 0.0238
28 - 32	30.33	8.75 $\pm$ 1.48	0.242 $\pm$ 0.0411 $\pm$ 0.104
32 - 36	34.17	13.50 $\pm$ 1.84	0.358 $\pm$ 0.0492 $\pm$ 0.134
36 - 40	37.95	15.75 $\pm$ 7.94	0.425 $\pm$ 0.0543 $\pm$ 0.176
40 - 44	41.79	12.50 $\pm$ 1.77	0.340 $\pm$ 0.0486 $\pm$ 0.155
44 - 48	45.85	7.25 $\pm$ 1.35	0.188 $\pm$ 0.0352 $\pm$ 0.076
48 - 56	51.70	3.75 $\pm$ 0.68	0.0903 $\pm$ 0.0166 $\pm$ 0.0285
56 - 64	58.85	2.75 $\pm$ 0.59	0.0608 $\pm$ 0.0130 $\pm$ 0.019
64 - 80	69.87	0.75 $\pm$ 0.22	0.0170 $\pm$ 0.0049 $\pm$ 0.0050
80 - 132	93.99	0.269 $\pm$ 0.072	0.0058 $\pm$ 0.0016 $\pm$ 0.0019

Table 6.2: The differential cross section values $d\sigma/dM^{\gamma\gamma}$ vs $M^{\gamma\gamma}$.

reasonable agreement between the data and the NLO QCD in the high Q^2 region and a reasonable agreement between the data and a Resummed QCD calculation(RESBOS) and PYTHIA in the low Q^2 region. The direct double-photon process is also the dominant background for the SM higgs search in the intermediate mass range $80 \leq M_H \leq 150$ at the LHC. This measurement at the Tevatron can help us to have better understanding of QCD, and improve the prediction of the background for the SM Higgs search at LHC.

$P_T^{\gamma\gamma}$ Bin (GeV/c)	$< P_T^{\gamma\gamma} >$ (GeV/c)	Events per GeV/c (Num/GeV/c)	$d\sigma/dP_T^{\gamma\gamma}$ (pb/GeV/c) ($\pm$ stat $\pm$ syst)
0 - 2	1.242	12.5 $\pm$ 2.5	0.303 $\pm$ 0.0609 $\pm$ 0.113
2 - 4	3.028	31.5 $\pm$ 4.0	0.796 $\pm$ 0.1009 $\pm$ 0.262
4 - 6	4.954	20.0 $\pm$ 3.2	0.504 $\pm$ 0.0802 $\pm$ 0.148
6 - 8	6.883	20.5 $\pm$ 3.2	0.552 $\pm$ 0.0870 $\pm$ 0.197
8 - 10	9.058	14.0 $\pm$ 2.64	0.391 $\pm$ 0.0750 $\pm$ 0.153
10 - 12	11.081	12.0 $\pm$ 2.45	0.325 $\pm$ 0.0672 $\pm$ 0.116
12 - 14	13.094	12.0 $\pm$ 2.45	0.344 $\pm$ 0.0711 $\pm$ 0.143
14 - 16	14.741	6.0 $\pm$ 1.73	0.166 $\pm$ 0.0482 $\pm$ 0.0605
16 - 20	17.693	3.75 $\pm$ 0.97	0.1087 $\pm$ 0.0284 $\pm$ 0.0474
20 - 24	21.714	3.0 $\pm$ 0.87	0.0818 $\pm$ 0.0240 $\pm$ 0.0249
24 - 32	27.213	2.75 $\pm$ 0.59	0.0749 $\pm$ 0.0162 $\pm$ 0.0265
32 - 40	35.689	2.00 $\pm$ 0.50	0.0602 $\pm$ 0.0152 $\pm$ 0.0320
40 - 56	44.575	0.437 $\pm$ 0.165	0.0116 $\pm$ 0.0044 $\pm$ 0.0046
56 - 80	71.096	0.167 $\pm$ 0.083	0.0042 $\pm$ 0.0021 $\pm$ 0.00149

Table 6.3: The differential cross section values $d\sigma/dP_T^{\gamma\gamma}$ vs $P_T^{\gamma\gamma}$.

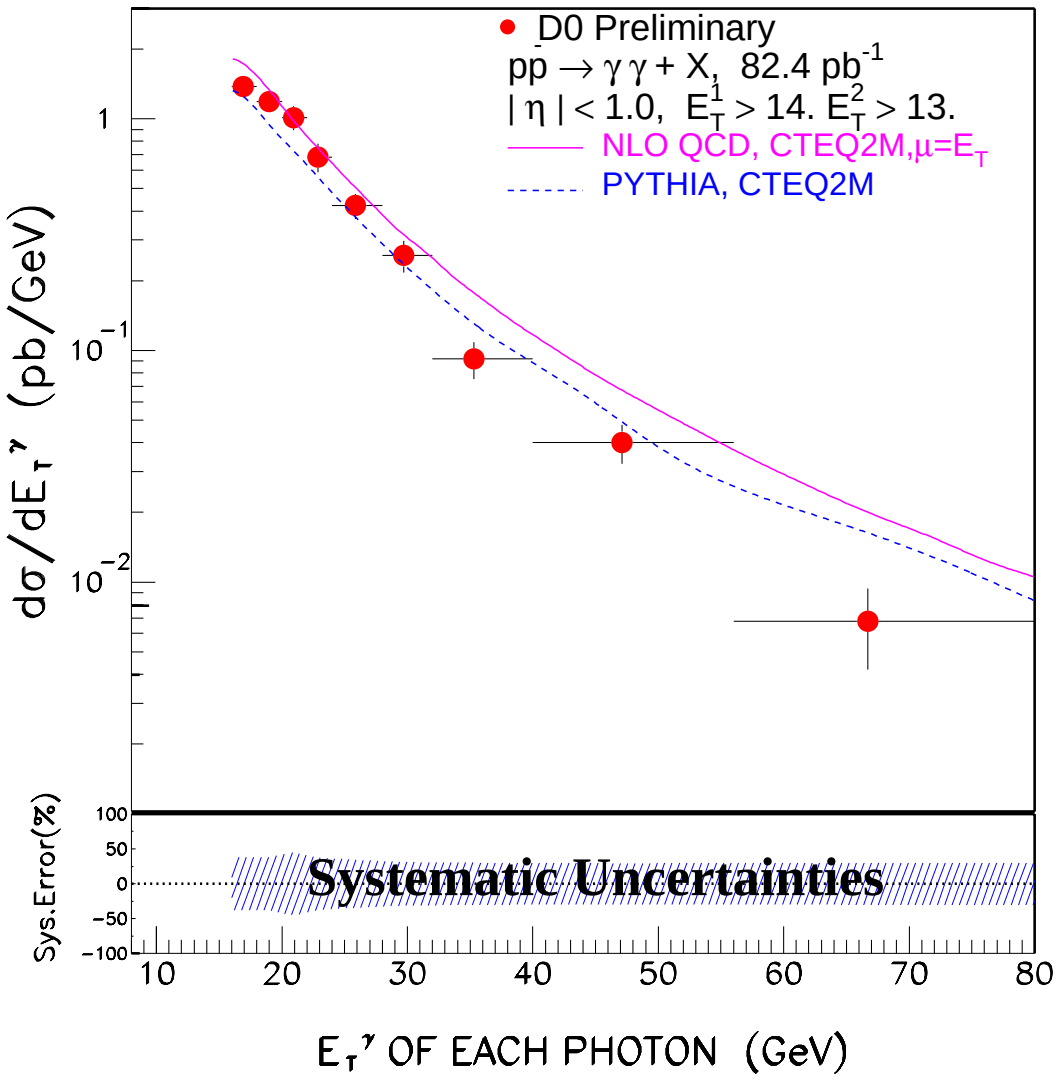

Figure 6.1: The differential cross section $d\sigma/dE_T^\gamma$.

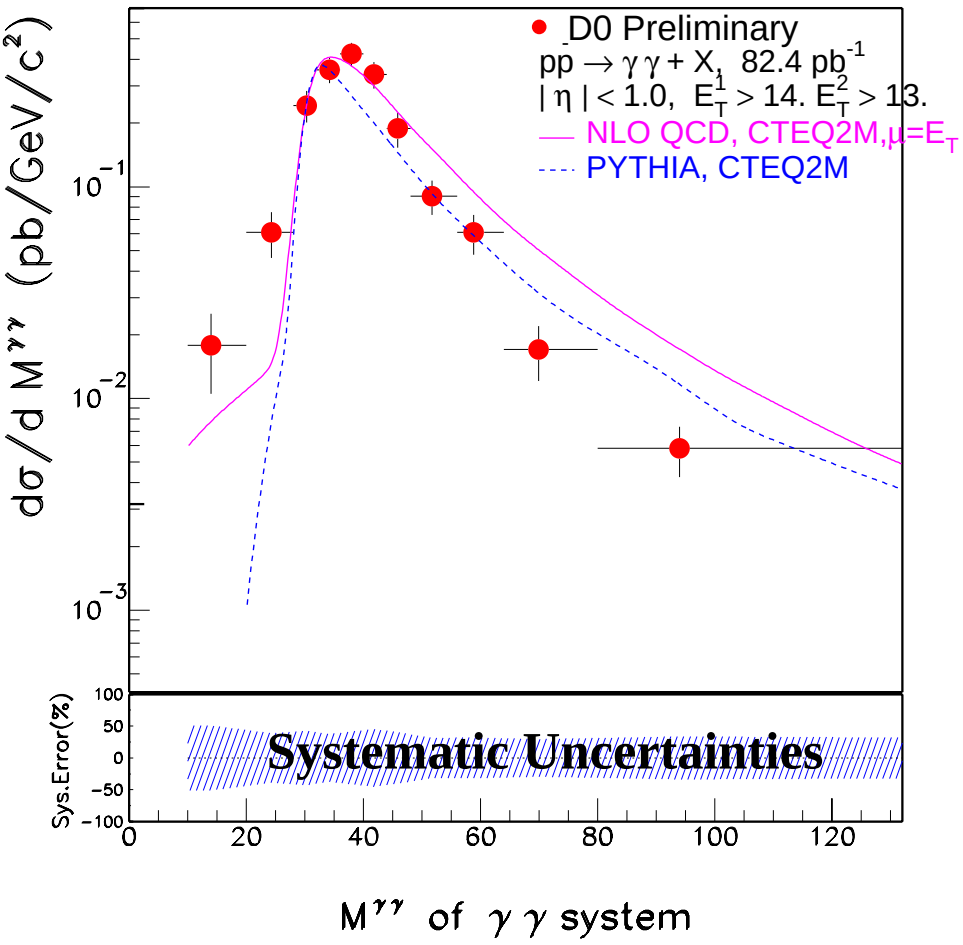

Figure 6.2: The differential cross section $d\sigma/dM^{\gamma\gamma}$.

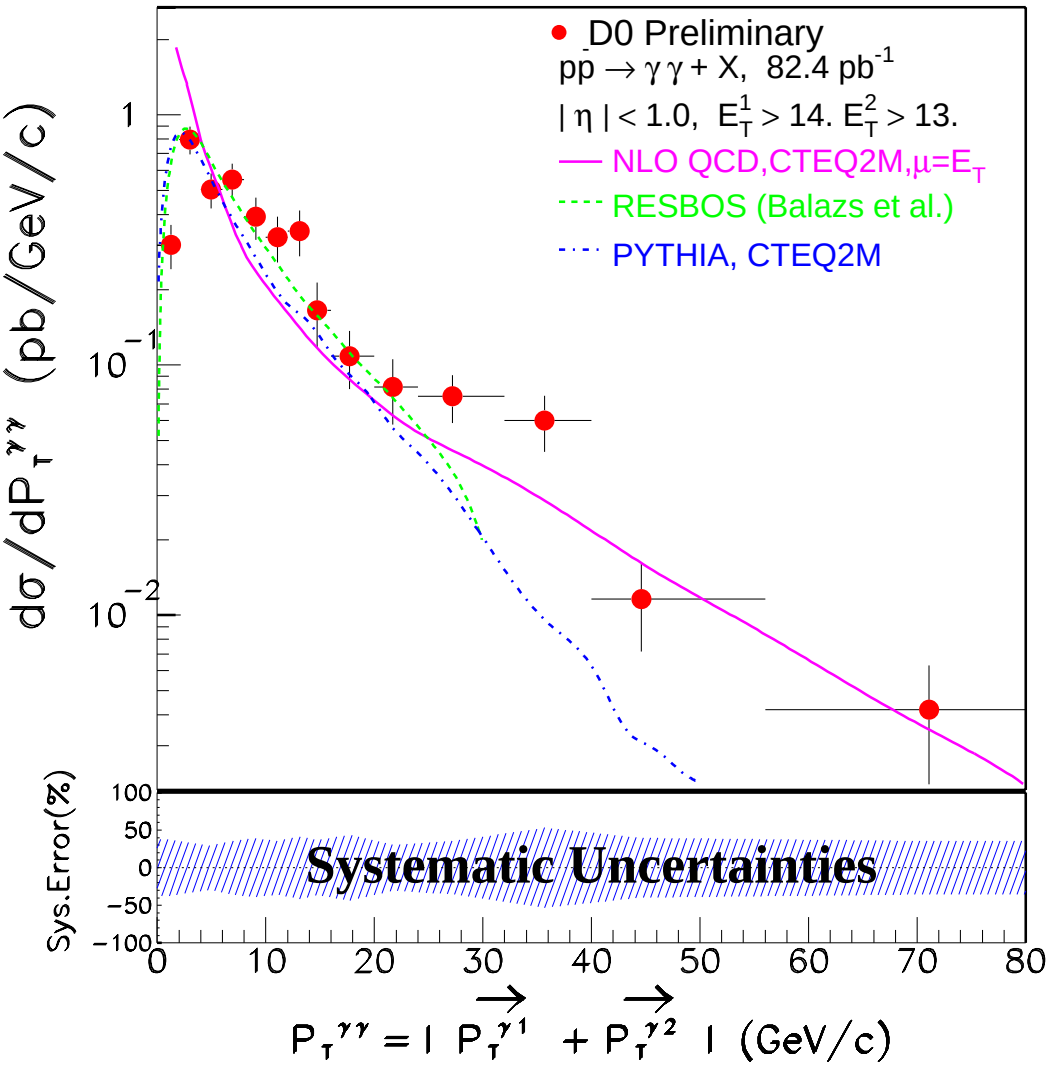

Figure 6.3: The differential cross section $d\sigma/dP_T^{\gamma\gamma}$.

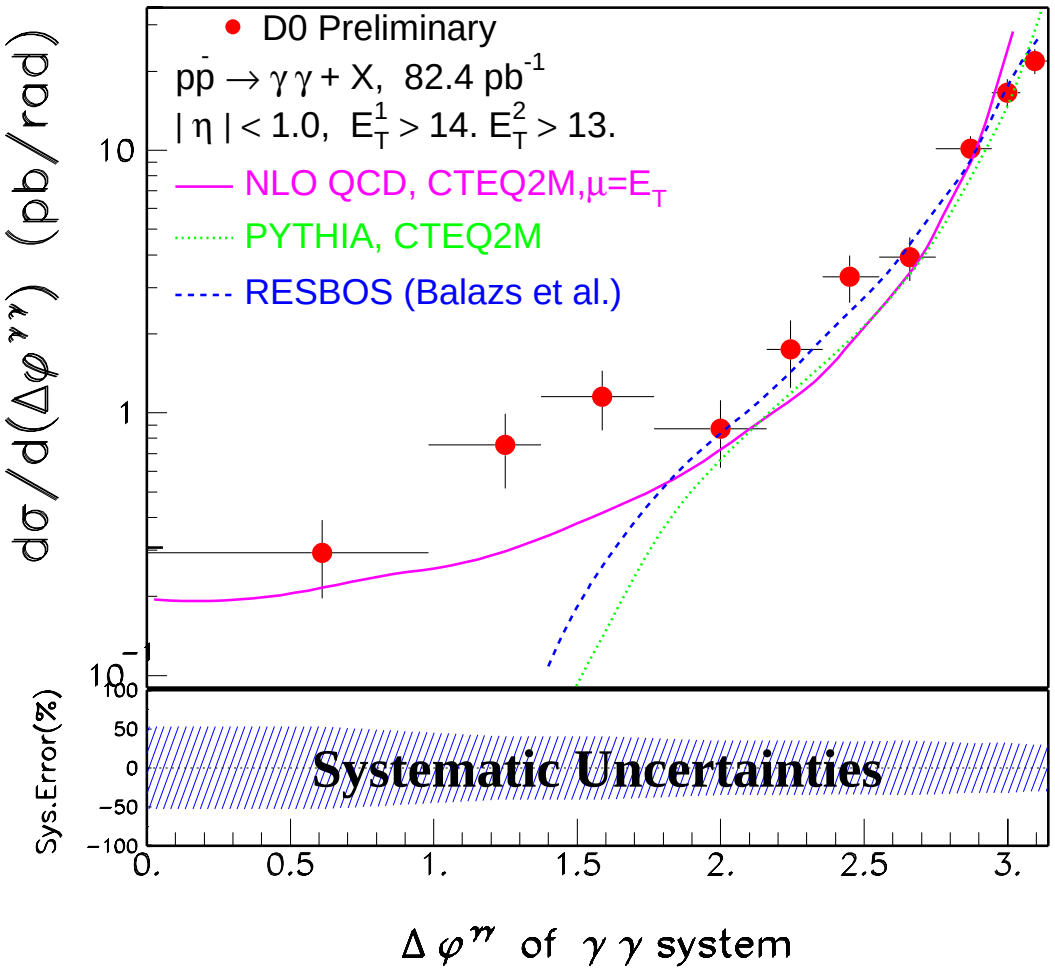

Figure 6.4: The differential cross section $d\sigma/d\Delta\phi^{\gamma\gamma}$.

$\Delta\phi^{\gamma\gamma}$ Bin (radian)	$< \Delta\phi^{\gamma\gamma} >$ (radian)	Events per radian (Num/radian)	$d\sigma/d\Delta\phi^{\gamma\gamma}$ (pb/radian) ($\pm$ stat $\pm$ syst)
0.0000 - 0.9817	0.6102	9.1677 $\pm$ 3.056	0.2726 $\pm$ 0.0913 $\pm$ 0.1444
0.9817 - 1.3744	1.2484	25.4654 $\pm$ 8.053	0.7104 $\pm$ 0.2267 $\pm$ 0.2877
1.3744 - 1.7672	1.5868	38.1981 $\pm$ 9.8627	1.0927 $\pm$ 0.2846 $\pm$ 0.4440
1.7672 - 2.1598	1.9987	30.5584 $\pm$ 8.821	0.8200 $\pm$ 0.2395 $\pm$ 0.2872
2.1598 - 2.3562	2.2441	61.1169 $\pm$ 17.643	1.6676 $\pm$ 0.4864 $\pm$ 0.5848
2.3562 - 2.5525	2.4501	122.234 $\pm$ 24.951	3.1846 $\pm$ 0.6573 $\pm$ 1.0793
2.5525 - 2.7489	2.6593	142.606 $\pm$ 26.950	3.7890 $\pm$ 0.7259 $\pm$ 1.3347
2.7489 - 2.9452	2.8701	381.981 $\pm$ 44.107	9.9268 $\pm$ 1.1594 $\pm$ 3.1806
2.9452 - 3.0434	2.9998	641.727 $\pm$ 80.850	16.347 $\pm$ 2.0812 $\pm$ 5.2904
3.0434 - 3.14159	3.0955	865.823 $\pm$ 93.912	21.717 $\pm$ 2.3796 $\pm$ 6.4979

Table 6.4: The differential cross section values $d\sigma/d\Delta\phi^{\gamma\gamma}$ vs $\Delta\phi^{\gamma\gamma}$.

Bibliography

[1] Particle Data Group, *Phys. Rev.*, **D54**, 1, 1996.

[2] Vernon Barger and Roger Phillips, *Collider Physics*, Addison-Wesley, 1988.

[3] George Sterman *et al.*, *Rev. Mod. Phys.*, **67**, 157, 1995.

[4] D. J. Gross and F. Wilczek, *Phys. Rev. Lett.*, **30**, 1343, 1973.

[5] H. D. Politzer, *Phys. Rev. Lett.*, **30**, 1346, 1973.

[6] C. Rubbia, *Rev. Mod. Phys.*, **57**, 699, 1985.

[7] F. Abe *et al.*, *Phys. Rev. Lett.*, **74**, 2626, 1995.

[8] S. Abachi *et al.* (The DØ collaboration), *Phys. Rev. Lett.*, **74**, 2632, 1995.

[9] E. D. Bloom *et al.*, *Phys. Rev. Lett.*, **23**, 930, 1969.

[10] J. I. Friedman and H. W. Kendall, *Ann. Rev. Nucl. Sci.*, **22**, 203, 1972.

[11] J. D. Bjorken, *Phys. Rep.*, **179**, 1547, 1969.

[12] R. P. Feynman, *Phys. Rev. Lett.*, **23**, 1415, 1969.

[13] CTEQ PDF web page, summary of PDFs.
(URL: `http://www.phys.psu.edu/ cteq/")`

[14] R. P. Feynman, *Photon-Hadron Interactions*, Benjamin, 1972.

[15] M. Gell-Mann, *Phys. Lett.*, **8**, 214, 1964.

[16] G. Zweig, *CERN preprint TH*, **401**, 412, 1964.

[17] D. J. Gross and F. Wilczek, *Phys. Rev.*, **D8**, 3633, 1973.

[18] S. Weinberg, *Phys. Rev. Lett.*, **31**, 494, 1973.

[19] S. L. Wu, *Phys. Rev.*, **C107**, 59, 1984.

[20] G. Sterman and S. Weinberg, *Phys. Rev. Lett.*, **39**, 1436, 1977.

[21] J. C. Collins and D. E. Soper, *Nucl. Phys.*, **B193**, 381, 1981.

[22] D. E. Soper J. C. Collins and G. Sterman, *Nucl. Phys.*, **B250**, 199, 1985.

[23] S. Catani and L. Trentadue, *Nucl. Phys.*, **B353**, 183, 1991.

[24] B. R. Webber S. Catani, G. Turnock and L. Trentadue, *Nucl. Phys.*, **B407**, 3, 1993.

[25] G. Altarelli and G. Parisi, *Nucl. Phys.*, **B126**, 298, 1977.

[26] G. Ladinsky and C. P. Yuan, *Phys. Rev.*, **D50**, 4239, 1994.

[27] Davies and Stirling, *Nucl. Phys.*, **B244**, 337, 1984.

[28] Csaba Balazs and C. P. Yuan, Resbos, the Monte Carlo program for resummed boson production and decay.
(URL: `http://pilot.msu.edu/user/balazscs/resbos.html`)

[29] Csaba Balazs and C. P. Yuan, Soft gluon effects on lepton pairs at hadron colliders, HEP preprint, hep-ph/9704258.
(URL: `http://xxx.lanl.gov/abs/hep-ph/9704258`)

[30] J. F. Owens, *Rev. Mod. Phys.*, **59**, 465, 1987.

[31] T. Ferbel and W. R. Molzon, *Rev. Mod. Phys.*, **56**, 181, 1984.

[32] J. D. Bjorken S. M. Berman and J. B. Kogut, *Phys. Rev.*, **D4**, 3388, 1971.

[33] P. Kessler C. Carimalo, M. Crozon and J. Parisi, *Phys. Rev.*, **D30**, 576, 1984.

[34] P. Aurenche *et al.*, *Z. Physik*, **C29**, 459, 1985.

[35] J. F. Owens B. Bailey and J. Ohnemus, *Phys. Rev.*, **D46**, 2018, 1992.

[36] R. Fergani P. Chiappetta and J. Guillet, *Phys. Lett.*, **B348**, 646, 1995.

[37] C. Kourkoumelis *et al.* (The R806 collaboration), *Z. Physik*, **C16**, 101, 1982.

[38] T. Akesson *et al.* (The AFS collaboration), *Z. Physik*, **C32**, 491, 1986.

[39] J. Badier *et al.* (The NA3 collaboration), *Phys. Lett.*, **B164**, 184, 1985.

[40] E. Bonvin *et al.* (The WA70 collaboration), *Z. Physik*, **C41**, 591, 1989.

[41] C. Albajar *et al.* (The UA1 collaboration), *Phys. Lett.*, **B209**, 385, 1988.

[42] J. Alitti *et al.* (The UA2 collaboration), *Phys. Lett.*, **B288**, 386, 1992.

[43] F. Abe *et al.* (The CDF collaboration), *Phys. Rev. Lett.*, **70**, 2232, 1993.

[44] S. Abachi *et al.* (The DØ collaboration), *Nucl. Inst. Meth.*, **A338**, 185, 1994.

[45] Donald H. Perkins, *Introduction to High Energy Physics*, Addison-Wesley, 1987.

[46] M. S. Livingstone and J. P. Blewett, *Particle accelerators*, McGraw-Hill, New York, 1962.

[47] M. H. Blewett, *Ann. Rev. Nucl. Sci.*, **17**, 427, 1967.

[48] William Joseph Thompson, Introduction to colliding beams at Fermilab, DØ Note 2367, 1994, Fermilab-TM 1909.

[49] Leon M. Lederman, *Scientific American*, page 48, March 1991.

[50] Helen T. Edwards, *Ann. Rev. Nucl. Part. Sci.*, **35**, 605, 1985.

[51] L. Thorndahl D. Möhl, G. Petrucci and S. van der Meer, *Phys. Rev.*, **C58**, 73, 1980.

[52] M. P. Church and J. P. Marriner, *Ann. Rev. Nucl. Part. Sci.*, **43**, 253, 1993.

[53] R. Partridge N. Amos, J. Linnemann and L. Paterno, Luminosity calculations for DØ, DØ Note 2031, 1994.

[54] N. Amos *et al.*, Change to the DØ luminosity monitor constant, DØ Note 2401, 1994, Fermilab-TM 1911.

[55] J. Bantly *et al.*, Improvement to the DØ luminosity monitor constant, DØ Note 2544, 1995, Fermilab-TM 1930.

[56] Peter Matthew Grudberg, *Measurement of the W and Z Boson Production Cross Sections in $p\overline{p}$ Collisions at $\sqrt{s}$ = 1.8 TeV*, PhD thesis, U.C. Berkeley, Berkeley, CA, 1997.

[57] F. Sauli, Principles of operation of multiwire proportional and drift chambers, in Thomas Ferbel, editor, *Experimental Techniques in High Energy Physics*. Addison-Wesley Publishing Company, 1987.

[58] A. Clark *et al.*, *Nucl. Inst. Meth.*, **A261**, 420, 1987.

[59] A. Clark *et al.*, *Nucl. Inst. Meth.*, **A279**, 243, 1989.

[60] Ties Behnke, *The Central Drift Chamber for the DØ Experiment: Design, Construction and Test*, PhD thesis, State University of New York at Stony Brook, Stony Brook, NY, 1989.

[61] R. Avery *et al.*, *IEEE Trans. Nucl. Sci. NS-*, **33**, 573, 1986.

[62] Jeffrey W. Bantly, *The Forward Drift Chamber Performance and Physics Capability in the 1990 FNAL Testbeam Run*, PhD thesis, Northwestern University, Evanston, IL, 1992.

[63] J. F. Detœuf *et al.*, *Nucl. Inst. Meth.*, **A265**, 157, 1988.

[64] J. F. Detœuf *et al.*, *Nucl. Inst. Meth.*, **A279**, 310, 1989.

[65] C. Fabjan, Calorimetry in high-energy physics, In Thomas Ferbel, editor, *Experimental Techniques in High Energy Physics*. Addison-Wesley Publishing Company, 1987.

[66] S. Abachi *et al.* (The DØ collaboration), *Phys. Rev. Lett.*, **77**, 3309, 1996.

[67] R. Hirosky, The response of the d-zero central calorimeter to electrons and pions from 2 through 150 GeV/c, DØ Note 1499, 1993.

[68] various central calorimeter survey values, available in the file `d0$stp$root:[geocal]srcp_raw_cc.dat`.

[69] S. Abachi *et al.* (The DØ collaboration), *Nucl. Inst. Meth.*, **A324**, 53, 1993.

[70] various end calorimeter survey values, available in the file `d0$stp$root:[geocal]srcp_raw_ec.dat`.

[71] H. Aihara *et al.*, *Nucl. Inst. Meth.*, **A325**, 393, 1993.

[72] Dean Schamberger, DØ calorimeter electronics, DØ Note 1026, 1991.

[73] Raymond E. Hall, *Search for the Top Quark in Dimuon Events at DØ*, PhD thesis, University of California at Riverside, Riverside, CA, 1994.

[74] M. Abolins *et al.*, *IEEE Trans. Nucl. Sci. NS-*, **36**, 384, 1989.

[75] M. Abolins *et al.*, *Nucl. Inst. Meth.*, **A289**, 543, 1990.

[76] Scott Stuart Snyder, *Measurement of the Top Quark Mass at D0*, PhD thesis, State University of New York at Stony Brook, Stony Brook, NY, 1995.

[77] Steven A. Jerger *Inclusive Direct Photon Production in the Central and Forward Rapidity Regions in Proton-Antiproton Collisions at a Center of Mass Energy of 1800 GeV*, PhD thesis, Michigan State University, Lansing, MI, 1997.

[78] CERN Program Library Q100 and Q101, *a long writeup of Zebra*, 1993.
(URL: `http://www.hep.net/cernlib/docs/www.dir/zebraold/ZEBRAMAIN.html`)
(URL: `http://wwwcn.cern.ch/asdoc/zebra/ZEBRAMAIN.html`)

[79] J. Bendich *et al.*, Beam xy position at dødetermined with vtx chamber, DØ Note 2331, 1994.

[80] C. Klopfenstein and M. Strovink, Comparison of hit finders on vertex chamber test data, DØ Note 445, 1986.

[81] Saul Youssef, *Comp. Phys. Comm.*, **45**, 423, 1987.

[82] T. C. Awes *et al.*, *Nucl. Inst. Meth.*, **A311**, 130, 1991.

[83] Steven Glenn and Azriel Goldschmidt, Corrections to biases in cluster-track matching, DØ Note 2419, 1995.

[84] Ulrich Heintz and Meenakshi Narain, A study of electron id efficiencies using z→ee decays, DØ Note 1814, 1993.

[85] Peter Grudberg, Cross section measurements of W and Z bosons to electrons at Dø: Event selection and efficiency studies, DØ Note 2316, 1994.

[86] R. Engelmann *et al.*, *Nucl. Inst. Meth.*, **A216**, 45, 1983.

[87] Meenakshi Narain, Electron identification in the dødetector, DØ Note 1548, 1992.

[88] S. Abachi *et al.* (The DØ collaboration), *Phys. Rev.*, **D52**, 4877, 1995.

[89] Lars Rasmussen Ulrich Heintz and Dean Schamberger, A study of the calibration pulser for the døcalorimeter, DØ Note 1430, 1992.

[90] Alexander Peryshkin and Rajendran Raja, On sampling fractions and electron shower shapes, DØ Note 1215, 1991.

[91] W. G. D. Dharmaratna, Reconstruction of the calorimeter response-test beam load 2, DØ Note 1731, 1993.

[92] Qiang Zhu, *Measurement of the W Boson Mass in Proton-Antiproton Collisions at* $\sqrt{s}$ *= 1.8 TeV*, PhD thesis, New York University, New York, NY 10003, 1994.

[93] N. Amos, Main ring veto counters for run 1b, DØ Note 2072, 1994.

[94] Torbjörn Sjöstrand, *Comp. Phys. Comm.*, **82**, 74, 1994.

[95] Torbjörn Sjöstrand, *a long writeup of PYTHIA 5.7 and JETSET 7.4*, 1993.
(URL: `http://wwwcn.cern.ch/asdoc/pythia_html3/pythia57.html`)

[96] CERN Program Library Long Writeup W5013, *GEANT – Detector Description and Simulation Tool*, 1993.
(URL: `http://wwwinfo.cern.ch/asdoc/geant_html3/geantall.html`)

[97] B. Abbott *et al.*(DØ), Determination of the mass of the w boson using the DØ detector at the tevatron, (*Phys. Rev. D* paper in preparation.).

[98] S. Abachi *et al.* (The DØ collaboration), *Phys. Rev. Lett.*, **75**, 1456, 1995.

[99] Steve Linn, private communication,

[100] Roger Barlow and Christine Beeston, *Comp. Phys. Comm.*, **77**, 219, 1993.

[101] CERN Program Library Long Writeup Y250, *HBOOK, version 4.22*, 1995.
(URL: `http://wwwinfo.cern.ch/asdoc/hbook_html3/hboomain.html`)